

AD-A158 105

NON-LINEAR CORRECTIONS TO THE LINEAR THEORY FOR THE
PREDICTION OF THE CAV. (U) MASSACHUSETTS INST OF TECH
CAMBRIDGE DEPT OF OCEAN ENGINEERIN. S A KINNAS JUN 85

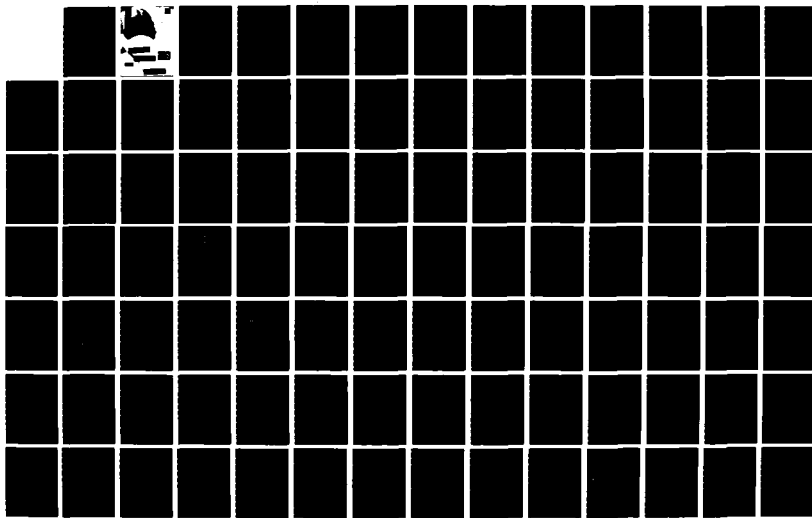
1/2

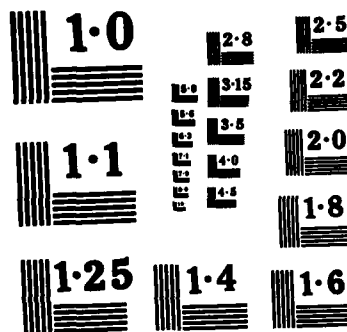
UNCLASSIFIED

DE-85-10 N00014-84-K-0067

F/G 2/4

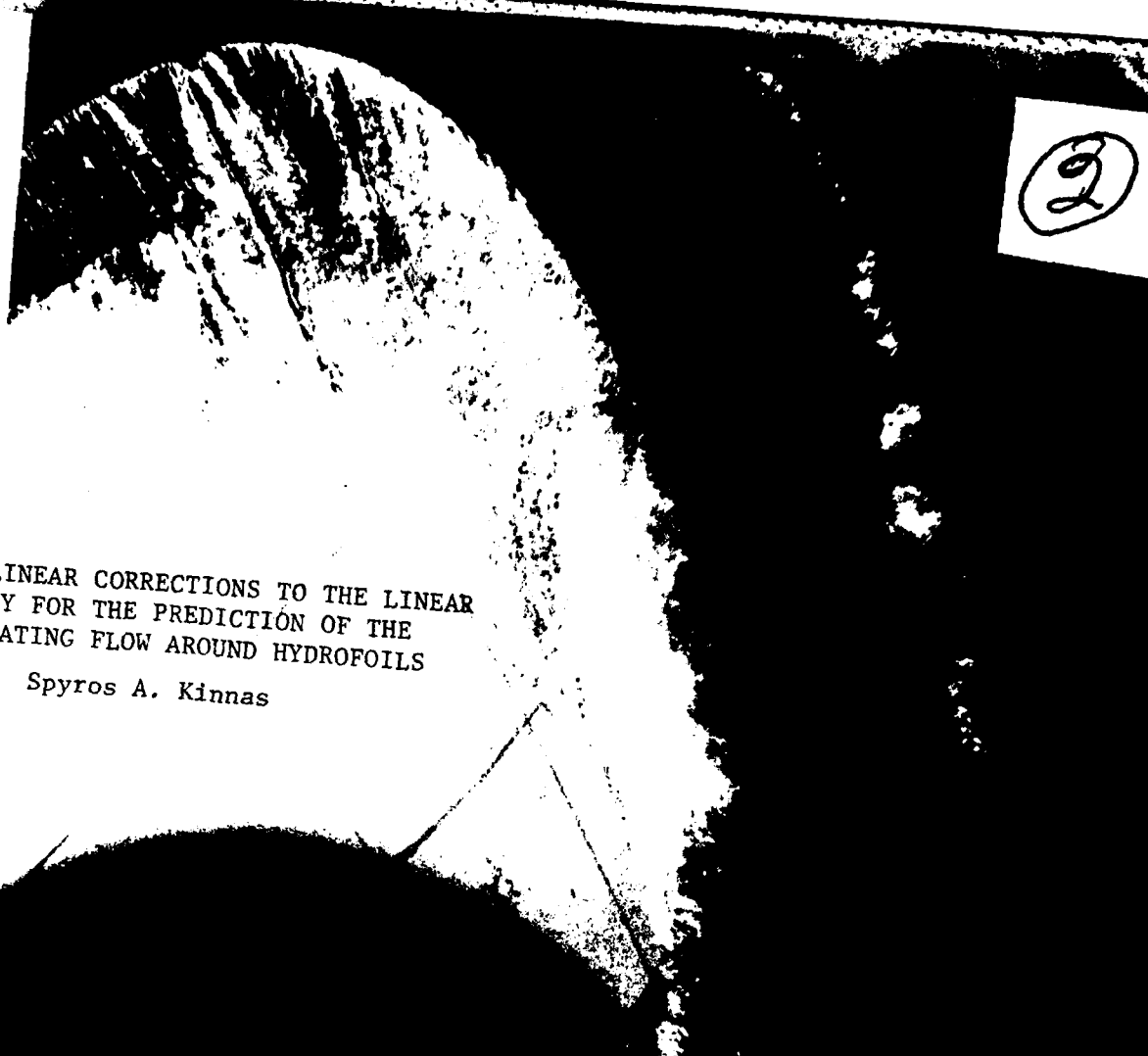
NL





NATIONAL BUREAU OF STANDARDS
MICROCOPY RESOLUTION TEST CHART

AD-A158 105

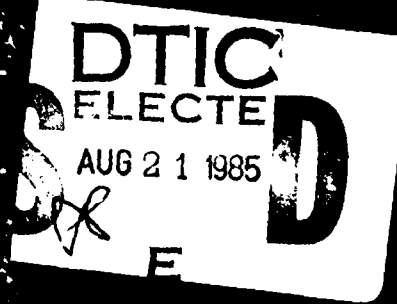


NON-LINEAR CORRECTIONS TO THE LINEAR
THEORY FOR THE PREDICTION OF THE
CAVITATING FLOW AROUND HYDROFOILS

Spyros A. Kinnas

DTIC FILE COPY

This document has been approved
for public release and sale; its
distribution is unlimited.



Massachusetts Institute of Technology

2

REPORT DOCUMENTATION PAGE**READ INSTRUCTIONS
BEFORE COMPLETING FORM**

1. REPORT NUMBER 85-10	2. GOVT ACCESSION NO. AD-A158 105	3. RECIPIENT'S CATALOG NUMBER
4. TITLE (and Subtitle) NON-LINEAR CORRECTIONS TO THE LINEAR THEORY FOR THE PREDICTION OF THE CAVITATING FLOW AROUND HYDROFOILS		5. TYPE OF REPORT & PERIOD COVERED TECHNICAL REPORT
7. AUTHOR(s) SPYROS A. KINNAS		8. PERFORMING ORG. REPORT NUMBER FINAL
9. PERFORMING ORGANIZATION NAME AND ADDRESS DEPARTMENT OF OCEAN ENGINEERING MASSACHUSETTS INSTITUTE OF TECHNOLOGY 77 MASSACHUSETTS AVENUE, CAMBRIDGE, MA 02139		10. PROGRAM ELEMENT, PROJECT, TASK AREA & WORK UNIT NUMBERS
11. CONTROLLING OFFICE NAME AND ADDRESS DAVID W. TAYLOR NAVAL SHIP R&D CENTER BETHESDA, MD 20084		12. REPORT DATE June 1985
		13. NUMBER OF PAGES 144
14. MONITORING AGENCY NAME & ADDRESS(if different from Controlling Office)		15. SECURITY CLASS. (of this report) UNCLASSIFIED
		15a. DECLASSIFICATION/DOWNGRADING SCHEDULE
16. DISTRIBUTION STATEMENT (of this Report) APPROVED FOR PUBLIC RELEASE: DISTRIBUTION UNLIMITED		
17. DISTRIBUTION STATEMENT (of the abstract entered in Block 20, if different from Report)		
18. SUPPLEMENTARY NOTES <i>en 1/20/85</i>		
 19. KEY WORDS (Continue on reverse side if necessary and identify by block number) CAVITATION; CAVITATING HYDROFOILS; CAVITY SHAPE; HYDROFOILS. <i>4</i>		
20. ABSTRACT (Continue on reverse side if necessary and identify by block number) <p>The problem of a partial or supercavitating hydrofoil in linear theory is formulated in terms of integral equations of unknown vortex and cavity source distributions. The general problem is decomposed into one of camber, one of thickness, and one of angle of attack.</p> <p>The general solution is given in terms of integrals of known functions over the cavity length for partial or over the chord length for supercavitating hydrofoils. The numerical scheme to compute the integrals is shown to be very accurate and insensitive to the variables of the problem. <i>→(over)</i></p>		

(continued, Block Number 20)

Cavity shapes obtained from linear and non-linear theory are compared for certain special cases. Linear theory is shown to be accurate for supercavitating sharp-nosed hydrofoils at moderate angles of attack.

The effect of the leading edge radius on the partial cavitation of a hydrofoil is introduced by incorporating Lighthill's correction in the linearized formulation of the problem. The results for certain special cases show the significant role of the leading edge radius on the cavitation of hydrofoils, something also confirmed from experiments conducted at the MIT water tunnel. *Keywords:* →(top A)

**MASSACHUSETTS INSTITUTE OF TECHNOLOGY
DEPARTMENT OF OCEAN ENGINEERING
CAMBRIDGE, MASSACHUSETTS 02139**

Report 85-10

**NON-LINEAR CORRECTIONS TO THE LINEAR THEORY FOR THE
PREDICTION OF THE CAVITATING FLOW AROUND HYDROFOILS**

by

Spyros A. Kinnas

June 1985

The preparation of this documentation was carried out under the Naval Sea Systems Command General Hydromechanics Research Program administered by the David W. Taylor Naval Ship Research and Development Center.

Office of Naval Research Contract N00014-84-0067. MIT OSP 94407.

Copyright (C) Massachusetts Institute of Technology 1985

ABSTRACT

The problem of a partial or supercavitating hydrofoil in linear theory is formulated in terms of integral equations of unknown vortex and cavity source distributions. The general problem is decomposed into one of camber, one of thickness, and one of angle of attack.

The general solution is given in terms of integrals of known functions over the cavity length for partial or over the chord length for supercavitating hydrofoils. The numerical scheme to compute the integrals is shown to be very accurate and insensitive to the variables of the problem.

Cavity shapes obtained from linear and non-linear theory are compared for certain special cases. Linear theory is shown to be accurate for supercavitating sharp-nosed hydrofoils at moderate angles of attack.

The effect of the leading edge radius on the partial cavitation of a hydrofoil is introduced by incorporating Lighthill's correction in the linearized formulation of the problem. The results for certain special cases show the significant role of the leading edge radius on the cavitation of hydrofoils, something also confirmed from experiments conducted at the MIT water tunnel.

Accession For	
NTIS GRA&I	<input checked="" type="checkbox"/>
DTIC TAB	<input type="checkbox"/>
Unannounced	<input type="checkbox"/>
Justification	
By _____	
Distribution/ _____	
Availability Codes	
Avail and/or	
Dist	Special
A-1	



ACKNOWLEDGEMENTS

I would like to thank my advisor, Prof. Justin E. Kerwin, for his constant support during my graduate studies. His insight during our numerous discussions was invaluable. The other members of the thesis committee--Prof. T. Francis Ogilvie, Dr. Robert Van Houten, Prof. Sheila Widnall, and Prof. Dick Yue--also contributed their time and talent unselfishly.

Many thanks are extended to Messrs. Dean Lewis, John Norton, William Coney, Wei-Zen Shih, and Mo-Hwa Wang for their help during the experimental part of this thesis, and to Dr. James Uhlman for useful discussions during the course of my work.

The superb typing of the thesis manuscript was done by Mrs. Beverly Scheibert and Kathy Perez, whose enormous effort is greatly appreciated.

At this point I would like to express my gratitude and love to my parents and brother for their endless encouragement during my studies.

TABLE OF CONTENTS

	<u>Page</u>
Abstract	2
Acknowledgments	3
Table of Contents	4
List of Figures	6
List of Tables	9
Nomenclature	10
INTRODUCTION	15
PART A. PARTIALLY CAVITATING HYDROFOIL - LINEAR THEORY	
1. Hydrofoil in non-cavitating flow - Linear theory	19
2. Partially cavitating hydrofoil - Linear theory	21
3. Decomposition in the partially cavitating hydrofoil problem	28
4. Solution to the partially cavitating hydrofoil problem	31
5. Cavitation number σ	32
6. Cavity volume V	34
7. Analytical solutions for some hydrofoils	36
8. Numerical method	43
9. The biconvex and the planoconvex hydrofoils	45
10. Comparison of the linear to the nonlinear theory	46
PART B. SUPERCAVITATING HYDROFOIL - LINEAR THEORY	
11. Formulation of the supercavitating hydrofoil problem	60
12. Decomposition in the supercavitating hydrofoil problem	63
13. Solution to the general supercavitating hydrofoil problem	65

	<u>Page</u>
14. Cavitation number σ	68
15. Cavity volume V	69
16. Cavity source distribution $q(z)$	69
17. Shape of the cavity	70
18. Analytical solutions for some supercavitating hydrofoils	71
19. Numerical method and results	73
PART C. CORRECTIONS TO THE LINEAR CAVITATING HYDROFOIL THEORY	
20. Lighthill's correction for non-cavitating hydrofoils	83
21. Lighthill's correction for cavitating hydrofoils	85
22. Effect of location of cavity detachment point on cavity shape	89
23. Open cavity model	102
PART D. CAVITATION EXPERIMENTS ON ROUND-NOSED HYDROFOILS	
24. Purpose and description of the experiment	105
25. Comparison of the measurements to theory	108
CONCLUSIONS	113
RECOMMENDATIONS	115
REFERENCES	116
APPENDICES	
A. List of integrals	121
B. Determination of the point where the cavity starts	125
C. Formulas used in Section 22	127
D. Characteristic curves and cavity plots for NACA 16 forms	130

LIST OF FIGURES

<u>Figure</u>	<u>Page</u>
1. Hydrofoil in non-cavitating flow - Linear theory	20
2. Partially cavitating hydrofoil - Linear theory	23
3. Decomposition of the partially cavitating hydrofoil problem into the camber, thickness, and flat plate problems	30
4. Special cases of partially cavitating hydrofoils	37
5. Degenerate cases of partially cavitating hydrofoils	41
6. Graph of function $f(n; s)$ for different values of λ .	42
7. a/σ vs. λ for biconvex hydrofoils, planoconvex hydrofoils, and a flat plate, all at $\alpha = 4^\circ$ - Linear theory	52
8. V vs. λ for biconvex hydrofoils, planoconvex hydrofoils, and a flat plate, all at $\alpha = 4^\circ$ - Linear theory	53
9. V vs. a/σ for biconvex hydrofoils, planoconvex hydrofoils, and a flat plate, all at $\alpha = 4^\circ$ - Linear theory	54
10. The elementary problems for partially cavitating 4% thick biconvex hydrofoil at $\lambda = 0.5$. (a) + (b) = (c)	55
11. The elementary problems for partially cavitating 4% thick planoconvex hydrofoil at $\lambda = 0.5$ (a) + (b) + (c) = (d)	56
12. Partially cavitating flat plate at $\alpha = 2^\circ$	57
13. Partially cavitating flat plate at $\alpha = 5^\circ$	58
14. Cavity plots for NACA 16-006 thickness form at $\alpha = 4^\circ$	59
15. Supercavitating hydrofoil in linear theory	61
16. Decomposition of the supercavitating hydrofoil problem	64
17. Change in the angle of attack (a) or in the scale (b)	66
18. Special cases: flat plate (a) and elliptic foil (b)	72
19. σ vs. λ for some supercavitating hydrofoils	79
20. V vs. λ for some supercavitating hydrofoils	80

<u>Figure</u>	<u>Page</u>
21. The Three elementary problems for NACA $\alpha = 0.8$, combined with NACA 0010 at $\alpha = 7^\circ$ and $\iota = 1.4$	81
22. Cavity plots for flat plate at $\alpha = 4^\circ$, $\iota = 1.4$	82
23. Lighthill's correction for non-cavitating flow (a) and cavitating flow (b)	84
24. Graph of leading edge radius correction factor $a(\rho_L; \iota)$ for different values of ρ_L	88
25. Flat plate with leading edge radius ρ_L , at $\alpha = 4^\circ$	90
26. Pure linear theory. All hydrofoils at $\alpha = 4^\circ$ and $\sigma = 1.07$	91
27. Linear theory including leading edge corrections. All hydrofoils at $\alpha = 4^\circ$ and $\sigma = 1.07$	92
28. Cavity plots for NACA 16-015 at $\alpha = 4^\circ$ for fixed $\iota = 0.5$ and different values of ι_0 using pure linear theory	98
29. Cavity plots for NACA 16-006 at $\alpha = 4^\circ$ for fixed $\iota = 0.5$ and different values of ι_0 using pure linear theory	99
30. Cavity plots for NACA 16-006 at $\alpha = 4^\circ$ for fixed $\iota = 0.5$ and different values of ι_0 using linear theory including leading edge corrections	100
31a. Cavity plates for NACA 16-006 thickness forms at $\alpha = 4^\circ$, $\sigma = 0.877$	101
31b. Cavity plots for flat plate at $\alpha = 5^\circ$, $\sigma = 1.246$	101
32a. Open cavity model in linear theory	104
32b. Cavity plots for NACA 16-006 thickness form at $\alpha = 4^\circ$.	104
33. Hydrofoil mounted in the MIT water tunnel	107
34. ι vs. α/σ for the two tested hydrofoils at MIT water tunnel - $\alpha = 2.7^\circ$	112

<u>Figure</u>	<u>Page</u>
D1. δ vs. a/σ for NACA 16 series sections of 6%, 9%, and 12% thickness/chord ratios at $\alpha = 4^\circ$ —pure linear theory	132
D2. δ vs. a/σ for NACA 16 series sections of 6%, 9%, and 12% thickness/chord ratios at $\alpha = 4^\circ$ —linear theory including leading edge corrections	132
D3. δ vs. a/σ for NACA 16 series sections of 6%, 9%, and 12% thickness/chord ratios at $\alpha = 4^\circ$ —non-linear theory	134
D4. V/a vs. δ for NACA 16 series sections of 6%, 9%, and 12% thickness/chord ratios at $\alpha = 4^\circ$ —pure linear theory	135
D5. V/a vs. δ for NACA 16 series sections of 6%, 9%, and 12% thickness/chord ratios at $\alpha = 4^\circ$ —linear theory including leading edge corrections	136
D6. V/a vs. δ for NACA 16 series sections of 6%, 9%, and 12% thickness/chord ratios at $\alpha = 4^\circ$ —non-linear theory	137
D7. V vs. a/σ for NACA 16 series sections of 6%, 9%, and 12% thickness/chord ratios at $\alpha = 4^\circ$ —pure linear theory	138
D8. V vs. a/σ for NACA 16 series sections of 6%, 9%, and 12% thickness/chord ratios at $\alpha = 4^\circ$ —linear theory including leading edge corrections	139
D9. V vs. a/σ for NACA 16 series sections of 6%, 9%, and 12% thickness/chord ratios at $\alpha = 4^\circ$ —non-linear theory	140
D10. V vs. a/σ for NACA 16 series sections of 6%, 9%, and 12% thickness/chord ratios at $\alpha = 4^\circ$ —short cavity theory	141
D11. Cavity plots for NACA 16-006 thickness form at $\alpha = 4^\circ$ —linear theory including leading edge corrections	142

<u>Figure</u>	<u>Page</u>
D12. Cavity plots for NACA 16-009 thickness form at $\alpha = 4^\circ$ —linear theory including leading edge corrections	143
D13. Cavity plots for NACA 16-012 thickness form at $\alpha = 4^\circ$ —linear theory including leading edge corrections	144

LIST OF TABLES

<u>Table</u>	
1. α/σ for flat plate	48
2. Cavity volume V for flat plate at $\alpha = 1$ rad	48
3. Cavity source distribution $q(x)$ for flat plate at $\alpha = 1$ rad and $l = 0.5$	49
4. Cavity thickness distribution $h(x)$ for flat plate at $\alpha = 1$ rad and $l = 0.5$	50
5. Cavitation number σ for parabolic camber of $\lambda = 0.4$ at $\alpha = 0^\circ$	51
6. Cavity volume V for parabolic camber of $\lambda = 0.4$ at $\alpha = 0^\circ$	51
7. Flat plate at $\alpha = 1$ rad, cavitation number	76
8. Flat plate at $\alpha = 1$ rad, cavity volume V	76
9. Elliptic foil with $\epsilon = 1$ at $l = 2$	77
10. Elliptic foil with $\epsilon = 1$ at $l = 2$, cavity source distribution $q(x)$	77
11. Elliptic foil with $\epsilon = 1$ at $l = 2$, cavity thickness distribution $h(x)$	78
12. Experimental results for foil No. 3	111
13. Experimental results for foil No. 2	111
D1. Input data for the NACA 16 thickness forms at $\alpha = 4^\circ$	131

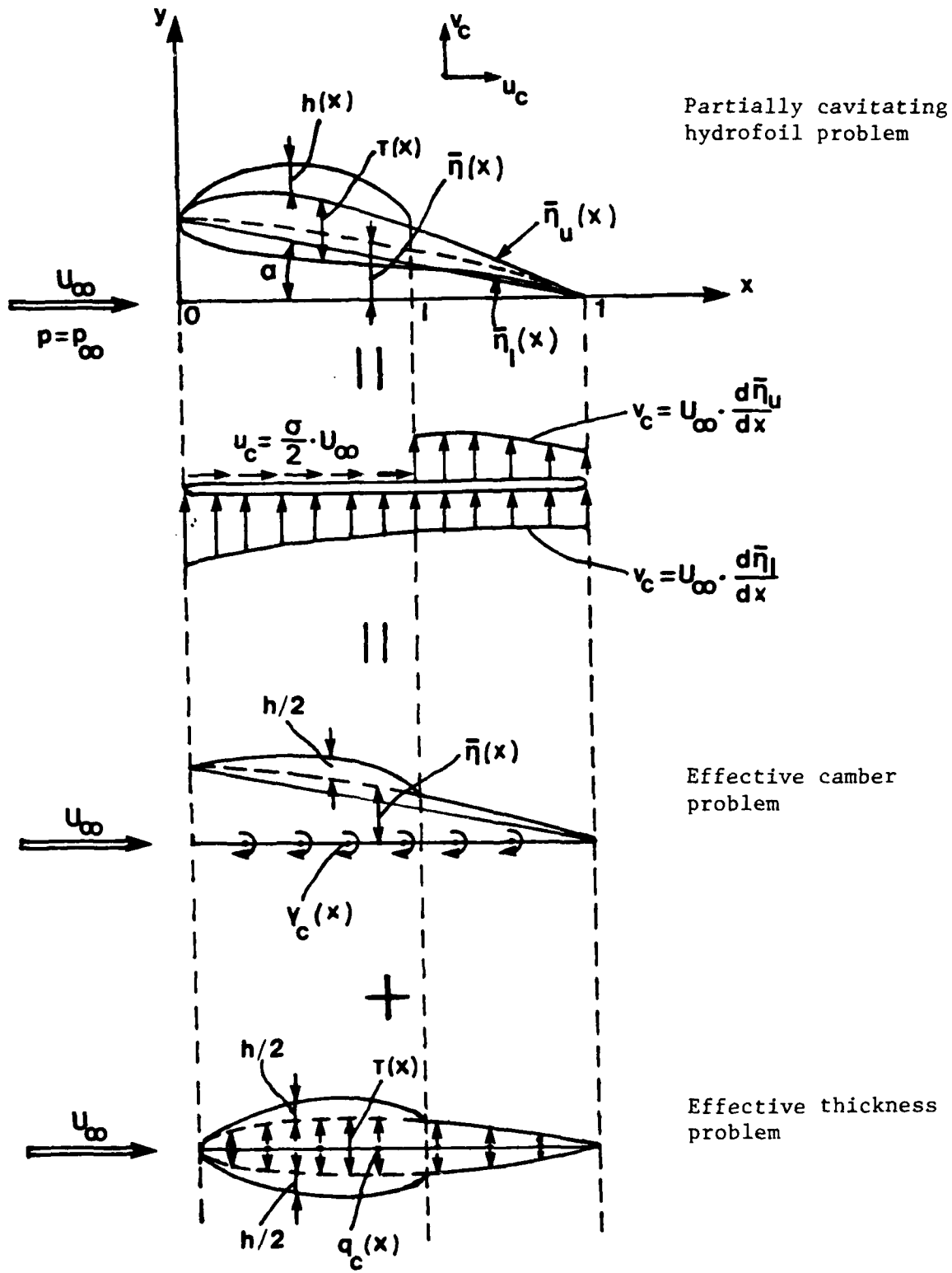


Figure 2. Partially cavitating hydrofoil - Linear theory

density of the fluid, we define the cavitation number σ as:

$$\sigma = \frac{p_{\infty} - p_c}{\frac{\rho}{2} \cdot U_{\infty}^2} \quad (2.1)$$

The cavity thickness $h(x)$ has to be determined as a part of the solution to the problem. The point on the hydrofoil where the cavity starts can be determined by the Villat-Brillouin condition [4,40] according to which the curvature of the cavity and foil should be continuous at that point. The end region of the cavity can be simulated by using any cavity termination model, for example, the modified Riabouchinsky model or the reentrant jet model. A review of the proposed models is included in [35].

Linear theory can be applied if the slopes of the hydrofoil and cavity surfaces with respect to the main stream are of the order of our small parameter ϵ , which can be for example the maximum thickness over chord ratio. In that case the boundary conditions are applied on the slit from $x=0$ to $x=1$ as we can see in Figure 2. If $\bar{\eta}_u(x)$ and $\bar{\eta}_l(x)$ are the upper and lower surfaces of the hydrofoil respectively, and (u_c, v_c) the perturbation velocity flow field, then the linearized boundary conditions, as demonstrated in [34], will be:

The kinematic boundary condition

$$v_c(x, 0+) = U_{\infty} \cdot \frac{\partial \bar{\eta}_u}{\partial x} ; \quad 0 < x < 1 \quad (2.2)$$

$$v_c(x, 0-) = U_{\infty} \cdot \frac{\partial \bar{\eta}_l}{\partial x} ; \quad 0^* < x < 1 \quad (2.3)$$

*Throughout our analysis it has been assumed that the cavity starts at the leading edge of the hydrofoil. This is further discussed in Section 22.

The streamwise perturbation velocity u_w^c on the slit $0 \leq x \leq l$ will be given as:

$$u_w^c(x, 0+) = - u_w^c(x, 0-) = \frac{\gamma_w(x)}{2} \quad (1.4)$$

The thickness problem:

The thickness distribution $\tau(x)$ is represented by the source distribution $q_w^\tau(x)$. The linearized kinematic boundary condition will be:

$$U_\infty \cdot \frac{1}{2} \cdot \frac{\partial \tau}{\partial x} = v_w^\tau(x, 0+) = - v_w^\tau(x, 0-) = \frac{q_w^\tau(x)}{2} \quad (1.5)$$

Therefore the source distribution will be:

$$q_w^\tau(x) = U_\infty \cdot \frac{\partial \tau}{\partial x} \quad (1.6)$$

and the streamwise perturbation velocity u_w^τ on the slit $0 \leq x \leq l$:

$$u_w^\tau(x, 0+) = u_w^\tau(x, 0-) = - \frac{1}{2\pi} \cdot \int_0^l \frac{q_w^\tau(\xi) \cdot d\xi}{\xi - x} \quad (1.7)$$

2. Partially cavitating hydrofoil - Linear theory.

Consider the same hydrofoil as in the previous section but now with a cavity of length ℓ on its upper surface as shown in Figure 2. If p_c is the corresponding pressure inside the cavity and ρ the

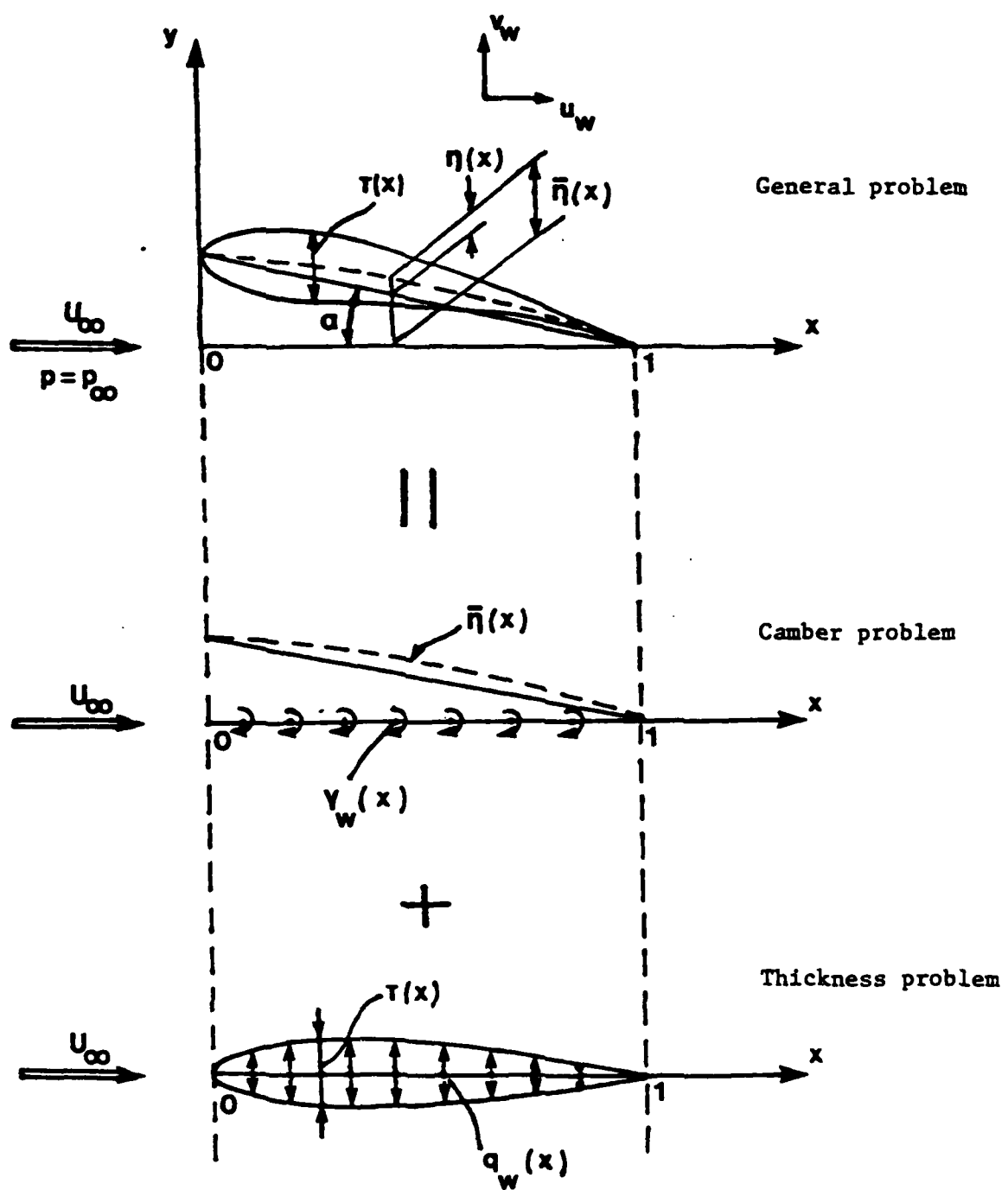


Figure 1. Hydrofoil in non-cavitating flow - Linear theory

PART A. PARTIALLY CAVITATING HYDROFOIL--LINEAR THEORY

1. Hydrofoil in non-cavitating flow - Linear theory.

Consider a hydrofoil of chord-length $c=1$, camber distribution $\bar{\eta}(x)$ (including the angle of attack α) and thickness distribution $\tau(x)$ in a uniform flow stream U_∞ and ambient pressure p_∞ , as illustrated in Figure 1. According to linear theory described in more detail in [28] the perturbation velocity flow field (u_w, v_w) can be generated by a distribution of vortices $\gamma_w(x)$ and sources $q_w(x)$ on the slit from $x=0$ to $x=1$. Furthermore the general hydrofoil problem can be decomposed in the following problems:

The camber problem:

The camber distribution $\bar{\eta}(x)$ is represented by the vortex distribution $\gamma_w(x)$. The linearized kinematic boundary condition will be:

$$U_\infty \cdot \frac{\partial \bar{\eta}}{\partial x} = v_w^c(x, \pm 0) = \frac{1}{2\pi} \cdot \int_0^1 \frac{\gamma_w(\xi) \cdot d\xi *}{\xi - x}; \quad 0 < x < 1 \quad (1.1)$$

The Kutta-condition at the trailing edge of the hydrofoil will be:

$$\gamma_w(1) = \text{finite} \quad (1.2)$$

Inversion of the singular integral equation of Cauchy type (1.1) in combination with (1.2) will give us the unique solution:

$$\gamma_w(x) = - \frac{2}{\pi} \cdot \sqrt{\frac{1-x}{x}} \cdot \int_0^1 \sqrt{\frac{\xi}{1-\xi}} \cdot \frac{U_\infty \cdot \frac{\partial \bar{\eta}}{\partial \xi}}{\xi - x} \cdot d\xi \quad (1.3)$$

*The symbol \int denotes the Cauchy principal value of the singular integral.

supercavitating hydrofoils is formulated in a uniform way and the solution is given in terms of integrals of known functions. Then the non-linear foil thickness effects are introduced by incorporating Lighthill's correction in the linearized version of the cavitating hydrofoil problem. That leads to an equivalent linear problem with the described streamwise perturbation velocity varying, rather than constant, over the cavity length. The present theory is found to predict a higher reduction in the cavity size than that by Uhlman, by increasing the foil thickness, but it is not as high as that predicted by Tulin and Hsu. Finally, the present theory is expected to be easily implemented into the cavitating propeller program via a three-dimensional version of Lighthill's correction. This is expected to result in a negligible change in the computing time.

Numerical methods have also been developed for the analysis of the cavitating hydrofoil or wing problem in linear theory. First, the discrete vortex and source method has been applied to a cavitating flat plate [14]. Then an unsteady lifting surface theory has been produced for a supercavitating wing, by using a vortex-source lattice technique [17]. Finally, this numerical method has been extended to predict the unsteady sheet cavitation of marine propellers operating in non-uniform wakes [24,19,21]. It has been observed that the numerical linear theory overpredicts the extent and volume of the cavities for certain propeller applications. This has been attributed to the inability of the linear theory to include non-linear foil thickness effects on the cavitation of hydrofoils.

Tulin and Hsu developed their short cavity theory [36] by considering the cavitating flow as a small perturbation on the non-linear fully wetted flow. Thus they were able to include non-linear foil thickness effects in their formulation. Namely, they predicted that by increasing the thickness of a partially cavitating hydrofoil, the size of the cavity was reduced substantially for fixed flow conditions.

Uhlman [38] formulated a non-linear numerical method for the analysis of partially cavitating hydrofoils by using surface singularity techniques and by applying the exact boundary conditions on the cavity and on the foil. His method also predicted a reduction in the size of the cavity as the foil thickness increased, but not as high as that by Tulin and Hsu. However, the computing time of his numerical scheme was long and therefore it was difficult to be implemented efficiently into the cavitating propeller program [21].

In this thesis, first the linear theory for partial and

of using the hodograph technique to deal with curved body boundaries, very few cases have been treated analytically by using the exact non-linear theory.

Linear theory was first applied by Tulin [34] to the problem of a supercavitating flat plate at small angles and arbitrary cavitation numbers. It was subsequently extended by T. Y. Wu [42], Geurst [11], Parkin [30], and Fabula [8] for a supercavitating hydrofoil of general shape. These authors have worked by means of the complex velocity function, and have given expressions for the cavitation number, the hydrodynamic coefficients and the cavity volume, in terms of integrals of known quantities.

The partially cavitating hydrofoil problem has first been addressed in linear theory by Acosta [1], Geurst and Timman [9] independently, who gave analytical results for a flat plate inclined to a uniform inflow. Geurst [10] also formulated the linear theory for partially cavitating camber meanlines and gave analytical results for a parabolic camber distribution [12]. The foil thickness was first included by Wade [41] who analyzed the partially cavitating planoconvex hydrofoil problem.

Hamaoka [16] stated the linear partial and supercavitating hydrofoil problem in terms of integral equations of unknown distributions of sources and dipoles on the foil and on the cavity. Inversion of these integral equations produced integral representations for the cavitation number, the hydrodynamic coefficients and the slope of the cavity surface in terms of the shape of the hydrofoil. He also gave series representations for his results when the hydrofoil shape could be expressed in terms of polynomials of the chordwise coordinate.

INTRODUCTION

Cavitation is the phenomenon in which a cavity of gas exists inside a flow stream, due to the development of pressures lower than the saturation pressure at the local temperature.

This is very likely to occur on the suction side of a hydrofoil or on the backface of propeller blades. Since in our time ships become larger and propeller loadings bigger, cavitation becomes more and more inevitable without any considerable sacrifice in propulsion efficiency and therefore fuel consumption.

On the other hand, unsteady propeller blade cavitation, which is the most usual case, is undesirable. One of the reasons is the chance of failure at the propeller trailing edge, due to the impulsive loads during the collapse stage of the unsteady cavity. However, the most important reason is that unsteady cavitation is the main contributor to unsteady hull forces, which often cause severe vibrations and structural failure in some ships.

In order to design an efficient propeller with a low level of cavitation, a thorough understanding of the phenomenon of cavitation is desirable.

Cavitating or free-streamline flows have been studied extensively during the last century with increasing interest. The first problems to be addressed were those of flows around bodies at zero cavitation number. The analysis of these problems has been achieved via the hodograph technique [3]. The extension to non-zero cavitation number problems has created a lot of diversity in the cavity termination models. The most prevailing models seem to have been the Riabouchinsky model [32] and the re-entrant jet model [6]. Due to the difficulty

r_L : Leading edge radius of the hydrofoil
 σ : Cavitation number defined as:
$$\sigma = \frac{p_\infty - p_c}{\frac{\rho \cdot U_\infty^2}{2}}$$

 σ_{inc} : Inception cavitation number
 σ_L : Cavitation number in pure linear theory
 $\tau(x)$: Thickness distribution of the hydrofoil (see Figure 1)
 τ_{max} : Maximum thickness/chord ratio for the hydrofoil
 $\tau_{T.E.}$: Thickness at the trailing edge/chord ratio for the hydrofoil
 ϕ : Transformed ξ variable defined as $\xi = l \cdot \sin^2(\frac{\phi}{2})$; $0 \leq \xi \leq l$
 and $0 \leq \phi \leq \pi$
 ϕ_i : Discrete ϕ defined in (8.7)
 $\phi(\eta; s)$: Function defined in (6.6)
 w : Dummy z variable

Superscripts

c : Refers to the camber problem
 t : Refers to the thickness problem
 α : Refers to the flat plate problem at angle of attack
 $+$: Refers to the upper hydrofoil surface
 $-$: Refers to the lower hydrofoil surface
 1 : Corresponds to No. 1 hydrofoil (see Section 24)
 2 : Corresponds to No. 2 tested hydrofoil (see Section 24)
 3 : Corresponds to No. 3 tested hydrofoil (see Section 24)

$\gamma_w(x)$: Vortex distribution for the non-cavitating hydrofoil problem (see Figure 1)

γ_i : Maximum of the vortex distribution for NACA $a = m$ camber meanline at $\alpha = \alpha_i$ (see Figure 5a)

δ : Thickness at the end of the cavity (see Figure 32a)

$\Delta\alpha$: Increment in the angle of attack

$\Delta\sigma$: Change in σ due to open cavity model

ϵ : Perturbation parameter for the cavitating hydrofoil problem.
 Also ratio of the minor to the major axis for an ellipse

n : Dummy z variable

$n(x)$: Camber distribution of the hydrofoil without including the angle of attack (see Figure 1)

n_{max} : Maximum camber/chord ratio of the hydrofoil

$\bar{n}(x)$: Camber distribution of the hydrofoil including the angle of attack (see Figure 1)

$\bar{n}_c(x)$: Cavity surface distribution

$\bar{n}_l(x)$: Lower hydrofoil surface distribution (see Figure 2)

$\bar{n}_u(x)$: Upper hydrofoil surface distribution (see Figure 2)

θ : Transformed n variable defined from the expression $n = s \cdot \sin^2(\frac{\theta}{2})$
 for partially cavitating or $n = t \cdot \sin^2(\frac{\theta}{2})$ for supercavitating hydrofoils; $0 < \theta < \pi$

$\theta^*(x)$: Hydrofoil slope, defined as: $\theta^*(x) = \frac{1}{\sigma} \cdot \frac{\partial \bar{n}_l}{\partial x}$.

λ : The maximum camber/chord ratio for a parabolic camber meanline, doubled (see Figure 4b)

μ : Maximum thickness/chord ratio for a biconvex hydrofoil (see Figure 4c)

ξ : Dummy x variable

ρ : Density of the fluid

u_c : x-component of the perturbation velocity with respect to U_∞
 for the cavitating hydrofoil problem (see Figures 2 and 15)

u_v : x-component of the perturbation velocity with respect to U_∞
 for the non-cavitating hydrofoil problem (see Figure 1)

U_∞ : Free stream velocity

v_c : y-component of the perturbation velocity with respect to U_∞
 for the cavitating hydrofoil problem (see Figures 2 and 15)

$v_{in}(x)$: Induced velocity distribution in the wake of the hydrofoil

v_v : y-component of the perturbation velocity with respect to U_∞
 for the non-cavitating hydrofoil problem (see Figure 1)

$\bar{v}(x)$: Nondimensional $v_{in}(x)$, defined as: $\bar{v}(x) = \frac{v_{in}(x)}{\sigma \cdot U_\infty}$

V : Cavity volume, non-dimensionalized with respect to c^2 ; for
 supercavitating hydrofoils, includes also the foil.

(x,y) : Coordinate system for the hydrofoil (see Figure 1)

x_{min} : x-coordinate of the minimum pressure point on the hydrofoil

z : Transformed x variable defined as $z = \sqrt{\frac{x}{1-x}}$; $0 < x < 1$ for the
 partially cavitating and as $z = \sqrt{\frac{x}{1-x}}$; $0 < x < l$ for the
 supercavitating hydrofoil problem

α : Angle of attack of the free stream with respect to the
 hydrofoil (see Figure 1)

α_i : Ideal angle of attack

$\gamma(x)$: Cavity vortex distribution defined as:

$$\gamma(x) = \gamma_c(x) - \gamma_v(x)$$

$\bar{\gamma}(x)$: Nondimensional vortex distribution for the supercavitating
 hydrofoil problem, defined as: $\bar{\gamma}(x) = \frac{\gamma_c(x)}{\sigma \cdot U_\infty}$

$\gamma_c(x)$: Vortex distribution for the cavitating hydrofoil
 problem (see Figures 2 and 15)

discrete cavity thickness distribution.

p_c : Vapor pressure of the fluid or pressure inside the cavity

p_∞ : Free stream pressure

ρ : Constant defined in (18.5)

$q(x)$: Cavity source distribution defined as $q(x) = q_c(x) - q_v(x)$

$\bar{q}(x)$: Nondimensional source distribution for the supercavitating hydrofoil problem, defined as: $\bar{q}(x) = \frac{q_c(x)}{\sigma \cdot U_\infty}$

$q_c(x)$: Source distribution for the cavitating hydrofoil problem (see Figures 2 and 15)

$q_v(x)$: Source distribution for the non-cavitating hydrofoil problem (see Figure 1)

$q_s(x)$: Surface velocity on the hydrofoil or on the cavity

$Q(Q_c)$: Any quantity depending linearly on the solution $\sigma, \gamma(x), q(x)$
 $(\sigma, \gamma_c(x), q_c(x))$ for the partially cavitating
(supercavitating) hydrofoil problem

Q_v : Any quantity depending linearly on the solution

$\gamma_v(x), q_v(x)$ for the non-cavitating hydrofoil problem

r : Constant defined as $r = (1 + s^2)^{1/4}$ for the partially cavitating and as $r = (1+t^2)^{1/4}$ for the supercavitating hydrofoil problem

R : Constant defined in (18.5)

$R(\omega, z)$: Integral defined in (A.24a)

s : Constant in the partially cavitating hydrofoil problem defined as $s = (\ell/(1-\ell))^{1/2}$

s_0 : Constant defined as $s_0 = (\ell_0/(1-\ell_0))^{1/2}$

t : Constant in the supercavitating hydrofoil problem defined as $t = 1/(\ell-1)^{1/2}$

NOMENCLATURE

$a(\rho_L; \ell)$: Leading edge radius correction factor defined in (21.9)

$\bar{a}(\rho_L; \ell, \ell_0)$: Integral defined in (22.21)

A: Constant defined in (5.2)

B: Constant defined in (5.2)

c: Chord-length of the hydrofoil

c(x): Camber distribution of the cavity (see Figure 15)

C_1, C_2, C_3, C_4, C_5 : Constants defined in Appendix C

C_D : Drag coefficient

C_L : Lift coefficient

C_M : Moment coefficient

D: Constant defined as $D = \frac{\pi}{4} \cdot \frac{(r^2 - 1)}{4 \cdot r}$

E: Constant defined in (6.7)

f(n;s): Function defined in (5.9)

$\bar{f}(n;s, s_0)$: Function defined in (22.16)

F: Constant defined in (6.8)

h(x): Cavity thickness distribution--for supercavitating hydrofoils,
includes also the foil thickness (see Figure 15)

h_i : Discrete cavity thickness distribution

I(n;s): Integral defined in (5.7)

$\bar{I}(n;s, s_0)$: Integral defined in (C-3)

J(n;t): Integral defined in (A.23)

K: Number of uniform intervals to apply Simpson's integration

ℓ_0 : x coordinate of the start of the cavity

ℓ : x coordinate of the end of the cavity

m: Extent of the γ_i for NACA $a = m$ camber meanline

M: Constant defined in (7.6a)

N: Constant defined in (7.6b). Also number of points for the

The dynamic boundary condition

$$u_c(x, 0+) = \frac{\sigma}{2} \cdot U_\infty; \quad 0^* < x < l \quad (2.4)$$

The perturbation velocity flow field (u_c, v_c) can again be generated by a distribution of vortices $\gamma_c(x)$ and sources $q_c(x)$ on the slit from $x=0$ to $x=1$. The problem can be again decomposed into the effective camber and effective thickness problems as shown in Figure 2, provided that the cavity thickness distribution is known.

The boundary conditions (2.2), (2.3) and (2.4) in terms of the unknown distributions $\gamma_c(x)$ and $q_c(x)$ will become:

$$v_c(x, 0+) = \frac{q_c(x)}{2} + \frac{1}{2\pi} \cdot \int_0^1 \frac{\gamma_c(\xi) \cdot d\xi}{\xi - x} = U_\infty \cdot \frac{\partial \bar{\eta}_u}{\partial x} \quad (2.5)$$

for: $l < x < 1$

$$v_c(x, 0-) = - \frac{q_c(x)}{2} + \frac{1}{2\pi} \cdot \int_0^1 \frac{\gamma_c(\xi) \cdot d\xi}{\xi - x} = U_\infty \cdot \frac{\partial \bar{\eta}_l}{\partial x} \quad (2.6)$$

for: $0 < x < l$

$$u_c(x, 0+) = \frac{\gamma_c(x)}{2} - \frac{1}{2\pi} \cdot \int_0^1 \frac{q_c(\xi) \cdot d\xi}{\xi - x} = \frac{\sigma}{2} \cdot U_\infty \quad (2.7)$$

for: $0 < x < l$

The Kutta condition at the trailing edge of the hydrofoil has also to be introduced as:

$$\gamma_c(1) = \text{finite} \quad (2.8)$$

The cavity thickness distribution $h(x)$ can be determined from the

kinematic boundary condition on the cavity surface:

$$v_c(x, 0+) = \frac{q_c(x)}{2} + \frac{1}{2\pi} \cdot \int_0^1 \frac{\gamma_c(\xi) \cdot d\xi}{\xi - x} = U_\infty \cdot \frac{\partial}{\partial x} (\bar{n}_u + h) \quad (2.9)$$

for: $0 < x < l$

But $\bar{n}_u(x)$ and $\bar{n}_l(x)$ can be expressed as:

$$\bar{n}_u(x) = \bar{n}(x) + \frac{\tau(x)}{2} \quad (2.10)$$

$$\bar{n}_l(x) = \bar{n}(x) - \frac{\tau(x)}{2} \quad (2.11)$$

Subtracting (2.6) from (2.9) and using (2.10), (2.11) and (1.6), we get:

$$q_c(x) - q_w(x) = U_\infty \cdot \frac{\partial h}{\partial x}; \quad 0 < x < l \quad (2.12)$$

Substituting (2.10) and (2.11) in (2.5) and (2.6) and having in mind (1.1) and (1.6), we get:

$$\frac{q_c(x) - q_w(x)}{2} + \frac{1}{2\pi} \cdot \int_0^1 \frac{\gamma_c(\xi) - \gamma_w(\xi)}{\xi - x} \cdot d\xi = 0; \quad l < x < 1 \quad (2.13)$$

$$-\frac{q_c(x) - q_w(x)}{2} + \frac{1}{2\pi} \cdot \int_0^1 \frac{\gamma_c(\xi) - \gamma_w(\xi)}{\xi - x} \cdot d\xi = 0; \quad 0 < x < l \quad (2.14)$$

Combining (2.13) and (2.14) we finally get:

$$q_c(x) = q_w(x); \quad l < x < 1 \quad (2.15)$$

$$-\frac{q_c(x) - q_w(x)}{2} + \frac{1}{2\pi} \cdot \int_0^1 \frac{\gamma_c(\xi) - \gamma_w(\xi)}{\xi - x} \cdot d\xi = 0; \quad 0 < x < l \quad (2.16)$$

We define the cavity source $q(x)$ and cavity vortex $\gamma(x)$ distributions as:

$$q(x) = q_c(x) - q_w(x) \quad (2.17)$$

$$\gamma(x) = \gamma_c(x) - \gamma_w(x) \quad (2.18)$$

Then the equations (2.12), (2.15) and (2.16) become:

$$q(x) = U_\infty \cdot \frac{\partial h}{\partial x}; \quad 0 < x < l \quad (2.19)$$

$$q(x) = 0; \quad l < x < 1 \quad (2.20)$$

$$-\frac{q(x)}{2} + \frac{1}{2\pi} \cdot \int_0^1 \frac{\gamma(\xi) \cdot d\xi}{\xi - x} = 0; \quad 0 < x < l \quad (2.21)$$

The dynamic boundary condition (2.7) can also be expressed in terms of $q(x)$, $\gamma(x)$ as:

$$\frac{\gamma(x)}{2} - \frac{1}{2\pi} \cdot \int_0^l \frac{q(\xi) \cdot d\xi}{\xi - x} - \frac{\sigma}{2} \cdot U_\infty = -\frac{\gamma_w(x)}{2} + \frac{1}{2\pi} \cdot \int_0^1 \frac{q_w(\xi) \cdot d\xi}{\xi - x} \quad (2.22)$$

$$0 < x < l$$

The right hand side of (2.22) is the negative of the perturbation velocity $u_w(x, 0+)$ on the upper side of the hydrofoil in non-cavitating flow, as it can be seen from (1.1) and (1.7).

The Kutta condition will become:

$$\gamma(1) = \text{finite} \quad (2.23)$$

In the preceding analysis nothing has been said about the trailing edge of the cavity. In the nonlinear theory using Riabouchinsky or reentrant jet models it has been proven in [13] that the thickness at the end of the cavity is of order of ϵ^2 . Therefore in linear theory we require that:

$$h(l) = 0 \quad (2.24)$$

or by integrating (2.19) we get the so-called cavity closure condition:

$$\int_0^l q(\xi) d\xi = 0 \quad (2.25)$$

The final system of singular integral equations is:

$$-\frac{q(x)}{2} + \frac{1}{2\pi} \cdot \int_0^1 \frac{\gamma(\xi) d\xi}{\xi - x} = 0; \quad 0 < x < l \quad (2.21)$$

$$\frac{\gamma(x)}{2} - \frac{1}{2\pi} \cdot \int_0^l \frac{q(\xi) d\xi}{\xi - x} - \frac{\sigma}{2} \cdot U_\infty = -u_w(x, 0+) \quad (2.26)$$

for: $0 < x < l$

$$\gamma(1) = \text{finite} \quad (2.23)$$

$$\int_0^l q(\xi) d\xi = 0 \quad (2.25)$$

The unknowns are σ , $q(x)$ and $\gamma(x)$. The solution corresponding to a certain cavity length l depends only on the distribution of $u_w(x, 0+)$ for $0 < x < l$ and is unique, as will be proven in Section 4.

3. Decomposition in the partially cavitating hydrofoil problem.

The non-cavitating hydrofoil problem can be decomposed, in linear theory, into the camber, the thickness and the angle of attack (or flat plate) problems. If Q_w is any quantity depending linearly on the distributions $q_w(x)$ and $\gamma_w(x)$, then:

$$Q_w = Q_w^c + Q_w^\tau + Q_w^\alpha \quad (3.1),$$

where the superscripts c, τ, α correspond to the camber, the thickness and the angle of attack problems respectively. The total camber $\bar{n}(x)$ has been decomposed as:

$$\bar{n}(x) = n(x) + \alpha \cdot (1-x) \quad (3.2)$$

where $n(x)$ is the hydrofoil camber and α the angle of attack as defined in Figure 1.

If we put $Q_w = u_w(x, 0+)$ in (3.1) then:

$$u_w(x, 0+) = u_w^c(x, 0+) + u_w^\tau(x, 0+) + u_w^\alpha(x, 0+) \quad (3.3)$$

Since the right hand side of equations (2.21), (2.26), (2.23), (2.25) can be decomposed as in (3.3), the same is true for the solution σ , $q(x)$, $\gamma(x)$:

$$\sigma = \sigma^c + \sigma^\tau + \sigma^\alpha \quad (3.4)$$

$$q = q^c + q^\tau + q^\alpha \quad (3.5)$$

$$\gamma = \gamma^c + \gamma^\tau + \gamma^\alpha \quad (3.6)$$

Furthermore, for any quantity Q depending linearly on the solution it will be true:

$$Q = Q^c + Q^\tau + Q^\alpha \quad (3.7)$$

where Q can be, for example:

-the cavity thickness distribution $h(x)$

- the cavity volume V
- the lift coefficient, C_L
- the moment coefficient, C_M
- the square root of drag coefficient, $\sqrt{C_D}$

Therefore, the partially cavitating hydrofoil problem can be decomposed into the camber, the thickness and the flat plate problems, all corresponding to the same cavity length l , as it is depicted in Figure 3. Some of these elementary problems possibly have no physical meaning, i.e. they result in negative or convex cavities, but if combined with the appropriate angle of attack they give meaningful solutions to our problems as illustrated in Figures 10 and 11.

As an application, the following special cases can be examined:

a) Change in angle of attack:

If we change the angle of attack of a partially cavitating hydrofoil by $\Delta\alpha$, then the solution for the same cavity length will change by an amount which is the solution to a flat plate at angle of attack $\Delta\alpha$ and the same cavity length.

b) Change of the camber/chord ratio:

For a given camber meanline shape partially cavitating at zero angle of attack, if we change the camber/chord ratio by a factor, then the solution for the same cavity length changes by the same factor.

A similar relationship holds for affine thickness forms.

Therefore for a given camber or thickness series partially cavitating at a cavity length l , we need to solve the problems for one value of the similarity parameter and one angle of attack.

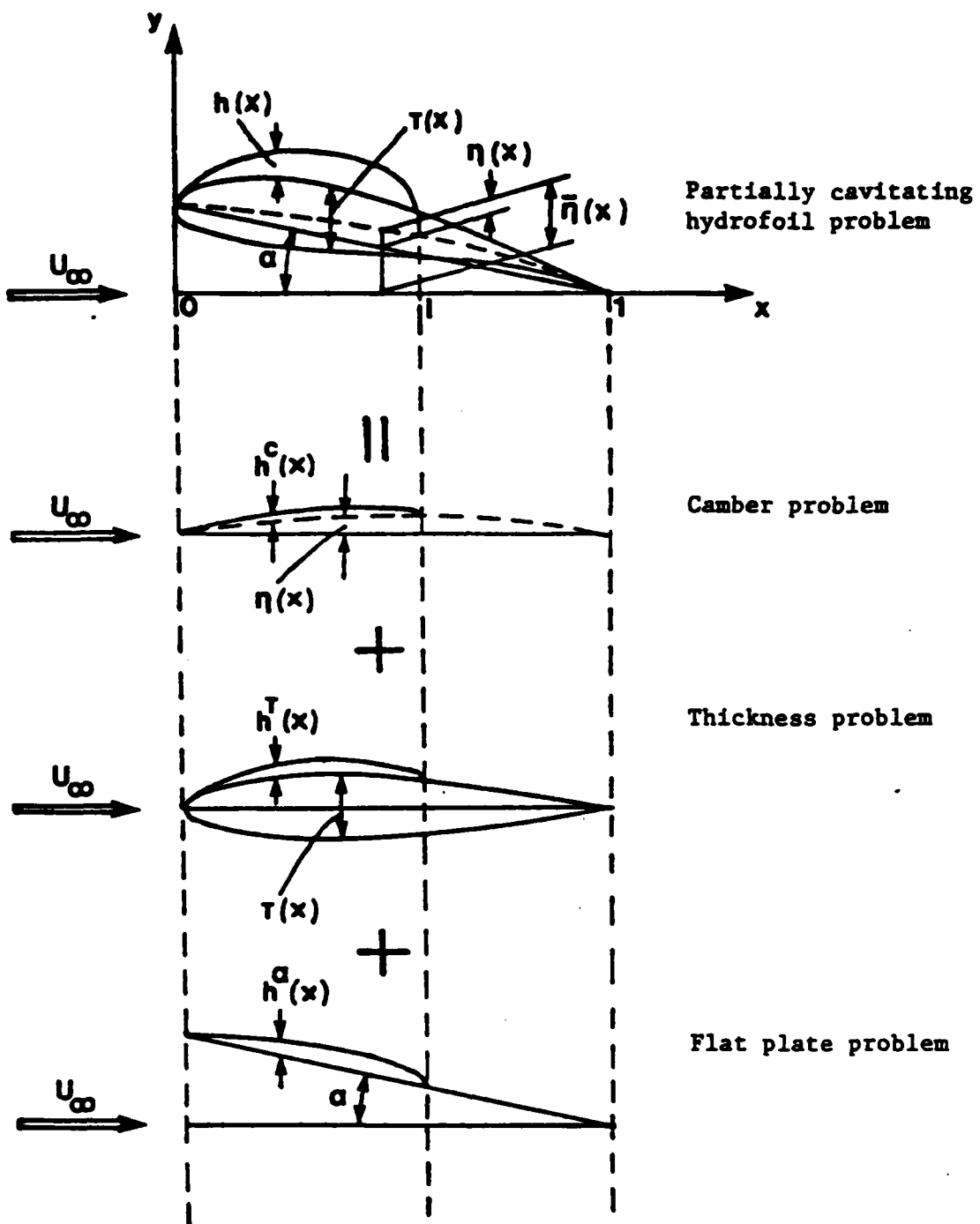


Figure 3. Decomposition of the partially cavitating hydrofoil problem into the camber, thickness, and flat plate problems.

4. Solution to the partially cavitating hydrofoil problem.

We have to solve the linear system of singular integral equations (2.21), (2.26) in combination with the restrictions (2.23), (2.25).

We first invert the equation (2.21) by using the formulas (1.1) and (1.3):

$$\gamma(x) = -\frac{1}{\pi} \cdot \sqrt{\frac{1-x}{x}} \cdot \int_0^l \sqrt{\frac{\xi}{1-\xi}} \cdot \frac{q(\xi)}{\xi-x} \cdot d\xi \quad (4.1)$$

The solution (4.1) already satisfies the Kutta condition (2.23) and is unique as long as $q(x)$ is. Substituting in (2.26) $\gamma(x)$ from (4.1) we get the following integral equation for $q(x)$:

$$\frac{1}{2\pi} \int_0^l (\sqrt{\frac{\xi}{1-\xi}} + \sqrt{\frac{x}{1-x}}) \cdot \frac{q(\xi)}{\xi-x} \cdot d\xi = (\frac{\sigma}{2} \cdot U_\infty - u_w^+) \cdot \sqrt{\frac{x}{1-x}} \quad (4.2)$$

We now introduce the following transformation as suggested by Hamaoka in [11]:

$$z = \sqrt{\frac{x}{1-x}}, \quad \eta = \sqrt{\frac{\xi}{1-\xi}}, \quad s = \sqrt{\frac{l}{1-l}}$$

(4.3)

$0 < x, \quad \xi \leq l \text{ and } 0 < z, \quad \eta \leq s$

and equation (4.2) becomes:

$$\frac{1}{2\pi} \cdot \int_0^s \frac{\eta \cdot q(\eta)}{(1+\eta^2)} \cdot \frac{d\eta}{(z-\eta)} = \frac{1}{2} \cdot \frac{z}{1+z^2} \cdot (\frac{\sigma \cdot U_\infty}{2} - u_w^+) \quad (4.4)$$

which is in a form similar to equation (1.1).

Inversion of (4.4) in combination with the requirement that the

cavity source is square root singular at the trailing edge of the cavity [43], renders the solution.

$$q(z) = \frac{1}{\pi} \cdot \frac{(1+z)^2}{\sqrt{z \cdot (s-z)}} \cdot \int_0^s \frac{\sqrt{\eta(s-\eta)}}{1+\eta^2} \cdot [u_w^+ - \frac{\sigma \cdot U_\infty}{2}] \cdot \frac{1}{z-\eta} \cdot d\eta \quad (4.5)$$

which is unique as long as σ is.

Equations (4.5) and (4.1) give us the formal unique solution to the general partially cavitating hydrofoil problem as soon as we determine the corresponding cavitation number σ .

5. Cavitation number σ

By using (A.19) equation (4.5) becomes:

$$q(z) = \frac{1}{\pi} \cdot \frac{(1+z)^2}{\sqrt{z \cdot (s-z)}} \cdot \int_0^s \frac{\sqrt{\eta \cdot (s-\eta)}}{1+\eta^2} \cdot u_w^+(\eta) \cdot \frac{1}{z-\eta} \cdot d\eta + \sigma \cdot U_\infty \cdot \frac{A-B \cdot z}{\sqrt{z \cdot (s-z)}} \quad (5.1)$$

where:

$$A = \frac{1}{2\sqrt{2}} \cdot \sqrt{r^2 - 1}, \quad B = \frac{1}{2\sqrt{2}} \cdot \sqrt{r^2 + 1}, \quad r^2 = \frac{1}{\sqrt{1-\lambda}} \quad (5.2)$$

To determine σ we have to apply the closure condition (2.25) which in terms of the transformation (4.3) becomes:

$$\int_0^s q(z) \cdot \frac{2z \cdot dz}{(1+z^2)^2} = 0 \quad (5.3)$$

Substituting (5.1) in (5.3) and using (A.11) and (A.12) we get:

$$\sigma = \frac{2}{U_{\infty} \cdot D} \cdot \int_0^s \frac{z}{\pi \sqrt{z(s-z)}} \cdot \frac{1}{1+z^2} \cdot dz \int_0^s \frac{\sqrt{n(s-n)}}{1+n^2} \cdot u_w^+ \cdot \frac{1}{z-n} \cdot dn \quad (5.4)$$

where:

$$D = \frac{\pi}{4 \cdot r} \cdot (r^2 - 1) \quad (5.5)$$

By using the Poincaré-Bertrand's formula (A.28) we change the order of integration in the double integral of (5.4) and we get:

$$\sigma = \frac{2}{U_{\infty} \cdot D} \int_0^s \frac{1}{\pi} \cdot \frac{\sqrt{n(s-n)}}{1+n^2} \cdot u_w^+ \cdot I(n; s) \cdot dn \quad (5.6)$$

where:

$$I(n; s) = \int_0^s \frac{\sqrt{z}}{\sqrt{s-z}} \cdot \frac{1}{1+z^2} \cdot \frac{1}{z-n} \cdot dz \quad (5.7)$$

The singular integral $I(n; s)$ is evaluated analytically in Appendix A.

Thus the final expression for σ becomes:

$$\sigma = \int_0^s \frac{2 \cdot u_w^+(n)}{U_{\infty}} \cdot f(n; s) \cdot dn \quad (5.8)$$

$$f(n; s) = \frac{2 \cdot \sqrt{2}}{\pi} \cdot \frac{\sqrt{n(s-n)}}{(1+n^2)^2} \cdot \frac{r^2}{r^2 - 1} \cdot [\sqrt{r^2 + 1} - n \cdot \sqrt{r^2 - 1}]$$

where:

$$(5.9)$$

with

$$r^2 = \sqrt{1+s^2} \quad (5.10)$$

Some plots of the function $f(n; s)$ for different values of n can be seen in Figure 6.

In other words, σ and $q(z)$ have been expressed in

(5.1) and (5.8) in terms of integrals of known functions over the cavity length. We observe again the dependence of the solution only on the distribution of the upper surface perturbation velocity u_w^+ in the non-cavitating flow. Similar expressions can also be derived for $\gamma(x)$, C_L , C_M , C_D (see also [16].)

In this work we focus more on the cavity shape than on the hydrodynamic characteristics of the cavitating hydrofoil. Thus we proceed by giving general expressions for the cavity volume V and the thickness distribution $h(x)$.

6. Cavity Volume V

The cavity thickness distribution comes from the integration of (2.19):

$$h(x) = \int_0^x \frac{q(\xi)}{U_\infty} \cdot d\xi \quad (6.1)$$

where we have made use of the boundary condition at the leading edge of the cavity:

$$h(0)=0 \quad (6.2)$$

The cavity volume V will be given as:

$$V = \int_0^l h(x) \cdot dx = x \cdot h \Big|_0^l - \int_0^l x \cdot \frac{dh}{dx} \cdot dx = - \int_0^l x \cdot \frac{q(x)}{U_\infty} \cdot dx \quad (6.3)$$

where we have made use of (6.2), (2.24) and (2.19).

In terms of the transformation (4.3) equation (6.1) becomes:

$$V = - \int_0^s \frac{q(z)}{U_\infty} \cdot \frac{2z^3}{(1+z^2)^3} \cdot dz \quad (6.4)$$

which by using (4.5), (A.28) and (A.21) finally renders:

$$V = \int_0^s \left(\frac{2 \cdot u_w^+ (\eta)}{U_\infty} - \sigma \right) \cdot \phi(\eta; s) \cdot d\eta \quad (6.5)$$

$$\phi(\eta; s) = \frac{\sqrt{\eta(s-\eta)}}{\sqrt{2} \cdot r^2 \cdot (1+\eta^2)^3} \cdot [(\sqrt{r^2+1} -$$

where:

$$= \eta \cdot \sqrt{r^2-1} - \frac{(1+\eta^2)}{4 \cdot r^6} \cdot (E + \eta \cdot F) \quad (6.6)$$

$$E = 2 \cdot s^2 \cdot \sqrt{r^2+1} + (s^3 - s) \cdot \sqrt{r^2-1} \quad (6.7)$$

$$F = (s^3 + 3 \cdot s) \cdot \sqrt{r^2+1} - 2 \cdot \sqrt{r^2-1} \quad (6.8)$$

7. Analytical solutions for some hydrofoils

As a first step to our solution we have to solve the non-cavitating hydrofoil problem in order to find u_w^+ , given as:

$$u_w^+(x) = u_w(x, 0+) = \frac{\gamma_w(x)}{2} - \frac{1}{2\pi} \cdot \int_0^1 \frac{q_w(\xi) \cdot d\xi}{\xi - x} \quad (7.1)$$

For the most camber meanlines used in practice, the vortex distribution $\gamma_w(x)$ is known, since they are designed to develop that load.

The thickness source distribution $q_w(x)$ is related to the thickness distribution $\tau(x)$ as in (1.6). The integral in (7.1) corresponds to the induced perturbation velocity $u_w^\tau(x, 0)$ due to the foil thickness, and for some special cases can be evaluated analytically.

Analytical results to the partially cavitating hydrofoil problem can be obtained as long as the integral in the expressions (5.1), (5.8) and (6.5) can be evaluated analytically. The following cases are considered as illustrated in Figure 4.

a. Flat plate

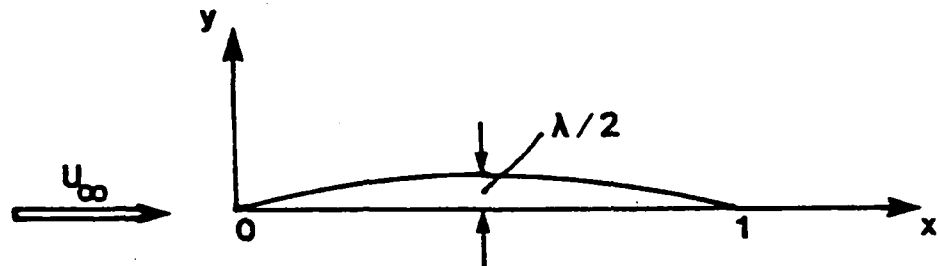
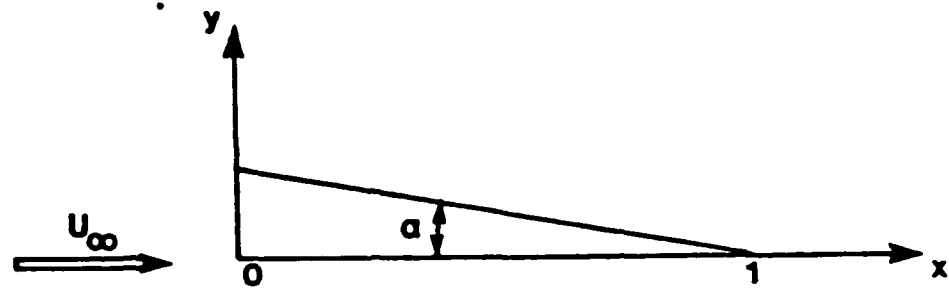
For the non-cavitating flow we have by using (1.3) with $\frac{\partial \bar{n}}{\partial \xi} = -\alpha$:

$$\gamma_w(x) = 2 \cdot U_\infty \cdot \alpha \cdot \sqrt{\frac{1-x}{x}}; \quad 0 \leq x \leq 1 \quad (7.2)$$

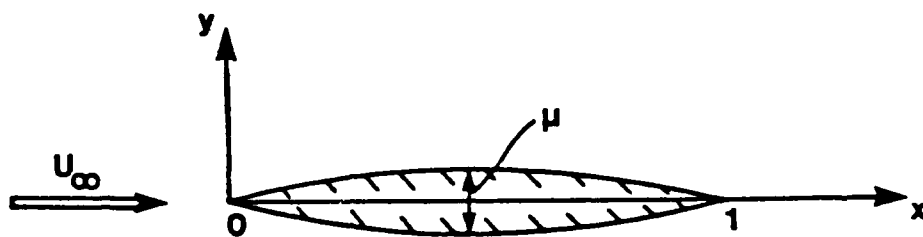
and by using (7.1) and (4.3):

$$u_w^+(\eta) = \frac{U_\infty \cdot \alpha}{\eta}; \quad 0 \leq \eta \leq s \quad (7.3)$$

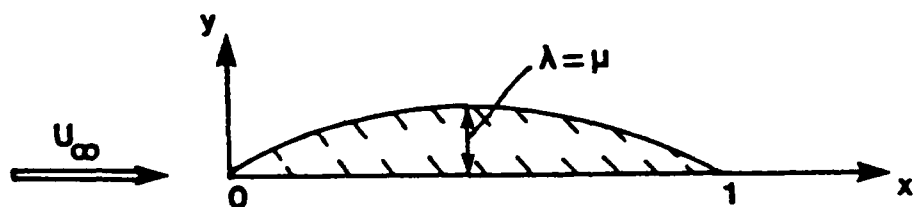
Substituting (7.3) in (5.8) and (5.1) and by using the formulas from Appendix A, we get (see also [10] and [31]):



(b) Parabolic camber



(c) Biconvex hydrofoil



(d) Planoconvex hydrofoil

Figure 4. Special cases of partially cavitating hydrofoils

Table 5

CAVITATION NUMBER σ FOR PARABOLIC CAMBER OF $\lambda = 0.4$ AT $\alpha = 0^\circ$				
λ	Analytical	Numerical		
		K = 20	K = 10	K = 5
0.1	0.4929822	0.4929822	0.4929822	0.4929822
0.3	0.8047841	0.8047841	0.8047841	0.8047825
0.5	0.9656854	0.9656854	0.9656854	0.9656083
0.7	1.0359341	1.0359341	1.0359341	1.0362429
0.9	0.9989466	0.9989466	0.9989687	1.0054026

Table 6

CAVITY VOLUME V FOR PARABOLIC CAMBER OF $\lambda = 0.4$ AT $\alpha = 0^\circ$				
λ	Analytical	Numerical		
		K = 20	K = 10	K = 5
0.1	-0.0003569	-0.0003569	-0.0003569	-0.0003569
0.3	-0.0050591	-0.0050591	-0.0050591	-0.0050595
0.5	-0.0162661	-0.0162661	-0.0162661	-0.0162791
0.7	-0.0332860	-0.0332860	-0.0332860	-0.0331346
0.9	-0.0550233	-0.0550233	-0.0550161	-0.0554519

Table 4

CAVITY THICKNESS DISTRIBUTION $h(x)$
FOR FLAT PLATE AT $\alpha = 1$ RAD AND $\ell = 0.5$

x	Numerical		
	N = 10	N = 20	N = 40
0.	0.	0.	0.
0.0006	0.0188053	0.0188283	0.0188298
0.0090	0.1370588	0.1371007	0.1371033
0.0407	0.3877945	0.3878217	0.3878234
0.1066	0.6975954	0.6975761	0.6975750
0.2	0.9307760	0.9307408	0.9307387
0.3	0.9944224	0.9944067	0.9944058
0.3866	0.8845249	0.8845262	0.8845263
0.45	0.6487553	0.6487611	0.6487616
0.4876	0.3402218	0.3402258	0.3402261
0.5	-0.0000009	-0.0000002	-0.0000001

Table 3

CAVITY SOURCE DISTRIBUTION $q(x)$
FOR FLAT PLATE AT $\alpha = 1$ RAD AND $\lambda = 0.5$

x	Analytical	Numerical		
		K = 20	K = 10	K = 3
0.00308	1.2809671	1.2809671	1.2809671	1.2805070
0.02725	0.6332379	0.6332379	0.6332379	0.6331418
0.07322	0.3967693	0.3967693	0.3967693	0.3967195
0.13650	0.2429593	0.2429593	0.2429593	0.2429246
0.21089	0.1160452	0.1160452	0.1160452	0.1160165
0.28911	-0.0075552	-0.0075552	-0.0075552	-0.0075820
0.36350	-0.1485767	-0.1485767	-0.1485767	-0.1486049
0.42677	-0.3445349	-0.3445349	-0.3445349	-0.3445693
0.47275	-0.7199107	-0.7199107	-0.7199107	-0.7199628
0.49692	-2.3735831	-2.3735831	-2.3735831	-2.3737326

Table 1

α/σ FOR FLAT PLATE				
ℓ	Analytical	Numerical		
		K = 20	K = 10	K = 5
0.1	0.0395011	0.0395011	0.0395011	0.0395011
0.3	0.0679238	0.0679238	0.0679238	0.0679238
0.5	0.0857864	0.0857864	0.0857864	0.0857862
0.7	0.0956519	0.0956519	0.0956519	0.0956511
0.9	0.0865823	0.0865823	0.0865823	0.0866735

Table 2

CAVITY VOLUME V FOR FLAT PLATE AT $\alpha = 1$ RAD				
ℓ	Analytical	Numerical		
		K = 20	K = 10	K = 5
0.1	0.0313815	0.0313815	0.0313815	0.0313815
0.3	0.1676164	0.1676163	0.1676164	0.1676189
0.5	0.3758550	0.3758550	0.3758549	0.3758483
0.7	0.6699281	0.6699281	0.6699281	0.6690742
0.9	1.2007285	1.2007285	1.2007252	1.2203253

now observe that for the same flow conditions the linear theory
overpredicts the extent and the volume of the cavity for a NACA 16-006
hydrofoil.

increase the thickness and keep the same flow conditions, the cavity becomes longer and has more volume. This is the reverse from what we concluded for biconvex hydrofoils and is due to the change of camber for a planoconvex hydrofoil as we increase its thickness. It also is the reverse from what we observe in the experiments [26, 29, and 37].

Some cavity plots for a biconvex and a planoconvex hydrofoil and for each of the elementary problems as described in Section 3 can be seen in Figures 10 and 11. We observe that the thickness and camber problems are physically unacceptable, since they result in negative cavities or even negative cavitation numbers. Nevertheless, those problems, combined with some angle of attack, give meaningful solutions to our problem.

10. Comparison of the linear to the nonlinear theory

The linear theory described in the previous sections is compared with the nonlinear theory using the modified Riabouchinsky cavity termination model.

First, for a flat plate, our results and the nonlinear results obtained by using the analysis described in [33] are shown in Figures 12 and 13 for $\alpha = 2^\circ$ and $\alpha = 5^\circ$ respectively. We can anticipate that for the same flow conditions the linear theory underpredicts the extent and the volume of the cavity for a partially cavitating flat plate. We also observe that the discrepancies between linear and nonlinear theory become smaller as we decrease the angle of attack.

The cavity plots obtained from linear and nonlinear theory [38] for a NACA 16-006 thickness form at $\alpha = 4^\circ$ are shown in Figure 14. We

$$h_{N+1} = 0$$

(8.8)

The numerical integrations are performed for a flat plate and a parabolic camber, and the results are compared with the analytical ones described in Section 7. The agreement is excellent, even for a small number of Simpson's intervals K and for the whole range of cavity lengths as shown in Tables 1, 2, 3, 5, and 6. The cavity thickness distribution for a flat plate cavitating at $\lambda = 0.5$ is computed by using the algorithm described by the expressions (8.5), (8.6) and (8.7). The results are shown in Table 4 for a different number of points N , where $K = 50$ has been used for the evaluation of the cavity source distribution $q(x)$. The results seem to be quite insensitive to N , since a four-decimal-places accuracy is obtained rather quickly.

9. The biconvex and the planococonvex hydrofoils

The numerical computations as described in the previous section are carried out for a biconvex and a planococonvex hydrofoil. In Figures 7, 8, and 9, graphs of the results are shown for 4% and 8% maximum thickness/chord ratios. From those graphs the following conclusions can be drawn:

- a) A biconvex hydrofoil seems to simulate a flat plate better than a planococonvex hydrofoil with the same thickness, even though the last two have the same lower surfaces.
- b) For biconvex hydrofoils and short cavities, if we increase the thickness and keep the same flow conditions, the cavity becomes shorter and has less volume.
- c) For planococonvex hydrofoils and short cavities, if we

is singular and needs more careful numerical treatment. Instead, by using (A.19) we put (5.1) in the form:

$$q(z) = -\frac{1}{\pi} \cdot \frac{1+z^2}{\sqrt{z(s-z)}} \cdot \int_0^s \frac{\sqrt{n(s-n)}}{1+n^2} \cdot \frac{u_w^+(z) - u_w^+(n)}{z-n} \cdot dn + \\ + [\sigma U_\infty - 2 \cdot u_w^+(z)] \cdot \frac{A-Bz}{\sqrt{z(s-z)}} \quad (8.3)$$

The integral in (8.3) is not singular since $\frac{u_w^+(z) - u_w^+(n)}{z-n} \sim \left. \frac{du_w^+(n)}{dn} \right|_{n=z}$ as $n \rightarrow z$ and therefore it is evaluated by applying Simpson's rule in θ .

To find the cavity thickness distribution we perform the integration in (6.1) numerically after making the transformation:

$$\xi = l \cdot \sin^2(\frac{\phi}{2}) \\ 0 \leq \xi \leq l \leftrightarrow 0 \leq \phi \leq \pi \quad (8.4)$$

We then compute the discretized thickness distribution by using the algorithm:

$$h_{i+1} = h_i + \frac{l}{2 \cdot U_\infty} \cdot \int_{\phi_i}^{\phi_{i+1}} q(\xi) \cdot \sin \phi \cdot d\phi; \quad i = 1, N \quad (8.5)$$

with: $h_1 = 0 \text{ at } \phi_1 = 0 \quad (8.6)$

where: $\phi_{i+1} = \phi_i + \frac{\pi}{N}; \quad i = 1, N \quad (8.7)$

The integral in (8.5) is computed numerically by applying Simpson's rule with one interval (i.e. three points). A check to the numerical integrations should be the closure condition:

$$u_w^+(x) = \epsilon \cdot U_\infty; \quad 0 < x < 1 \quad (7.22)$$

Therefore the partially cavitating problem is identical to the non-cavitating one, once we put:

$$\sigma = 2 \cdot \epsilon \quad (7.23)$$

Again that results to zero cavity thickness!

8. Numerical method

For general shape hydrofoils, $u_w^+(x)$ can be evaluated either analytically or numerically. Then the integrals involved in the formulas (5.8), (5.1) and (6.5) will be evaluated numerically.

We first define the transformation variable θ as follows:

$$\eta = s \cdot \sin^2\left(\frac{\theta}{2}\right) \quad (8.1)$$

$0 \leq \eta \leq s \leftrightarrow 0 \leq \theta \leq \pi$

Then we perform the numerical integrations in terms of θ , by applying Simpson's rule with K uniform intervals (i.e., $2K+1$ points).

For example equation (5.8) becomes:

$$\sigma = \frac{\sqrt{2}}{\pi} \cdot \frac{s^2 \cdot r^2}{r^2 - 1} \cdot \int_0^\pi \left(\frac{u_w^+}{U_\infty} \right) \cdot \frac{\sin^2 \theta}{(1 + s^2 \cdot \sin^4 \frac{\theta}{2})^2} \cdot [\sqrt{r^2 + 1} - s \cdot \sin^2 \frac{\theta}{2} \cdot \sqrt{r^2 - 1}] \cdot d\theta \quad (8.2)$$

$$[\sqrt{r^2 + 1} - s \cdot \sin^2 \frac{\theta}{2} \cdot \sqrt{r^2 - 1}] \cdot d\theta$$

The integrand in (8.2) behaves smoothly at $\theta=0$ and $\theta=\pi$ and therefore we expect more accurate results by applying Simpson's rule in (8.2) than in (5.8) in which the integrand behaves like square root of the distance from the ends. Furthermore for the case u_w^+ behaves like $1/n$ at $n=0$ (as in (7.3)) then by using (8.2) we avoid the square root singularity at $n=0$ in the integrand of (5.8). The integral in (5.1)

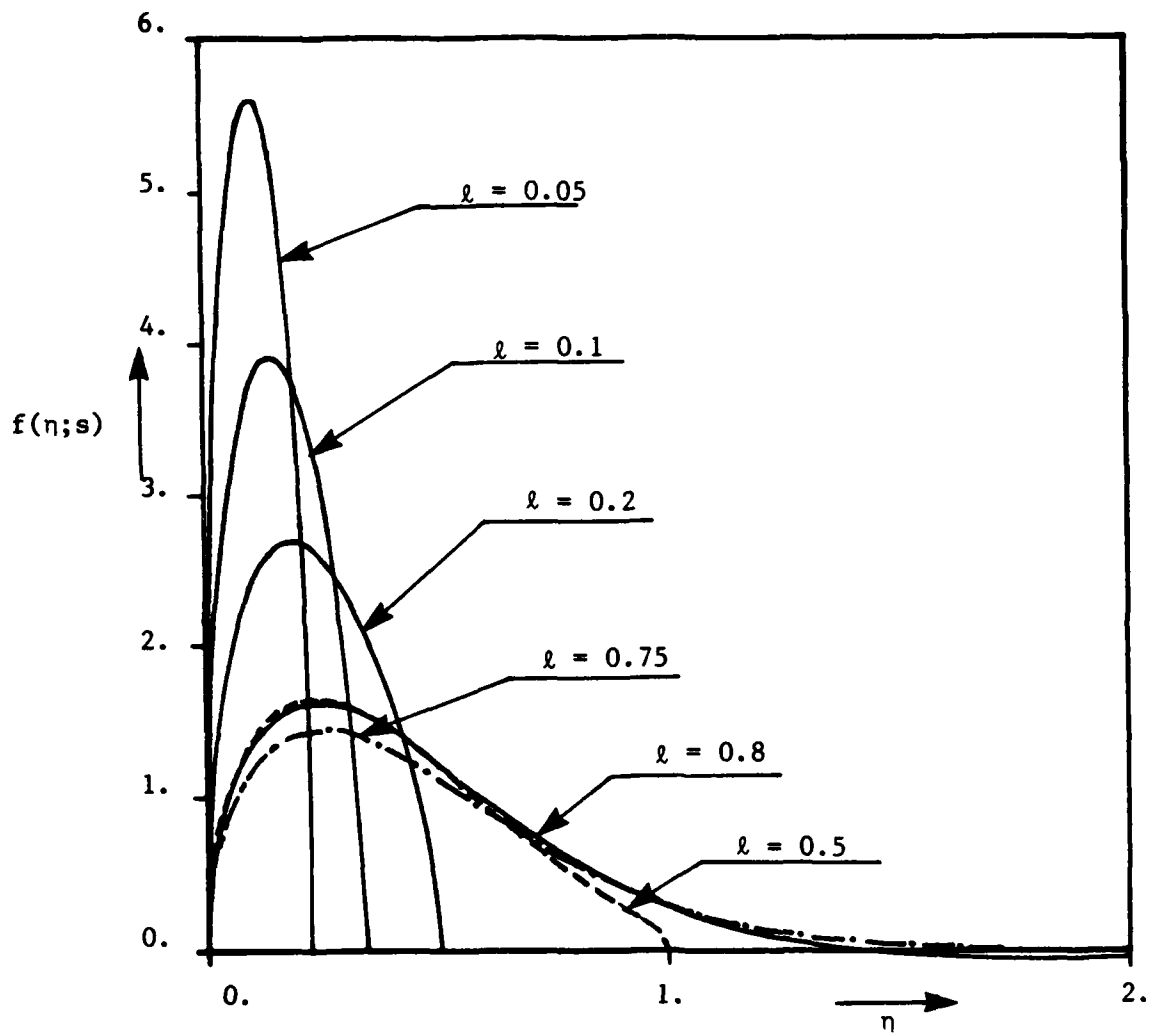
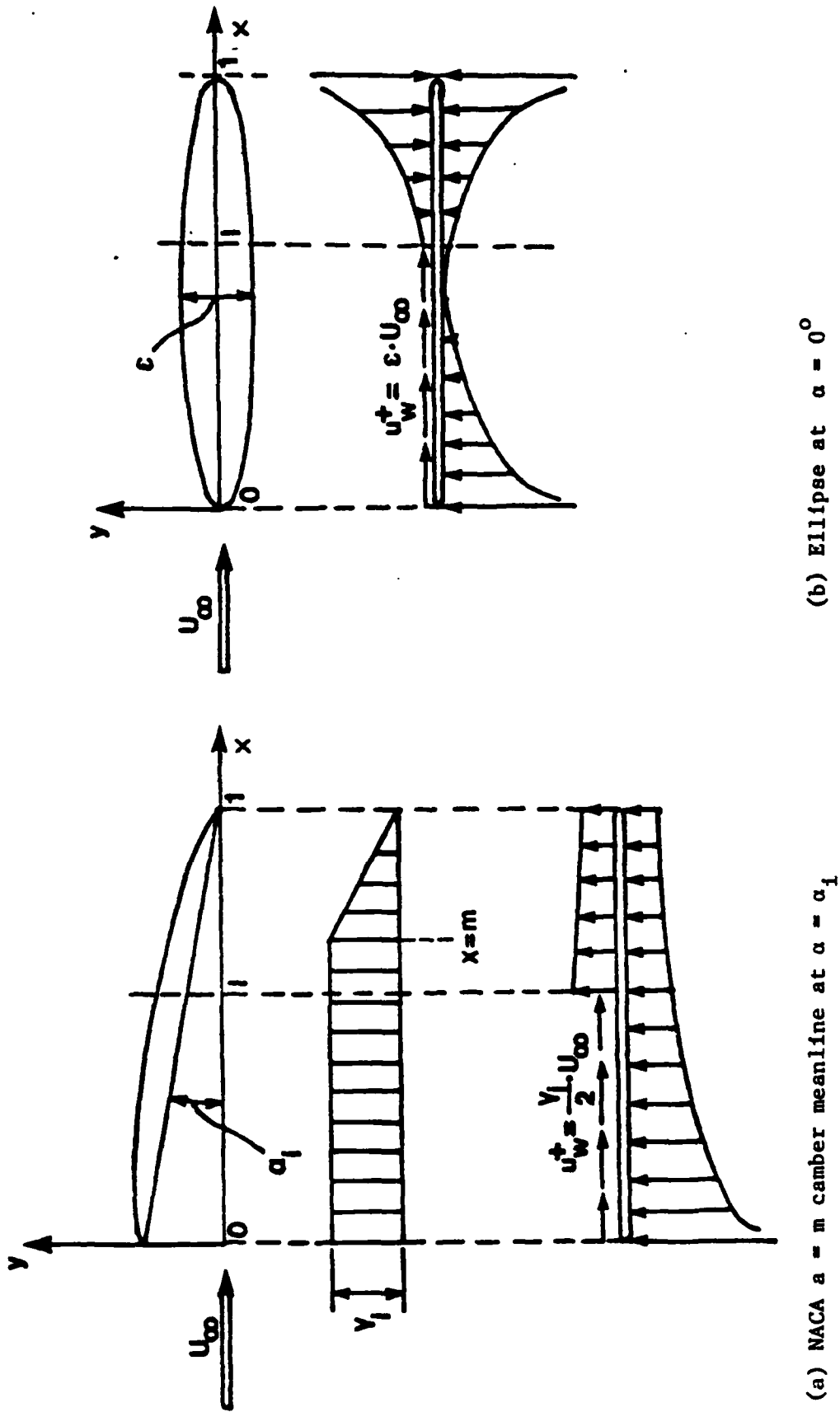


Figure 6. Graph of function $f(\eta; s)$ for different values of λ .



(a) NACA $a = m$ camber meanline at $\alpha = \alpha_l$

(b) Ellipse at $\alpha = 0^\circ$

Figure 5. Degenerate cases of partially cavitating hydrofoils

as:

$$\gamma_w(x) = \gamma_1; 0 < x < m$$

$$\gamma_w(x) = \gamma_1 \frac{1-x}{1-m}; m < x < 1$$
(7.16)

and:

$$u_w^+(x) = \frac{\gamma_1}{2} \cdot U_\infty; 0 < x < m$$

$$u_w^+(x) = \frac{\gamma_1}{2} \cdot U_\infty \cdot \left(\frac{1-x}{1-m}\right); m < x < 1$$
(7.17)

For $i < m$ the non-cavitating boundary value problem, as we can see in Figure 5a, already satisfies the partially cavitating problem stated by the equations (2.21), (2.26), (2.23) and (2.25), if we put:

$$\sigma = \gamma_1 \quad (7.18)$$

The respective unique solution will be:

$$q(x) = 0 \quad (7.19)$$

$$\gamma(x) = 0 \quad (7.20)$$

In other words there is no cavity for $i < m$!

The above results can also be obtained by substituting (7.17) in (5.8), (5.1) and (4.1). The equation (5.8) in combination with (7.17) and (7.18) requires the function $f(\eta, s)$ to satisfy the restriction:

$$\int_0^s f(\eta; s) \cdot d\eta = 1 \quad (7.21)$$

which also can be proved from direct integration. In other words, the function $f(\eta; s)$ becomes a "delta" function as $i \rightarrow 0$, as can also be seen in Figure 6.

f. Ellipse at $\alpha=0$ degrees

Consider an ellipse of axes $(1, \epsilon)$ subject to a uniform flow U_∞ , as shown at figure 5b. Then according to linear theory [39]:

$$\sigma = 2\lambda \cdot \sqrt{\ell} \cdot (1 + \sqrt{1-\ell}) \quad (7.11)$$

$$v = - \frac{\pi}{16} \cdot \lambda \cdot \ell^{3/2} \cdot (1 - \sqrt{1-\ell}) \cdot (3 - 2\ell) \quad (7.12)$$

c. Biconvex hydrofoil

This is a symmetric hydrofoil confined between two circular arcs.

The thickness distribution to first order is given as:

$$\tau(x) = 4\mu x(1-x) \quad (7.13)$$

By inserting (7.13) in (1.6) and (7.1) we get:

$$u_w^+(x) = \frac{2\mu U_\infty}{\pi} \cdot [2 + (1-2x) \cdot \ln(\frac{x}{1-x})]; \quad 0 < x < 1 \quad (7.14)$$

or in terms of the transformed variable η

$$u_w^+(\eta) = \frac{4\mu U_\infty}{\pi} \cdot (1 + \frac{1-\eta}{1+\eta}^2 \cdot \ln(\eta)); \quad 0 < \eta < s \quad (7.15)$$

The integrals involved in the expressions (5.8) and (6.5) are computed numerically as described in Section 8.

d. Planoconvex hydrofoil

This is the hydrofoil with the upper side a circular arc and the lower side flat. It can be considered as a combination of a parabolic camber and a biconvex hydrofoil with $\mu = \lambda$ as illustrated in Figure 4. Therefore the results will be the superposition of the two previous cases, according to Section 3.

e. NACA $a=m$ camber meanlines

The vortex distribution at ideal angle $\alpha = \alpha_i$ will be given

$$\sigma = 2 \cdot \alpha \cdot s \cdot \frac{r^2 + 1}{r^2 - 1} \quad (7.4)$$

$$q(z) = \sigma \cdot U_\infty \cdot \frac{(M - N \cdot z)}{\sqrt{z \cdot (s - z)}}; \quad 0 < z < s \quad (7.5)$$

$$M = \frac{1}{\sqrt{2}} \left[\frac{\alpha}{\sigma} \cdot (r^2 + 1)^{\frac{1}{2}} + \frac{1}{2} (r^2 - 1)^{\frac{1}{2}} \right] \quad (7.6a)$$

$$N = \frac{1}{\sqrt{2}} \left[\frac{1}{2} \cdot (r^2 + 1)^{\frac{1}{2}} - \frac{\alpha}{\sigma} (r^2 - 1)^{\frac{1}{2}} \right] \quad (7.6b)$$

By using (6.5) and (7.3) we also recover after lengthy algebra the result by Geurst for the cavity volume V [10]:

$$V = \frac{\pi \cdot \alpha \cdot s}{16} \cdot l (1 + 4 \cdot \sqrt{1 - l}) \quad (7.7)$$

b. Parabolic camber

In that case the camber distribution is given as:

$$\bar{\eta}(x) = 2 \cdot \lambda \cdot x \cdot (1 - x); \quad 0 \leq x \leq 1 \quad (7.8)$$

Substituting (7.8) in (1.3) we get:

$$\gamma_w(x) = 8 \cdot U_\infty \cdot \lambda \cdot \sqrt{x(1-x)}; \quad 0 \leq x \leq 1 \quad (7.9)$$

and thus:

$$u_w^+(n) = 4 \cdot U_\infty \cdot \lambda \cdot \frac{n}{1+n^2}; \quad 0 \leq n \leq s \quad (7.10)$$

Then the formulas (5.8) and (6.5) will recover the results by Geurst for $\alpha = 0$ degrees [12]:

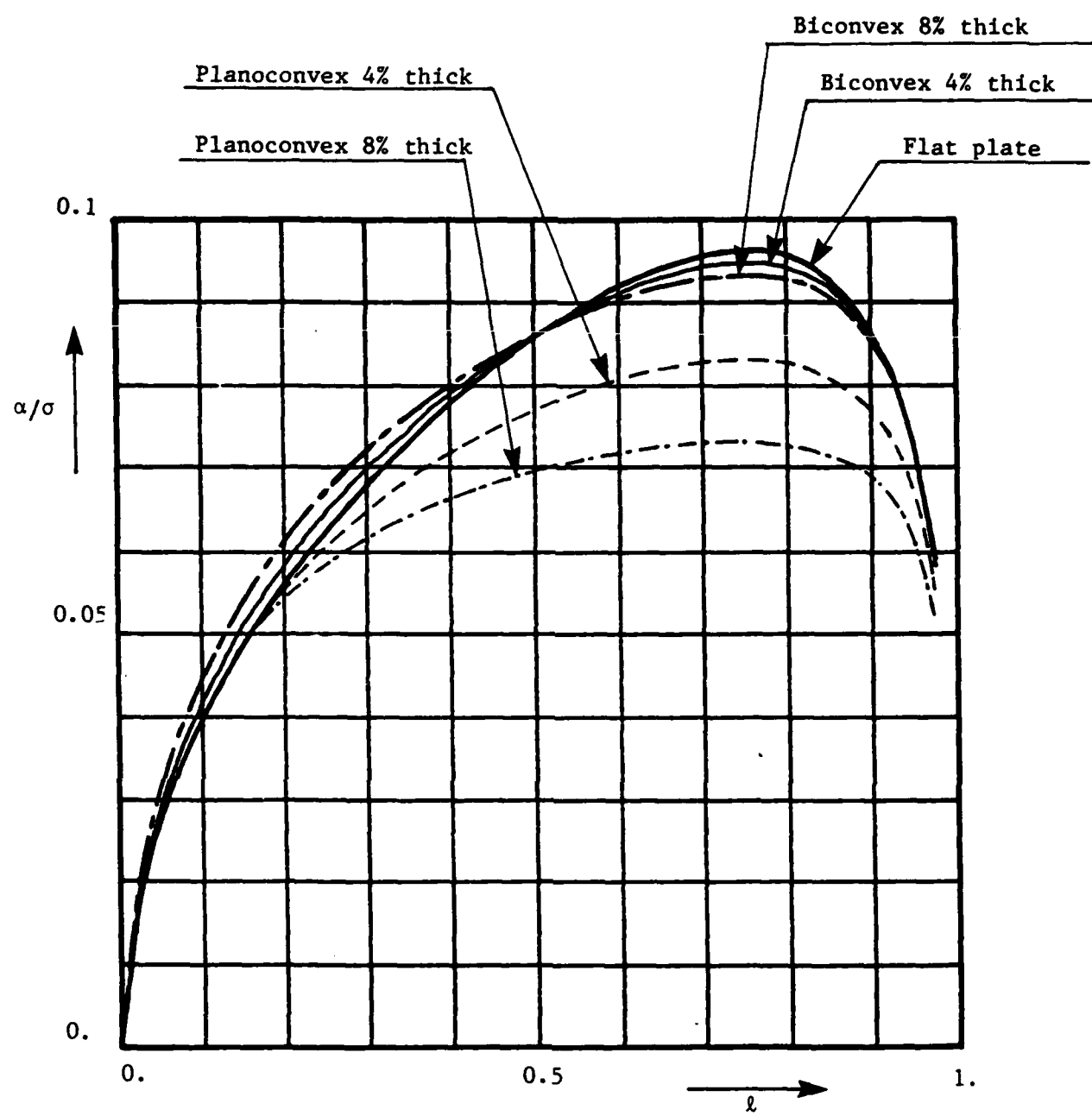


Figure 7. α/σ vs. l for biconvex hydrofoils, planoconvex hydrofoils, and a flat plate, all at $\alpha = 4^\circ$ - Linear theory

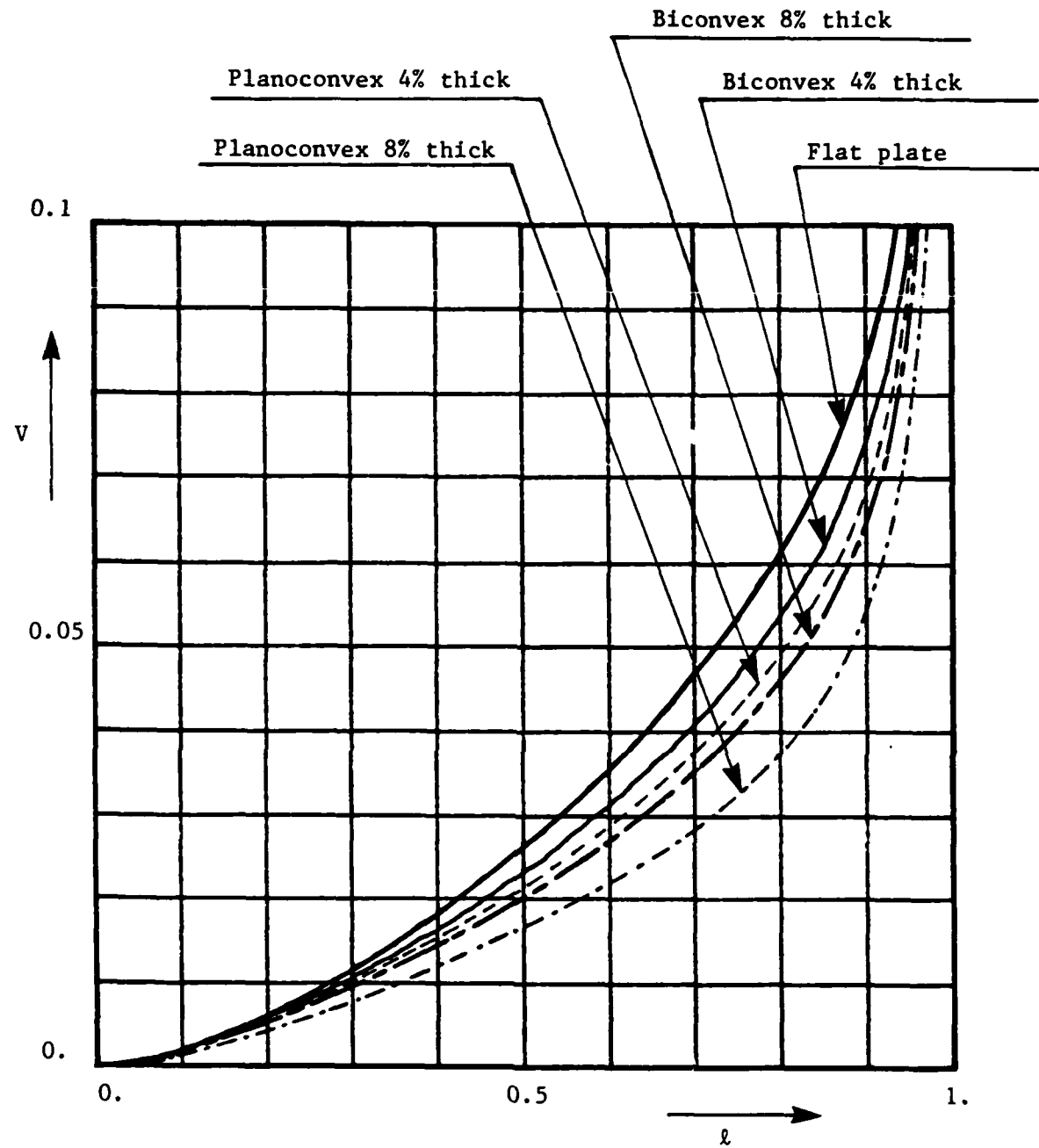


Figure 8. V vs. l for biconvex hydrofoils, planoconvex hydrofoils, and a flat plate, all at $\alpha = 4^\circ$ - Linear theory

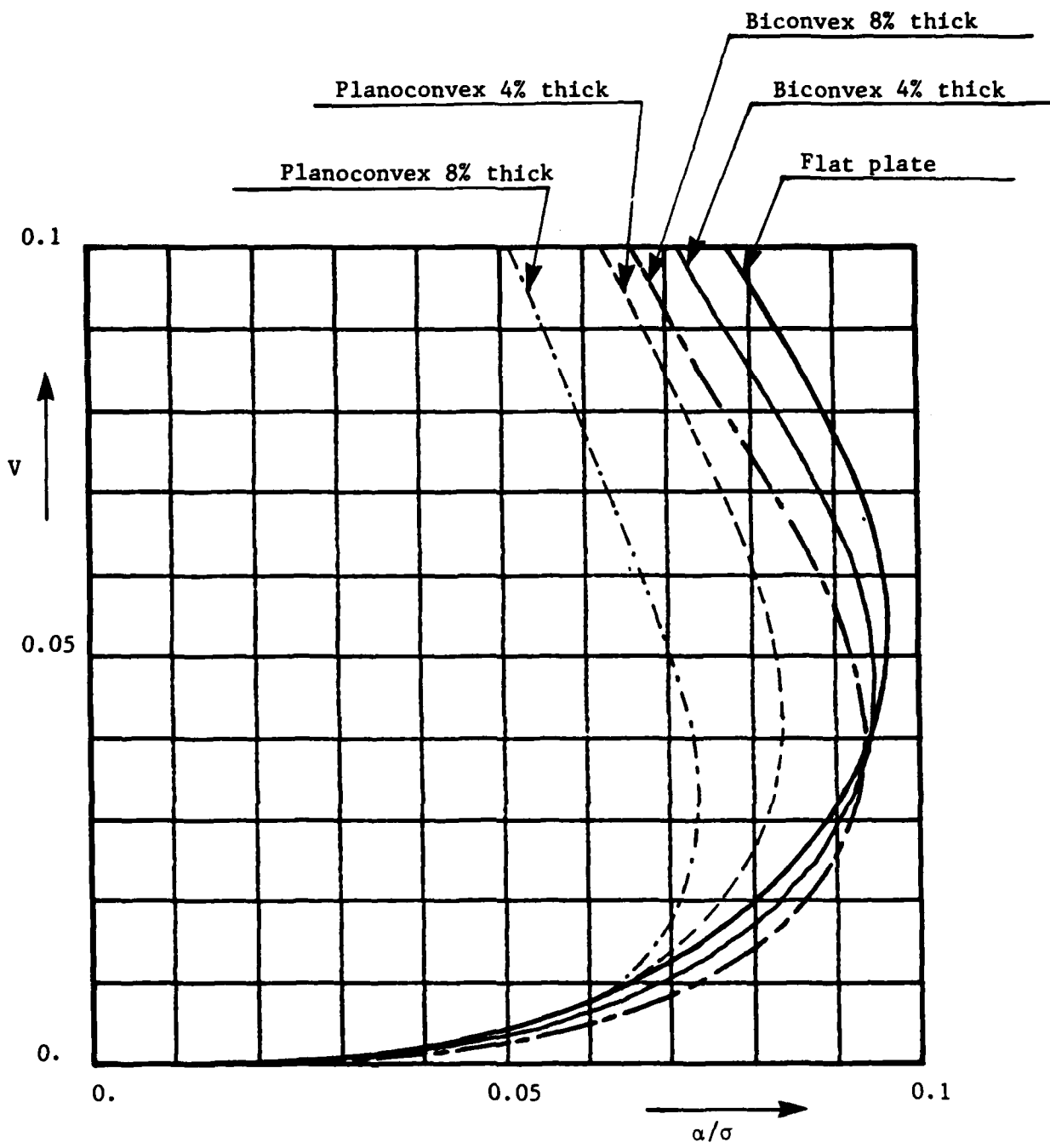
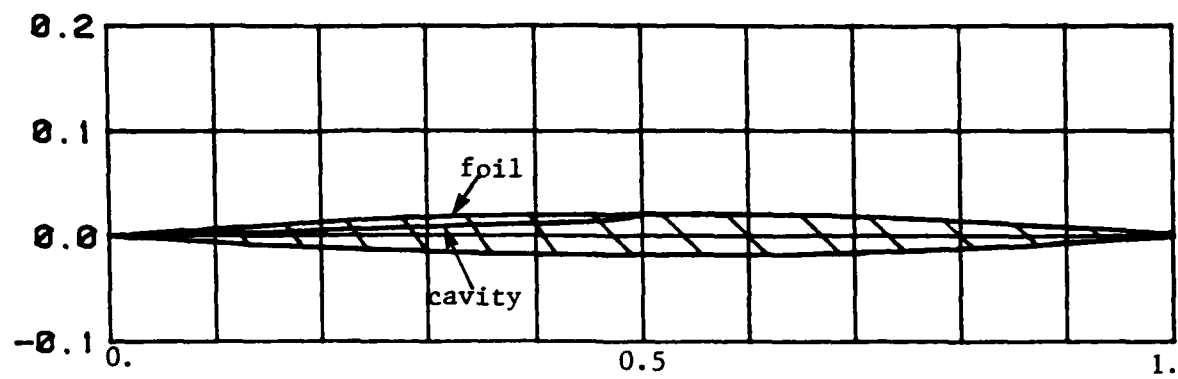
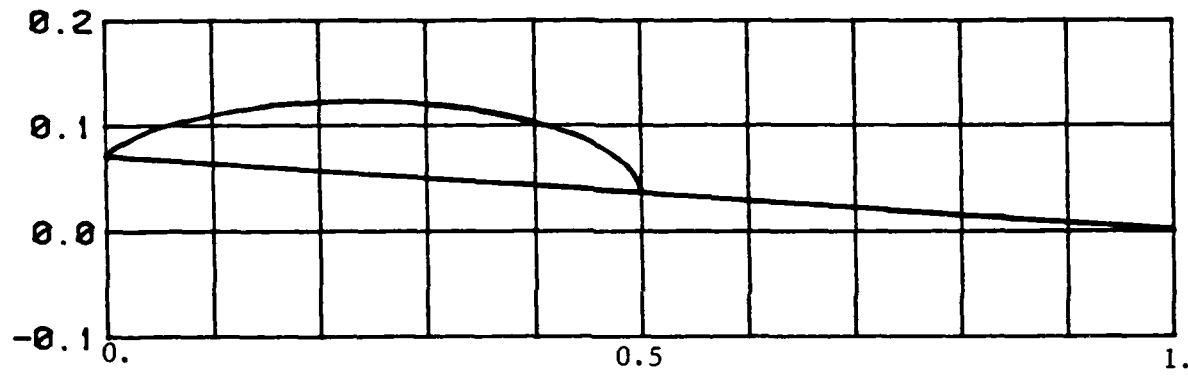


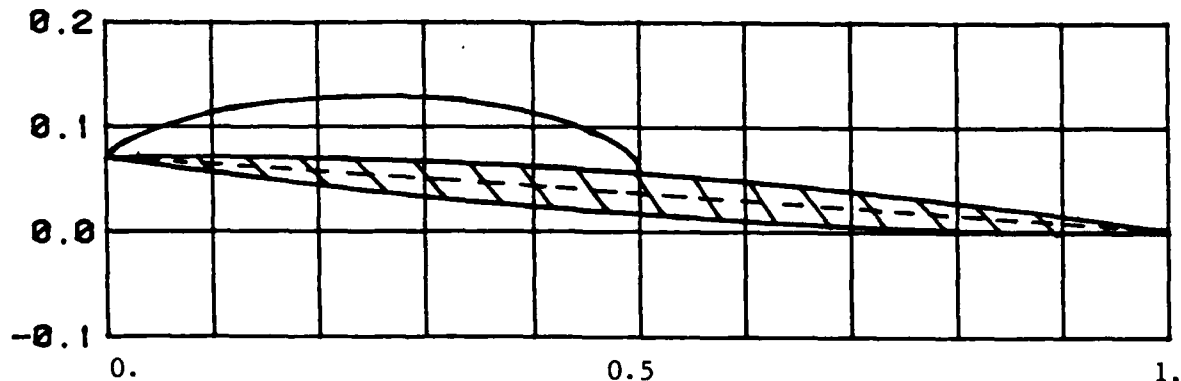
Figure 9. V vs. α/σ for biconvex hydrofoils, planoconvex hydrofoils, and a flat plate, all at $\alpha = 4^\circ$ - Linear theory



(a) Biconvex hydrofoil at $\alpha = 0^\circ$, $\sigma = -0.0013$

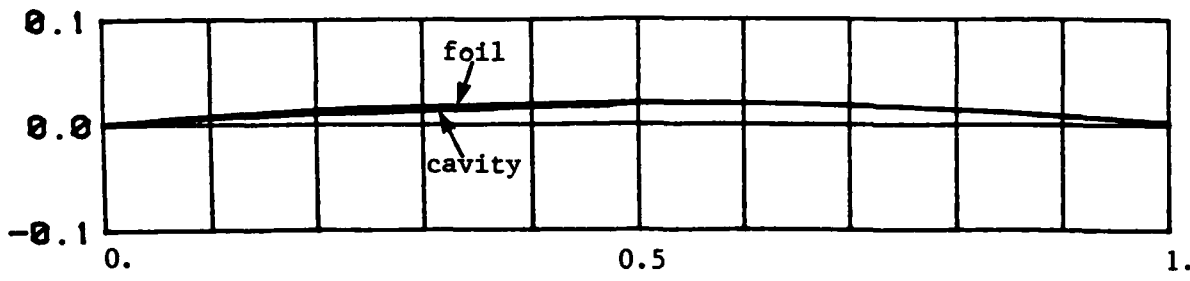


(b) Flat plate at $\alpha = 4^\circ$, $\sigma = 0.8138$

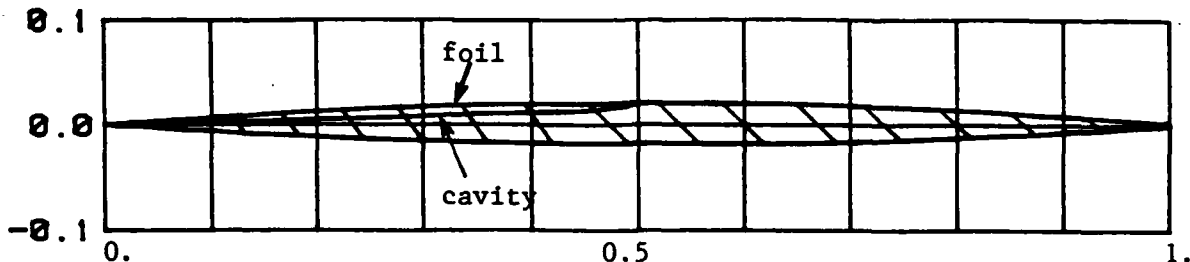


(c) Biconvex hydrofoil at $\alpha = 4^\circ$, $\sigma = 0.8125$

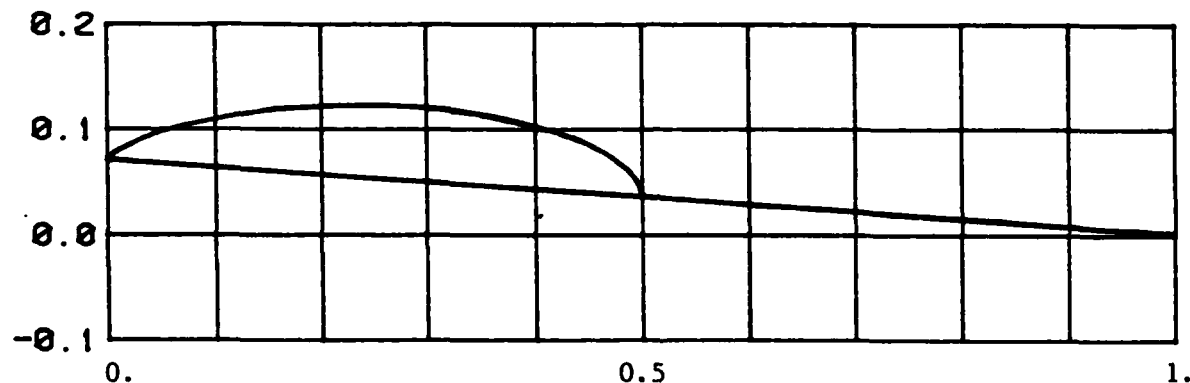
Figure 10. The elementary problems for partially cavitating 4% thick biconvex hydrofoil at $\ell = 0.5$. (a) + (b) = (c)



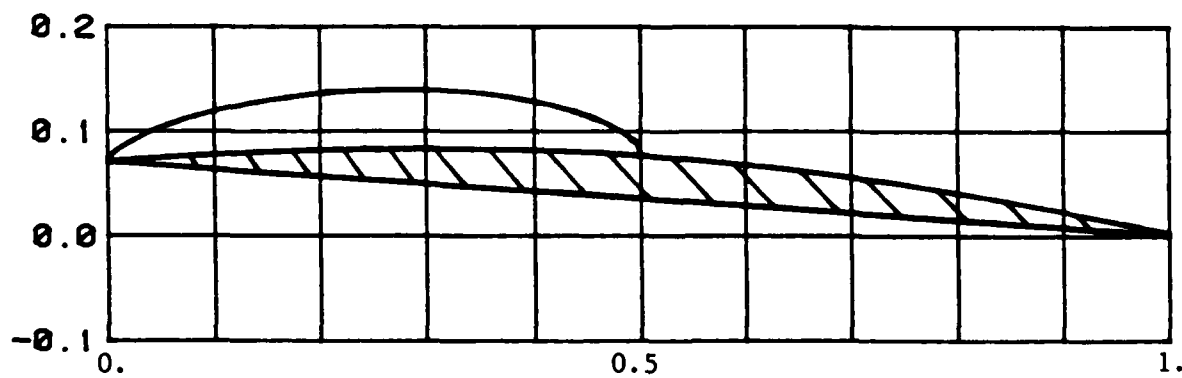
(a) Parabolic camber at $\alpha = 0^\circ$, $\sigma = 0.0966$



(b) Biconvex hydrofoil at $\alpha = 0^\circ$, $\sigma = -0.0013$



(c) Flat plate at $\alpha = 4^\circ$, $\sigma = 0.8138$



(d) Planoconvex hydrofoil at $\alpha = 4^\circ$, $\sigma = 0.9091$

Figure 11. The elementary problems for partially cavitating 4% thick
planoconvex hydrofoil at $\ell = 0.5$ (a) + (b) + (c) = (d)

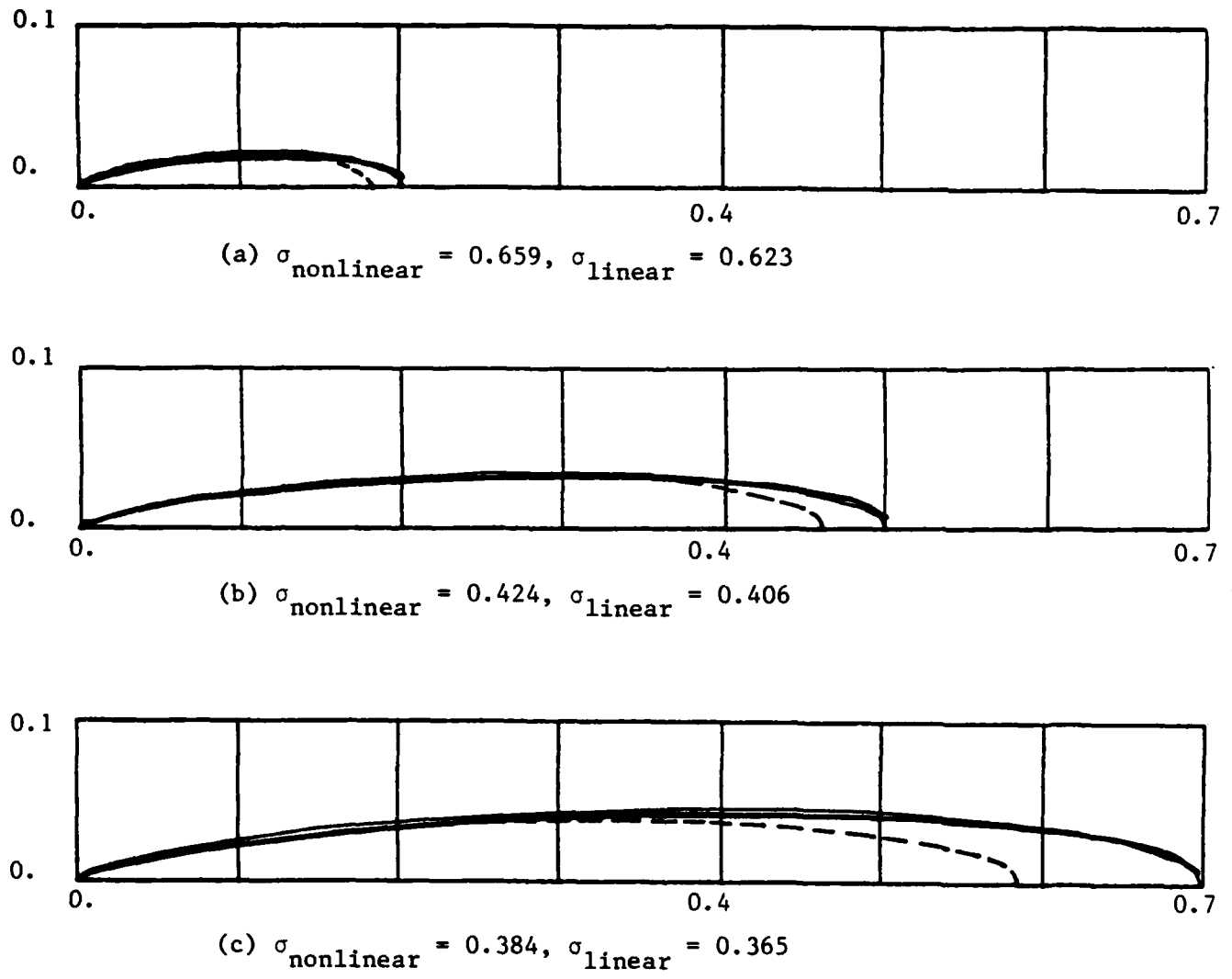
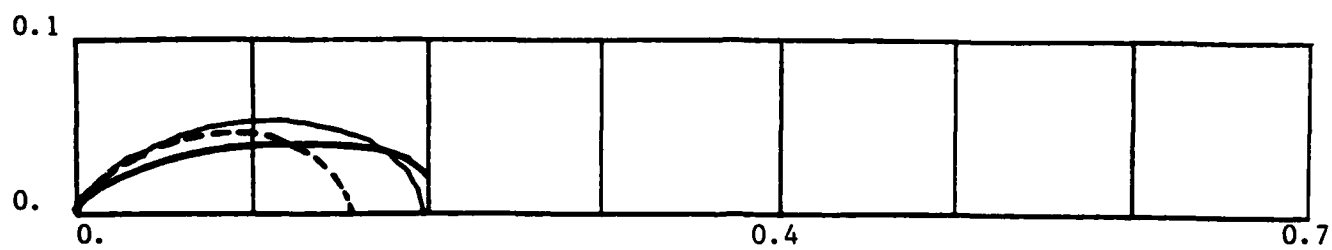
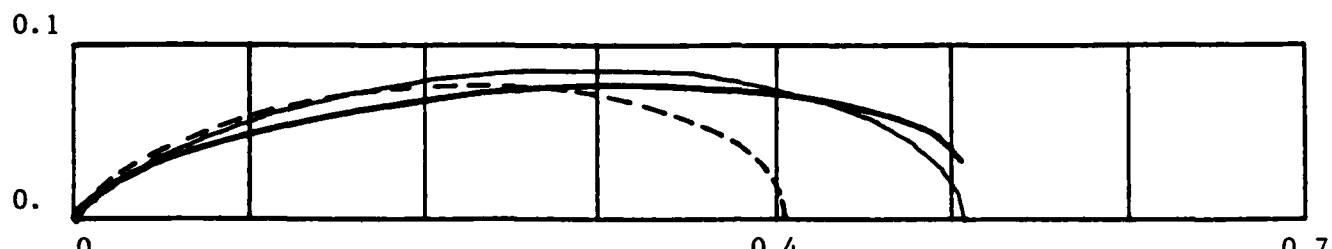


Figure 12. Partially cavitating flat plate at $\alpha = 2^\circ$

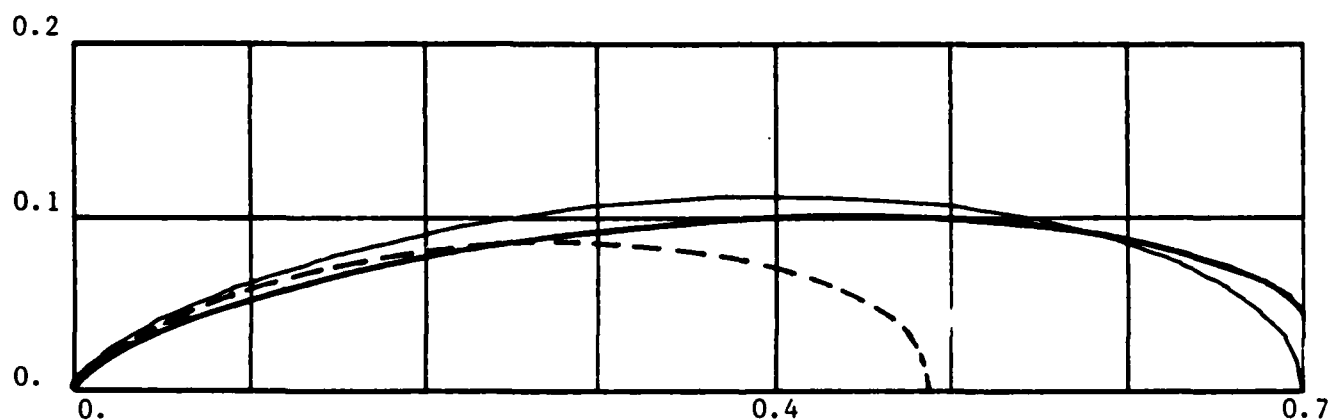
- nonlinear theory [33]
- linear theory for the same cavity length as nonlinear theory
- linear theory for the same cavitation number as nonlinear theory



(a) $\sigma_{\text{nonlinear}} = 1.791, \sigma_{\text{linear}} = 1.575$



(b) $\sigma_{\text{nonlinear}} = 1.114, \sigma_{\text{linear}} = 1.012$



(c) $\sigma_{\text{nonlinear}} = 1.028, \sigma_{\text{linear}} = 0.912$

Figure 13. Partially cavitating flat plate at $\alpha = 5^\circ$

- nonlinear theory [33]
- linear theory for the same cavity length as nonlinear theory
- - - linear theory for the same cavitation number as nonlinear theory

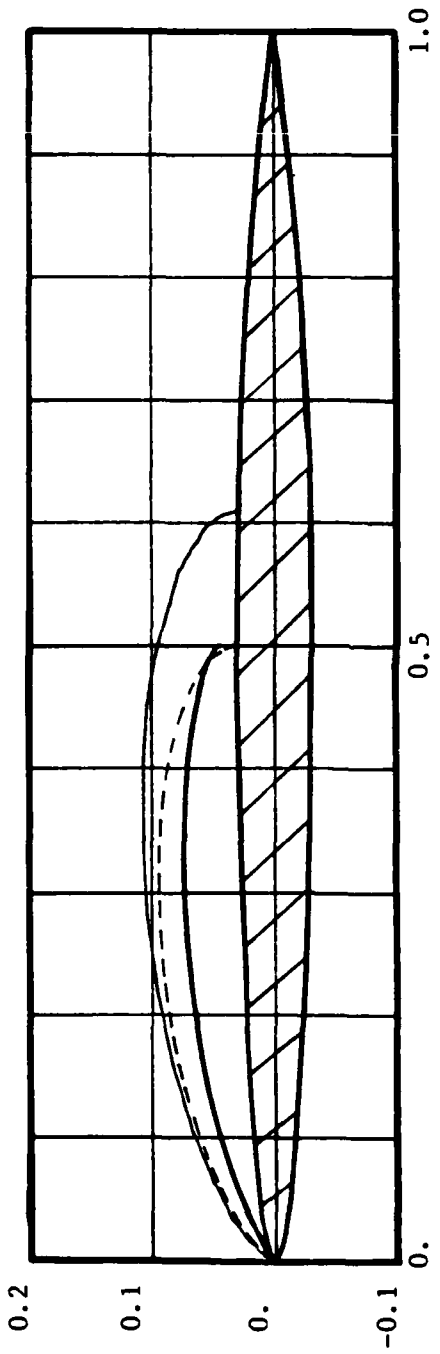


Figure 14. Cavity plots for NACA 16-006 thickness form at $\alpha = 4^\circ$

- nonlinear theory, [38] at $\lambda = 0.5$, $\sigma = 0.877$
- - - linear theory at $\lambda = 0.5$, $\sigma = 0.934$
- · - linear theory at $\lambda = 0.61$, $\sigma = 0.877$

PART B. SUPERCAVITATING HYDROFOIL--LINEAR THEORY

11. Formulation of the supercavitating hydrofoil problem

Consider now a supercavitating hydrofoil of chord-length $c = 1$ in uniform flow U_∞ and ambient pressure P_∞ as shown in Figure 15. Given the cavity length ℓ and the lower surface distribution $\bar{\eta}_\ell(x)$ of the hydrofoil, we want to determine the corresponding cavitation number σ and the shape of the cavity.

According to the linear theory, the perturbation velocity field (u_c, v_c) due to the cavity and the foil can be generated by a distribution of vortices $\gamma_c(x)$ and sources $q_c(x)$ along the slit from $x = 0$ to $x = \ell$.

The linearized boundary conditions, assuming that the cavity starts at the leading edge of the foil, will be:

The dynamic boundary conditions:

$$u_c = \frac{\sigma}{2} \cdot U_\infty \quad ; \quad 0 < x < \ell, y = 0^+ \quad (11.1)$$

$$u_c = \frac{\sigma}{2} \cdot U_\infty \quad ; \quad 1 < x < \ell, y = 0^- \quad (11.2)$$

The kinematic boundary condition:

$$v_c = U_\infty \cdot \frac{\partial \bar{\eta}_\ell}{\partial x} \quad ; \quad 0 < x < 1, y = 0^- \quad (11.3)$$

The Kutta condition:

$$(u_c, v_c) \text{ finite at } x = 1 \quad (11.4)$$

The closure condition:

The cavity closes at its trailing edge:

$$h(\ell) = 0 \quad (11.5)$$

The condition at infinity:

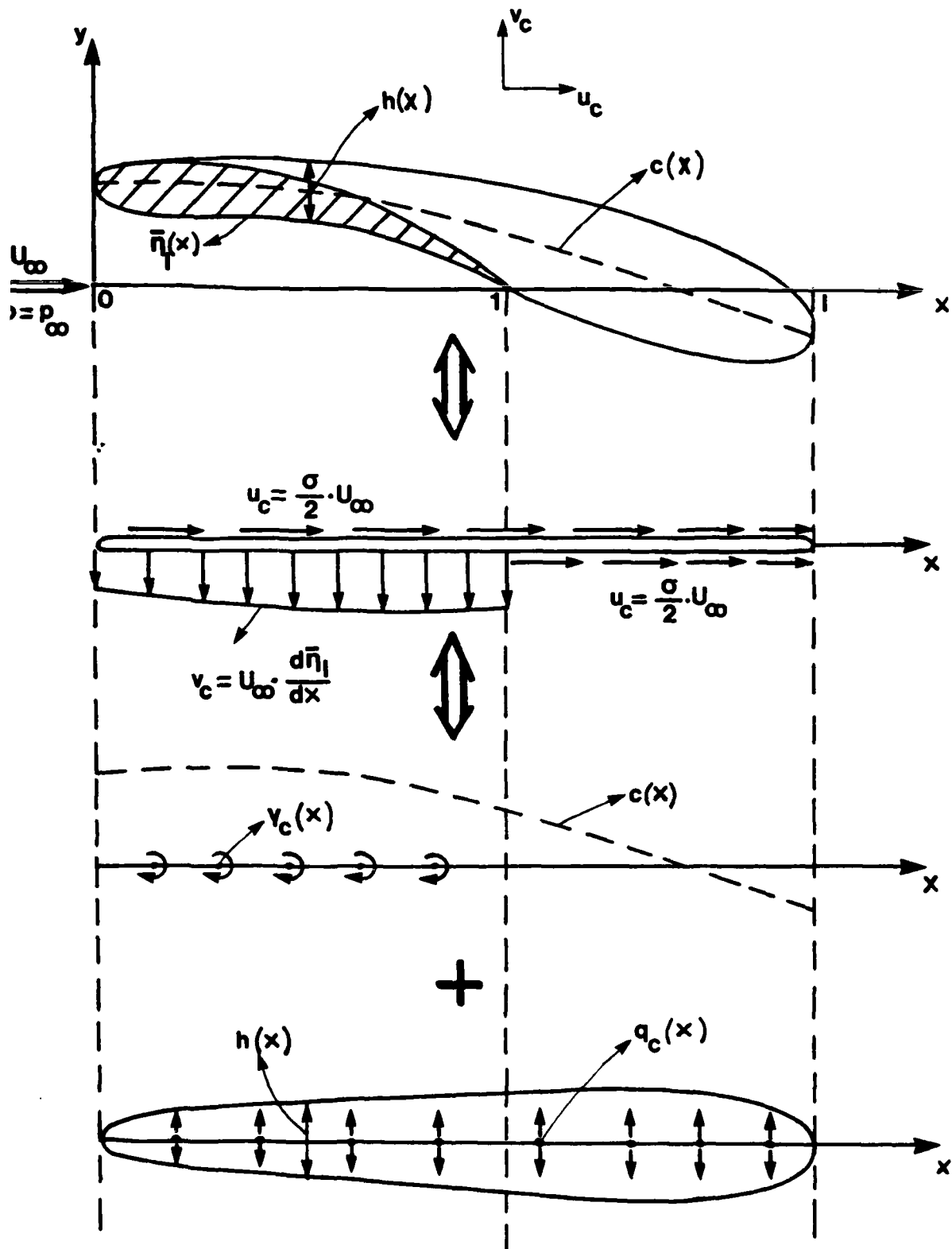


Figure 15. Supercavitating Hydrofoil in Linear Theory

$$u_c \rightarrow 0 \text{ and } v_c \rightarrow 0 \text{ at infinity}$$

(11.6)

The boundary conditions in terms of the unknown distributions

$\gamma_c(x)$ and $q_c(x)$ will become:

$$\frac{\gamma_c(x)}{2} - \frac{1}{2\pi} \cdot \int_0^l \frac{q_c(\xi) \cdot d\xi}{\xi - x} - \frac{\sigma}{2} \cdot U_\infty = 0 ; \quad 0 < x < l \quad (11.7)$$

$$\text{with } \gamma_c(x) = 0 \quad \text{for } 1 < x < l$$

$$-\frac{q_c(x)}{2} + \frac{1}{2\pi} \int_0^1 \frac{\gamma_c(\xi) \cdot d\xi}{\xi - x} = U_\infty \cdot \frac{\partial \bar{n}_l}{\partial x} ; \quad 0 < x < l \quad (11.8)$$

$$\gamma_c(1) = 0 \quad (11.9)$$

$$\int_0^l q_c(x) \cdot dx = 0 \quad (11.10)$$

$$\int_0^l q_c(x) \cdot dx = 0$$

The boundary condition (11.6) is automatically satisfied by the use of vortices and sources for the representation of the velocity field. For given l and $\bar{n}_l(x)$, the equations (11.7) - (11.10) give us the unique solution $\sigma, \gamma_c(x)$ and $q_c(x)$.

The cavity thickness $h(x)$ and the cavity camber $c(x)$ will then be given by the following relationships:

$$U_\infty \cdot \frac{\partial h}{\partial x} = q_c(x) ; \quad 0 < x < l \quad (11.11)$$

$$c(x) = \bar{n}_l(x) + \frac{h(x)}{2} ; \quad 0 < x < l \quad (11.12a)$$

$$U_\infty \cdot \frac{\partial c}{\partial x} = v_{in}(x) ; \quad 1 < x < l \quad (11.12b)$$

$$v_{in}(x) = -\frac{1}{2\pi} \cdot \int_0^1 \frac{\gamma_c(\xi) \cdot d\xi}{x - \xi} ; \quad 1 < x < l \quad (11.13)$$

where $v_{in}(x)$ is the induced velocity in the wake by the vorticity distribution $\gamma_c(x)$.

12. Decomposition in the supercavitating hydrofoil problem

If the hydrofoil has a camber meanline $\eta(x)$, a thickness distribution $\tau(x)$ and is at an angle of attack α , as shown in Figure 16, then its lower surface can be expressed as:

$$\bar{\eta}_\ell(x) = \eta(x) - \frac{\tau(x)}{2} + \alpha \cdot (1-x) \quad (12.1)$$

and

$$\frac{\partial \bar{\eta}_\ell}{\partial x} = \frac{\partial \eta}{\partial x} - \frac{1}{2} \cdot \frac{\partial \tau}{\partial x} - \alpha \quad (12.2)$$

By decomposing the RHS of the system of equations (11.7) - (11.10) as in (12.2), we can easily see that as long as we keep ℓ fixed, the supercavitating general shape hydrofoil problem can be considered as the superposition of the following three elementary problems (also illustrated in Figure 16):

The camber problem with $\bar{\eta}_\ell(x) = \eta(x)$

The thickness problem with $\bar{\eta}_\ell(x) = -\frac{\tau(x)}{2}$

The flat plate problem with $\bar{\eta}_\ell(x) = \alpha \cdot (1-x)$

The solution σ , $\gamma_c^c(x)$, $q_c^c(x)$ will be the linear superposition of the solutions to those problems:

$$\sigma = \sigma^c + \sigma^\tau + \sigma^\alpha \quad (12.3)$$

$$\gamma_c^c(x) = \gamma_c^c(x) + \gamma_c^\tau(x) + \gamma_c^\alpha(x) \quad (12.4)$$

$$q_c^c(x) = q_c^c(x) + q_c^\tau(x) + q_c^\alpha(x) \quad (12.5)$$

Furthermore, for each quantity Q_c which depends linearly on the

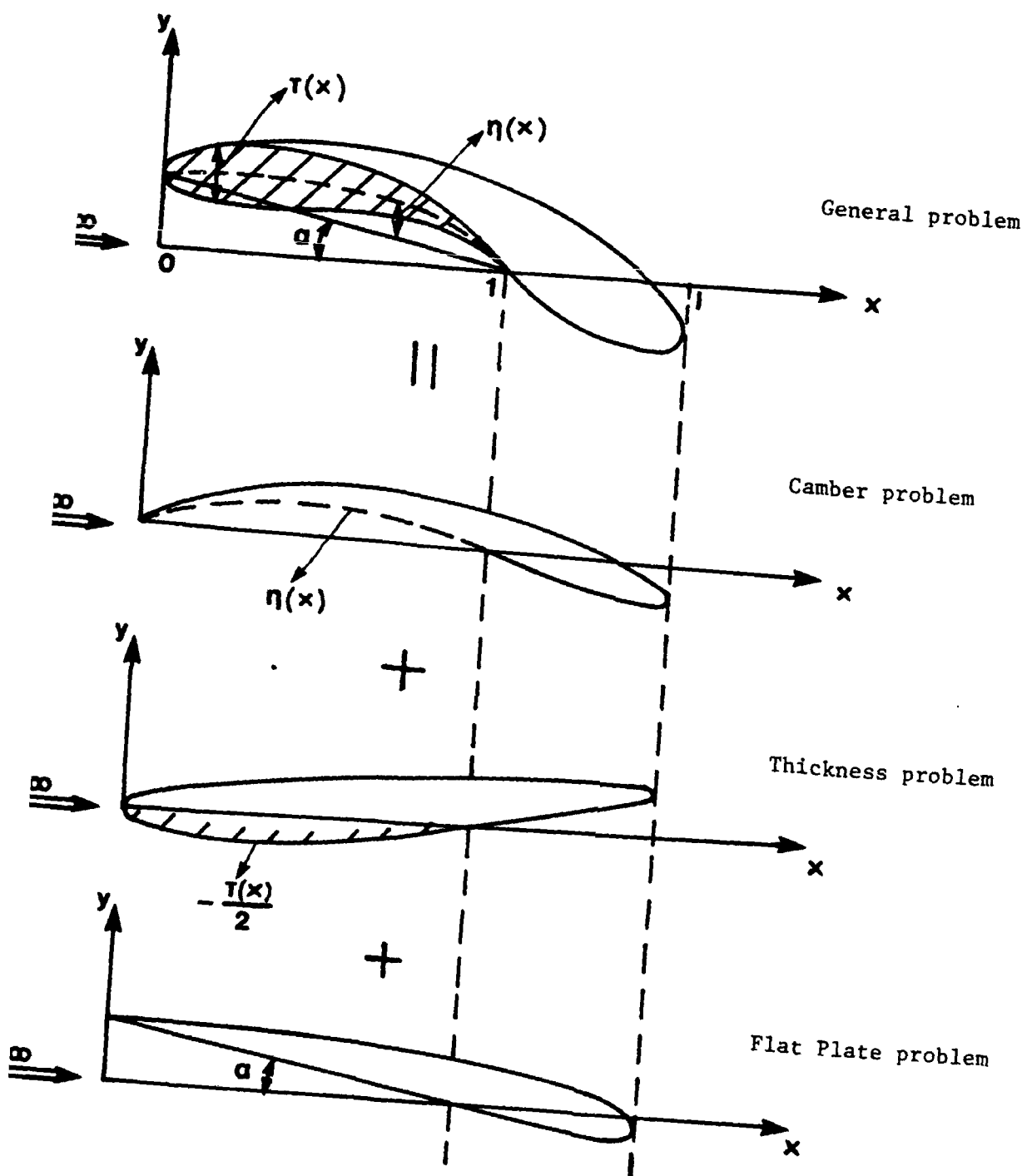


Figure 16. Decomposition of the Supercavitating Hydrofoil Problem

solution, we will have:

$$Q_c = Q_c^c + Q_c^\tau + Q_c^\alpha \quad (12.6)$$

For example, Q_c can be: σ , $\gamma_c(x)$, $q_c(x)$, $h(x)$, $c(x)$, V , C_L , C_D , $\sqrt{C_D}$. Some particular cases can then be examined:

Change in the angle of attack. If we change the angle of attack of a supercavitating hydrofoil by $\Delta\alpha$, then the solution for the same cavity length will change by an amount which is the solution to a supercavitating flat plate at angle of attack $\Delta\alpha$ and the same cavity length, as also illustrated in Figure 17a.

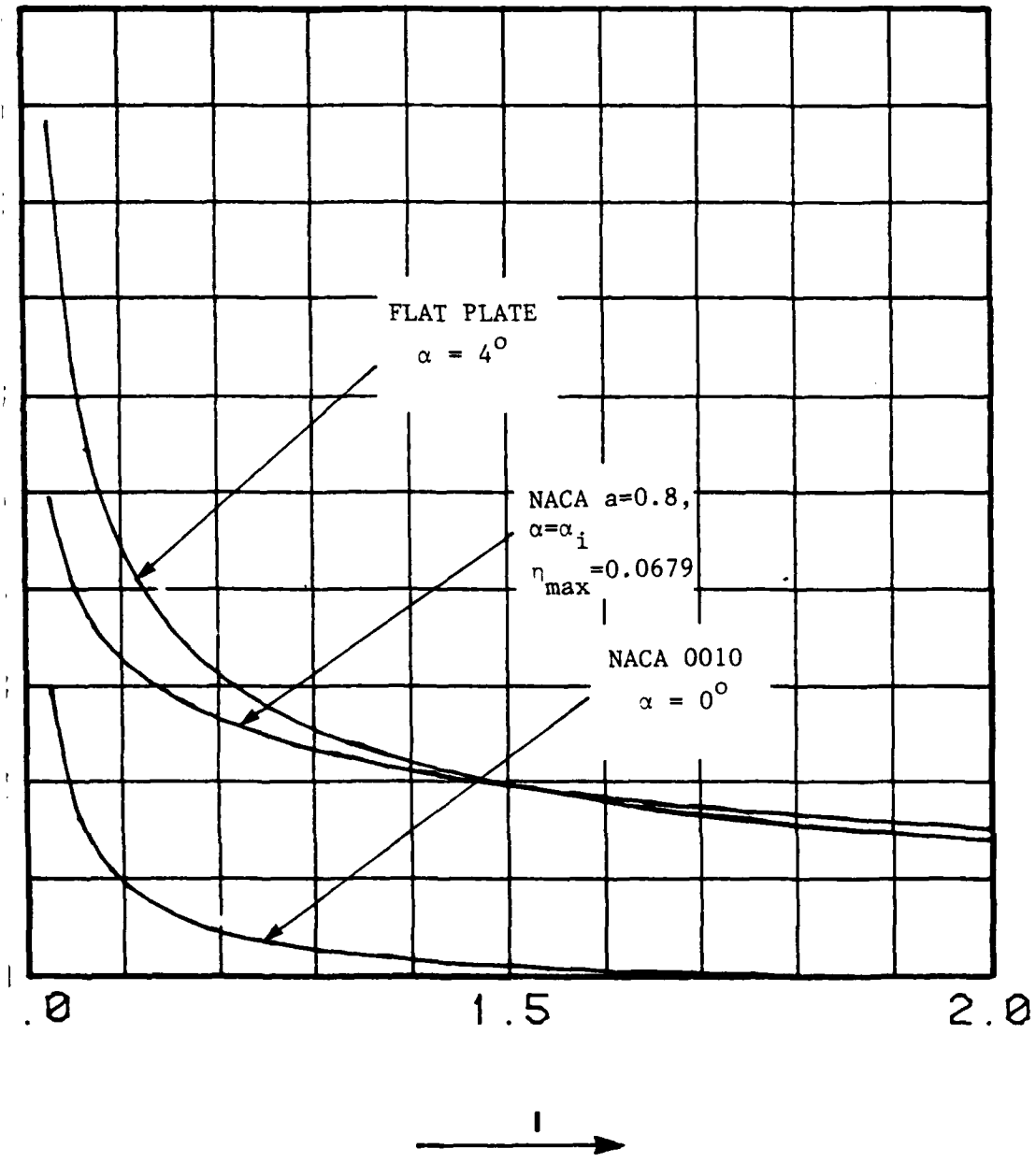
Change of the camber/chord ratio. For a given camber meanline shape supercavitating at zero angle of attack, if we change the camber/chord ratio by a factor, then the solution for the same cavity length changes by the same factor, as also illustrated in Figure 17b. A similar relationship is also true for affine thickness forms.

For a given camber or thickness series, therefore, we need to solve the problem for one value of the similarity parameter and one angle of attack.

The decomposition described above can also be done when the cavity starts after the leading edge of the foil. In that case, both the leading edge and the trailing edge of the cavity have to remain fixed for each elementary problem.

Solution to the general supercavitating hydrofoil problem

It is convenient to introduce the following nondimensional quantities:



19. σ vs. l for some Supercavitating Hydrofoils

Table 11

ELLIPTIC FOIL WITH $\epsilon = 1$ AT $\lambda = 2$.

CAVITY THICKNESS DISTRIBUTION $h(x)$

x	Analytical	Numerical	
		N = 10	N = 20
0.0000	0.000000	0.000000	0.000000
0.0489	0.618034	0.618036	0.618034
0.1910	1.175571	1.175574	1.175571
0.4122	1.618034	1.618039	1.618034
0.6910	1.902113	1.902119	1.902113
1.0000	2.000000	2.000007	2.000000
1.3090	1.902113	1.902119	1.902113
1.5878	1.618034	1.618039	1.618034
1.8090	1.175571	1.175574	1.175571
1.9510	0.618034	0.618036	0.618034
2.0000	0.000000	-0.000000	-0.000000

Table 9

ELLIPTIC FOIL WITH $\epsilon = 1$ AT $\ell = 2$		
	σ	V
Analytical	2.	3.14159265
$K = 20$	2.00000000	3.14159265
$K = 10$	2.00000000	3.14159265
$K = 5$	1.99999994	3.14159217
$K = 3$	1.99866994	3.13764913

Table 10

ELLIPTIC FOIL WITH $\epsilon = 1$ AT $\ell = 2$		CAVITY SOURCE DISTRIBUTION $\bar{q}(x)$		
x	Analytical	Numerical		
		$K = 20$	$K = 10$	$K = 3$
.1	2.06474	2.06474	2.06474	2.06206
.2	1.33333	1.33333	1.33333	1.33270
.4	0.75000	0.75000	0.75000	0.74987
.5	0.57735	0.57735	0.57735	0.57727
.7	0.31449	0.31449	0.31449	0.31444
.9	0.10050	0.10050	0.10050	0.10046
.	0.	0.00000	0.00000	-0.00005

Table 7

FLAT PLATE AT $\alpha = 1$ RAD, CAVITATION NUMBER σ

ℓ	Analytical	Numerical		
		K = 20	K = 10	K = 5
1.1	6.324555	6.324555	6.324560	6.329471
1.3	3.651484	3.651484	3.651484	3.651730
1.5	2.828427	2.828427	2.828427	2.828405
1.8	2.236068	2.236068	2.236068	2.236057
2.0	2.	2.000000	2.000000	1.999995

Table 8

FLAT PLATE AT $\alpha = 1$ RAD, CAVITY VOLUME V

ℓ	Analytical	Numerical		
		K = 20	K = 10	K = 5
1.1	1.272656	1.272656	1.272668	1.282604
1.3	1.327715	1.327715	1.327715	1.328218
1.5	1.554475	1.554475	1.554475	1.554295
1.8	1.975729	1.975729	1.975729	1.975635
2.0	2.288818	2.288818	2.288818	2.288768

= 0.0679.

σ^T, V^T : correspond to the NACA 0010 thickness form.

α_i : ideal angle of attack. In this case $a_i = 1.54 \times \frac{\eta_{\max}}{0.0679}$ degrees.

The cavity plots for the three elementary problems for a NACA $a = 0.8$ camber meanline combined with a NACA 0010 thickness form at $\alpha = 7^\circ$ are also shown in Figure 21. A more systematic exposure of cavity plots for different cavity lengths can be found in [22].

Finally, cavity shapes from linear and non-linear theory [38] for a flat plate at $\alpha = 4^\circ$ are compared in Figure 22. The differences are very small and this indicates that linear theory works quite well for supercavitating sharp-nosed hydrofoils.

square root singularities of the integrands at $\eta = 0$ and $\eta = t$. The numerical integrations are performed thereafter by applying Simpson's rule with K uniform intervals in θ .

The cavity thickness and camber distributions are computed also numerically by applying in equations (17.1) and (17.2) the algorithm described by the formulas (8.4)-(8.7).

The numerical integrations are performed for a flat plate and an elliptic foil. The results are compared to the analytical ones given in Section 18. The agreement is excellent even for a small number of intervals in the numerical integrations, as can be seen in Tables 7-11.

The values of the cavitation number σ and of the cavity volume V for different cavity lengths l are evaluated for a flat plate at $\alpha = 4^\circ$, a NACA 0010 thickness form and a NACA $a = 0.8$ camber meanline of maximum camber $\eta_{\max} = 0.0679$. The related curves are shown in Figures 19 and 20. From those curves and by using the principle of decomposition, we can evaluate the σ vs. l and V vs. l curves for any combination of NACA $a = 0.8$ meanlines and four-digit thickness forms. For example, for a NACA $a = 0.8$ meanline with maximum camber η_{\max} , combined with a four-digit thickness form of maximum thickness τ_{\max} at an angle of attack α degrees, we will have:

$$\sigma = \sigma^a \cdot \frac{\alpha - \alpha_i}{4^\circ} + \sigma^\tau \cdot \frac{\eta_{\max}}{0.0679} + \sigma^\tau \cdot \frac{\tau_{\max}}{0.1} \quad (19.2)$$

$$V = V^a \cdot \frac{\alpha - \alpha_i}{4^\circ} + V^\tau \cdot \frac{\eta_{\max}}{0.0679} + V^\tau \cdot \frac{\tau_{\max}}{0.1} \quad (19.3)$$

where:

σ^a, V^a : correspond to the flat plate at $\alpha = 4^\circ$.

σ^τ, V^τ : correspond to the NACA $a = 0.8$ camber meanline of η_{\max}

b. Elliptic Foil. Consider an ellipse of semi-axes $(1, \epsilon)$ at uniform inflow U_∞ , as shown in Figure 18b. According to the linear theory, the streamwise perturbation velocity on the ellipse will be constant [39]:

$$u_w = \epsilon \cdot U_\infty \quad (18.7)$$

Therefore, if we consider the lower left part of the ellipse as a supercavitating hydrofoil at cavity length $\ell = 2$, then the shape of the cavity will be the rest of the ellipse (in linear theory always), and we will get by inspection:

$$\sigma = 2 \cdot \epsilon \quad (18.8)$$

$$v = \pi \cdot \epsilon \quad (18.9)$$

$$\bar{q}(z) = \frac{1-z^2}{2 \cdot z} ; \quad z > 0 \quad (18.10)$$

$$\bar{v}(z) = 0 ; \quad z \geq t \quad (18.11)$$

Equations (18.8)-(18.11) can also be recovered by substituting in (14.2), (15.3), (16.1) and (17.5) the expression for $\frac{\partial \bar{\eta}_\ell}{\partial x}$:

$$\frac{\partial \bar{\eta}_\ell}{\partial x} = \epsilon \cdot \frac{\omega^2 - 1}{2 \cdot \omega} ; \quad 0 < \omega < 1 \quad (18.12)$$

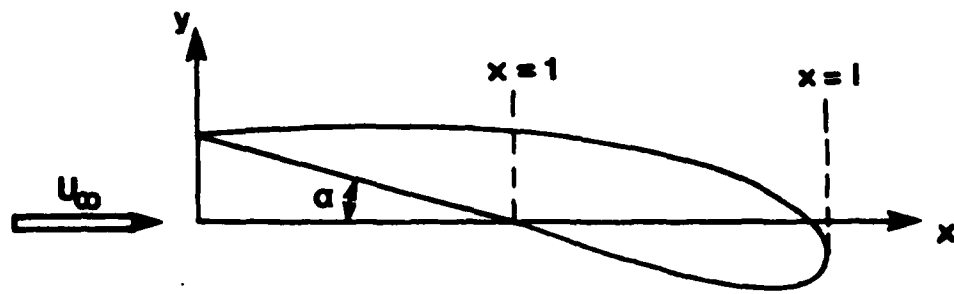
19. Numerical method and results

For general shape hydrofoils, the formulas (14.2), (15.3), (16.1), and (17.5) are computed numerically.

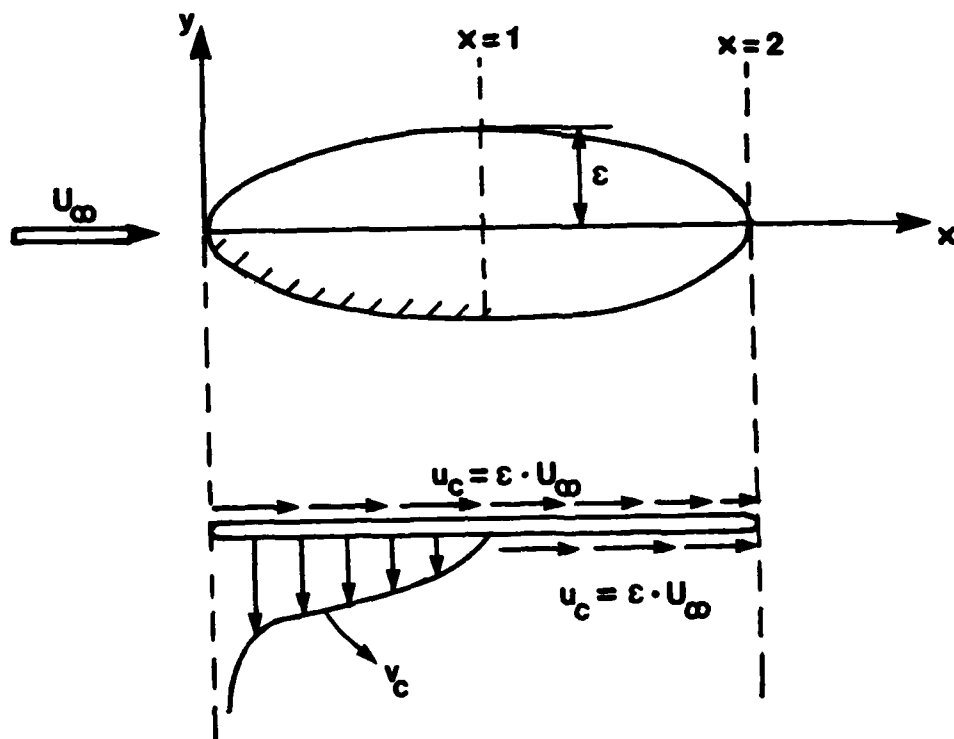
We first define the transformation variable θ as follows:

$$\begin{aligned} n &= t \cdot \sin^2 \left(\frac{\theta}{2} \right) \\ 0 \leq n \leq t \text{ and } 0 \leq \theta \leq \pi \end{aligned} \quad (19.1)$$

Then we express the involved integrals in terms of θ , thus avoiding the



(a)



(b)

Figure 18. Special Cases: Flat Plate (a) and Elliptic Foil (b)

$$\begin{aligned}
& + \sqrt{\frac{z-t}{z}} \cdot \frac{1}{4 \cdot \sqrt{2 \cdot r^2}} \cdot (\sqrt{r^2+1} \cdot z + \sqrt{r^2-1}) - \\
& - \sqrt{\frac{t+z}{z}} \cdot \frac{1}{2 \cdot \pi} \cdot (1+z^2) \cdot \int_0^t \sqrt{\frac{w}{t-w}} \cdot \frac{\theta^*(\omega)}{z+\omega} \cdot \frac{1}{1+\omega^2} \cdot d\omega + \\
& + \sqrt{\frac{z-t}{t}} \cdot \frac{1}{2 \cdot \pi} \cdot (1+z^2) \cdot \int_0^t \sqrt{\frac{w}{t-w}} \cdot \frac{\theta^*(\omega)}{z-\omega} \cdot \frac{1}{1+\omega^2} \cdot d\omega
\end{aligned} \tag{17.5}$$

for $z \geq t$

18. Analytical solutions for some supercavitating hydrofoils

a. Flat Plate. For this case we have

$$\frac{\partial \bar{\eta}_l}{\partial x} = -\alpha \tag{18.1}$$

where α = angle of attack as shown in Figure 18a. Then the equations (14.2), (15.3), (16.1) and (17.5), by using the integrals given in Appendix A, will reduce to the following formulas, also given in [11] and [31]:

$$\sigma = 2 \cdot t \cdot \alpha \tag{18.2}$$

$$\bar{q}(z) = (P - R \cdot z) \cdot \sqrt{\frac{z+t}{z}} ; \quad z < t \tag{18.3a}$$

$$\bar{q}(z) = (P - R \cdot z) \cdot \sqrt{\frac{z+t}{z}} - (P + R \cdot z) \cdot \sqrt{\frac{z-t}{z}} ; \quad z \geq t \tag{18.3b}$$

$$\bar{v}(z) = \frac{1}{2} (P - R \cdot z) \cdot \sqrt{\frac{z+t}{z}} + \frac{1}{2} (P + R \cdot z) \cdot \sqrt{\frac{z-t}{z}} - \frac{1}{2 \cdot t} ; \quad z \geq t \tag{18.4}$$

where: $P = \frac{1}{\sqrt{2 \cdot r^2}} \cdot [\frac{1}{2 \cdot t} \cdot \sqrt{1+r^2} + \frac{1}{2} \cdot \sqrt{r^2-1}]$

$$R = \frac{1}{\sqrt{2 \cdot r^2}} \cdot [-\frac{1}{2 \cdot t} \cdot \sqrt{r^2-1} + \frac{1}{2} \cdot \sqrt{1+r^2}] \tag{18.5}$$

$$v = \frac{\pi \cdot \alpha \cdot t}{16} \Big/ (1 - \sqrt{\frac{l-1}{l}})^2 \tag{18.6}$$

$$\begin{aligned}
\bar{q}(z) = & \left(\frac{t+z}{z}\right)^{\frac{1}{2}} \cdot \frac{1}{2 \cdot \sqrt{2 \cdot r^2}} \cdot (\sqrt{r^2-1} - z \cdot \sqrt{r^2+1}) - \\
& - \frac{1}{\pi} \cdot (1+z^2) \cdot \left(\frac{t+z}{z}\right)^{\frac{1}{2}} \cdot \int_0^t \sqrt{\frac{\omega}{t-\omega}} \cdot \frac{1}{1+\omega^2} \cdot \frac{\theta^*(\omega)}{z+\omega} \cdot d\omega - \\
& - \left(\frac{z-t}{z}\right)^{\frac{1}{2}} \cdot \frac{1}{2 \cdot \sqrt{2 \cdot r^2}} \cdot (\sqrt{r^2+1} \cdot z + \sqrt{r^2-1}) - \\
& - \frac{1}{\pi} \cdot (1+z^2) \cdot \left(\frac{z-t}{z}\right)^{\frac{1}{2}} \cdot \int_0^t \sqrt{\frac{\omega}{t-\omega}} \cdot \frac{1}{1+\omega^2} \cdot \frac{\theta^*(\omega)}{z-\omega} \cdot d\omega \quad (16.1b)
\end{aligned}$$

for $z > t$.

17. Shape of the cavity

The cavity thickness distribution $h(x)$ will be given from the integration of (11.11) as:

$$h(x) = \sigma \cdot \int_0^x \bar{q}(\xi) \cdot d\xi \quad (17.1)$$

The camber distribution $c(x)$ of the cavity in the wake will be given from the integration of (11.12b) as:

$$c(x) = c(1) + \sigma \cdot \int_1^x \bar{v}(\xi) \cdot d\xi \quad (17.2)$$

where $c(1) = \bar{\eta}_l(1) + \frac{h(1)}{2}$ (17.3)

and $\bar{v}(x) = \frac{v_{in}(x)}{\sigma \cdot U_\infty}$ (17.4)

By using (11.13), (13.10), (A.28), (A.27), (A.25) and (A.26), we get this expression for $\bar{v}(z)$:

$$\bar{v}(z) = \sqrt{\frac{t+z}{z}} \cdot \frac{1}{4 \cdot \sqrt{2 \cdot r^2}} \cdot (\sqrt{r^2-1} - z \cdot \sqrt{r^2+1}) +$$

Notice that (14.2) expresses σ as an integral of the slope of the lower hydrofoil surface weighted by terms depending only on the cavity length.

15. Cavity volume V

The cavity volume V , including the hydrofoil, will be given as:

$$V = \int_0^l h(x) \cdot dx = -\sigma \int_0^l x \cdot \bar{q}(x) \cdot dx \quad (15.1)$$

Substituting (13.6) in (15.1) and using (A.28), (A.2), (A.3) and (14.1), we get:

$$V = \frac{\sigma \cdot \pi \cdot l^2}{8} - \sigma \cdot \int_0^l \bar{Y}(\xi) \cdot \xi \cdot \sqrt{\frac{l-\xi}{\xi}} \cdot d\xi \quad (15.2)$$

Finally, by using (13.10), (A.28) and (A.23), (15.2) becomes:

$$V = l^2 \left\{ \frac{\pi \cdot \sigma}{8} - \frac{2}{\pi} \cdot \int_0^t \left[\frac{\sigma \cdot \eta}{2} - \frac{\partial \bar{Y}_l}{\partial x} \right] \cdot \sqrt{\frac{\eta}{t-\eta}} \cdot \frac{1}{1+\eta^2} \cdot J(\eta; t) \cdot d\eta \right\} \quad (15.3)$$

where $J(\eta; t)$ is given in (A.23).

16. Cavity source distribution $\bar{q}(z)$

Starting with (13.11) and by using (13.10), (A.28), (A.24), (A.25) and (A.26), we finally get:

$$\begin{aligned} \bar{q}(z) = & -\theta^*(z) + \left(\frac{t+z}{z} \right)^{\frac{1}{2}} \cdot \frac{1}{2\sqrt{2} \cdot r^2} \cdot (\sqrt{r^2-1} - z \cdot \sqrt{r^2+1}) - \\ & - \frac{1}{\pi} \cdot (1+z^2) \cdot \left(\frac{t+z}{z} \right)^{\frac{1}{2}} \cdot \int_0^t \sqrt{\frac{\omega}{t-\omega}} \cdot \frac{1}{1+\omega^2} \cdot \frac{\theta^*(\omega)}{z+\omega} \cdot d\omega \end{aligned} \quad (16.1a)$$

for $z < t$;

$$\frac{1}{2\pi} \cdot \int_0^t \frac{\bar{\gamma}(\eta) \cdot d\eta}{(1+\eta^2) \cdot (z-\eta)} = \frac{1}{4} \cdot \frac{z}{1+z^2} - \frac{\theta^*(x)}{2} \cdot \frac{1}{1+z^2} \quad (13.9)$$

Inversion of (13.9) gives:

$$\bar{\gamma}(z) = -\frac{1}{\pi} \cdot (1+z^2) \cdot \sqrt{\frac{t-z}{z}} \cdot \int_0^t \sqrt{\frac{\eta}{t-\eta}} \cdot [\frac{\eta}{2} - \theta^*(\eta)] \frac{d\eta}{(1+\eta^2) \cdot (z-\eta)} \quad (13.10)$$

Notice that (13.10) is the unique solution which satisfies also the Kutta condition (13.4).

Substituting (13.8) in (13.6) we get:

$$\bar{q}(z) = -z + \frac{2}{\pi} \cdot z \cdot (1+z^2) \cdot \int_0^t \frac{\bar{\gamma}(\eta) \cdot d\eta}{(z^2-\eta^2) \cdot (1+\eta^2)} \quad (13.11)$$

The formulas (13.10) and (13.11) give the formal solution to our problem as soon as we determine the corresponding cavitation number σ .

14. Cavitation number σ

The cavitation number σ is going to be determined from the closure condition (13.5). By substituting (13.6) in (13.5) and using (A.1), (A.2) and (A.4) we get:

$$-\frac{\pi \cdot l}{2} + \int_0^l d\xi \cdot \sqrt{\frac{l-\xi}{\xi}} \cdot \bar{\gamma}(\xi) = 0 \quad (14.1)$$

By using (13.10), (A.28), (A.22), (A.12) and (A.13), we get the following general expression for σ :

$$\sigma = \frac{4 \cdot \sqrt{2} \cdot r^4}{\pi \cdot (r^2+1)} \cdot \int_0^t \sqrt{\frac{\eta}{t-\eta}} \cdot \frac{1}{(1+\eta^2)^2} \cdot (\sqrt{r^2+1} + \sqrt{r^2-1} \cdot \eta) \cdot \left(-\frac{\partial \bar{\gamma}}{\partial x}\right) \cdot dy \quad (14.2)$$

where: $r^4 = 1 + t^2$. (14.3)

$$\bar{\gamma}(x) = \frac{\gamma_c(x)}{\sigma \cdot U_\infty} , \quad \bar{q}(x) = \frac{q_c(x)}{\sigma \cdot U_\infty} , \quad \theta^*(x) = \frac{1}{\sigma} \cdot \frac{\partial \bar{\eta}_k}{\partial x} \quad (13.1)$$

Then equations (11.7)-(11.10) become:

$$\frac{\bar{\gamma}(x)}{2} - \frac{1}{2\pi} \cdot \int_0^l \frac{\bar{q}(\xi) \cdot d\xi}{\xi - x} = \frac{1}{2} ; \quad 0 < x < l \\ \text{with } \bar{\gamma}(x) = 0 \quad \text{for } l < x < \infty \quad (13.2)$$

$$-\frac{\bar{q}(x)}{2} + \frac{1}{2\pi} \cdot \int_0^1 \frac{\bar{\gamma}(\xi) \cdot d\xi}{\xi - x} = \theta^*(x) ; \quad 0 < x < 1 \quad (13.3)$$

$$\bar{\gamma}(1) = 0 \quad (13.4)$$

$$\int_0^l \bar{q}(x) \cdot dx = 0 \quad (13.5)$$

Using similar procedures as described in [16] and [31], we derive the solution to the system of singular integral equations (13.2)-(13.5) as follows:

Inverting first (3.2) we get:

$$\bar{q}(x) = -\sqrt{\frac{x}{l-x}} + \frac{1}{\pi} \cdot \sqrt{\frac{x}{l-x}} \cdot \int_0^1 \sqrt{\frac{l-\xi}{\xi}} \cdot \frac{\bar{\gamma}(\xi) \cdot d\xi}{x-\xi} \quad (13.6)$$

Notice that this is the unique solution which behaves like $\frac{1}{\sqrt{l-x}}$ at the trailing edge of the cavity (T. Y. Wu's singularity [43]).

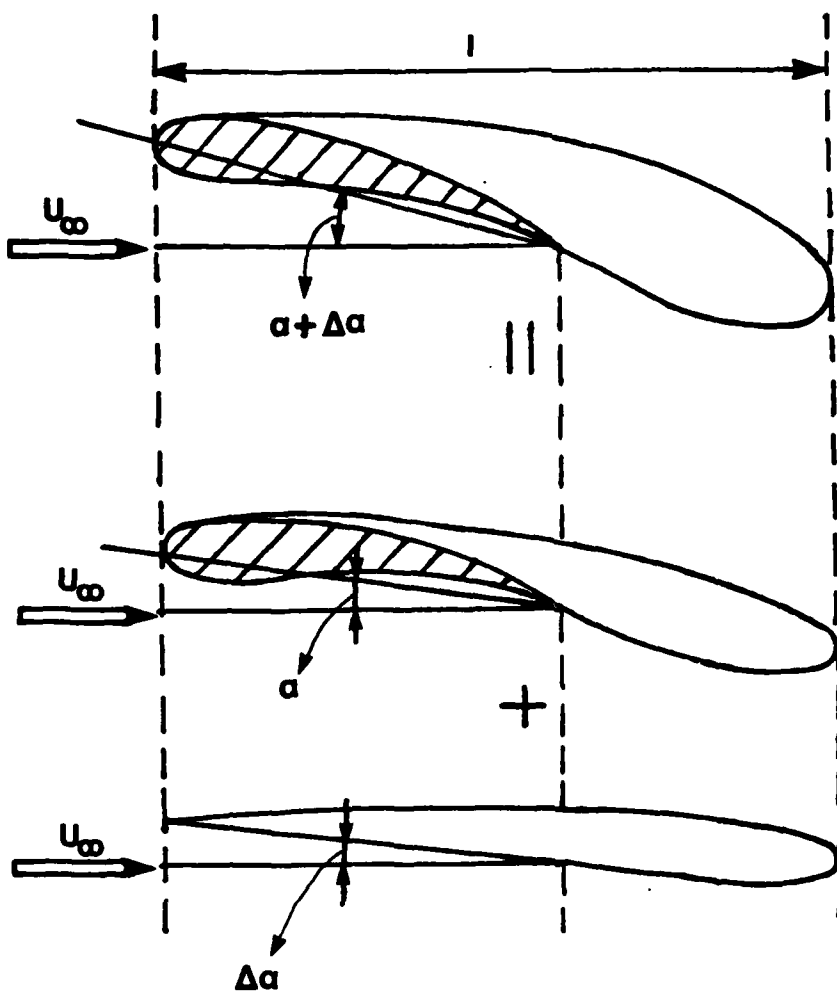
Substituting (13.6) in (13.3) we finally get:

$$\frac{1}{2\pi} \cdot \int_0^1 \left(\sqrt{\frac{l-x}{x}} + \sqrt{\frac{l-\xi}{\xi}} \right) \cdot \frac{\bar{\gamma}(\xi) \cdot d\xi}{x-\xi} = \frac{1}{2} - \theta^*(x) \cdot \sqrt{\frac{l-x}{x}} \quad (13.7)$$

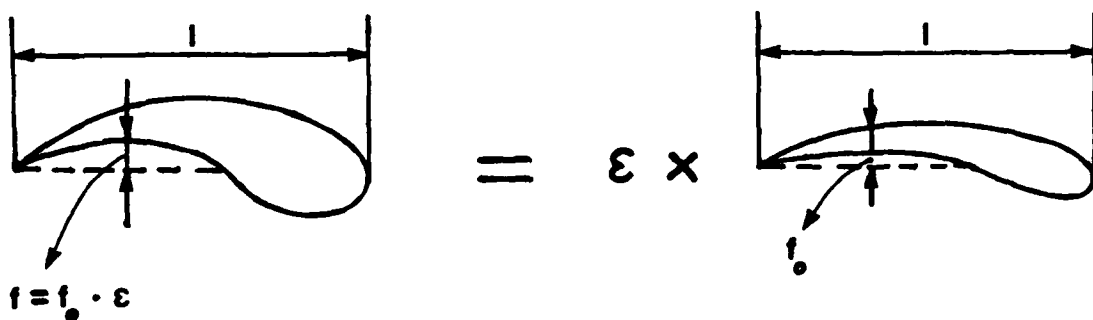
Using the transformation:

$$z = \sqrt{\frac{x}{l-x}} , \quad \eta = \sqrt{\frac{\xi}{l-\xi}} , \quad t = \sqrt{\frac{1}{l-1}} \quad (13.8)$$

(13.7) becomes:



(a)



(b)

Figure 17. Change in the Angle of Attack (a) or in the Scale (b)

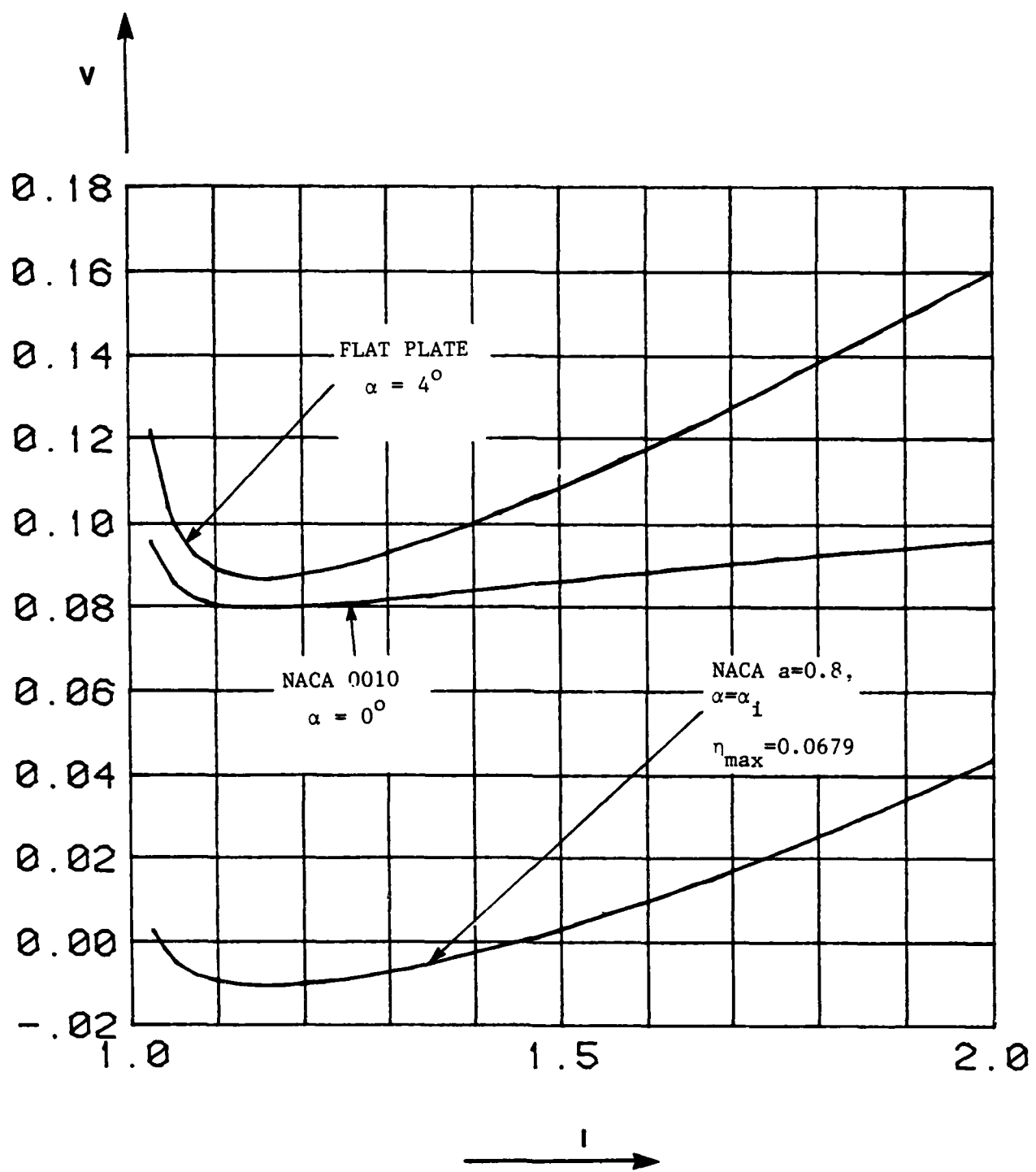
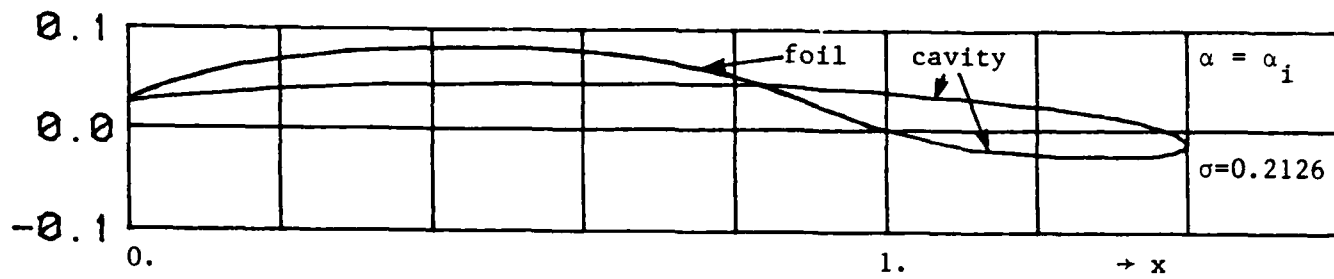
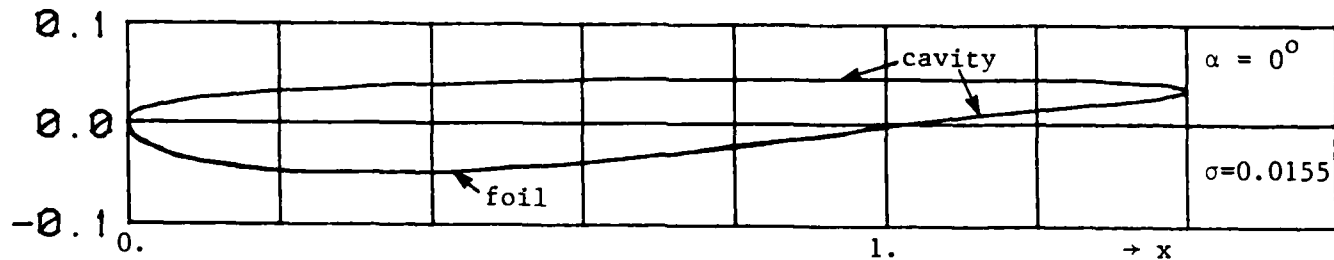


Figure 20. V vs. l for some Supercavitating Hydrofoils

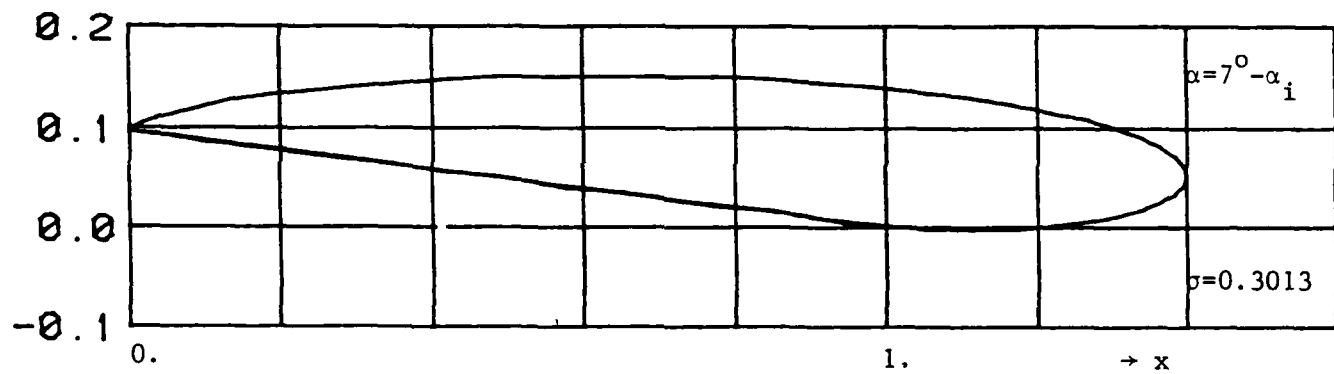
(a) NACA $a = 0.8$ ($n_{\max} = 0.0679$)



(b) NACA 0010



(c) FLAT PLATE



(d) NACA $a = 0.8$ and NACA 0010

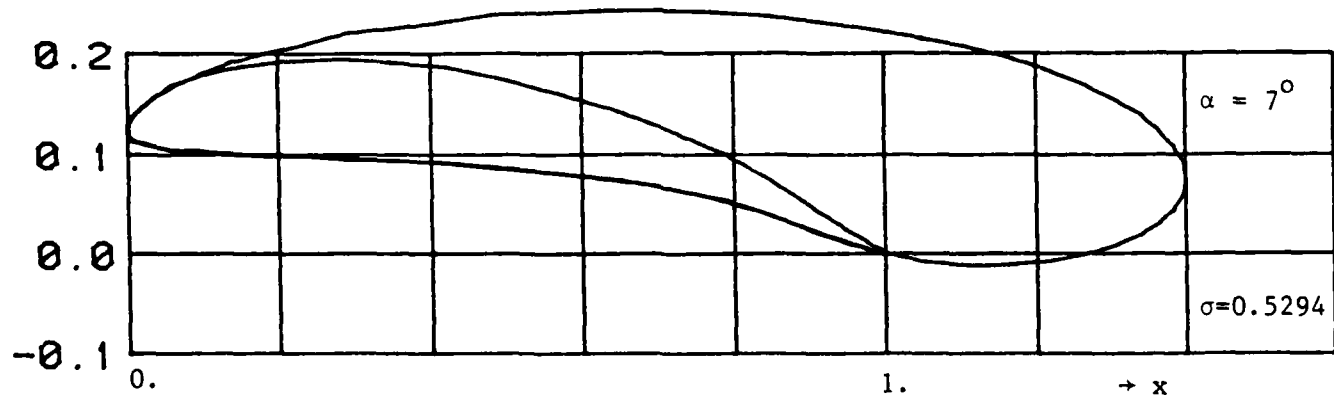


Figure 21. The Three Elementary Problems for NACA $a = 0.8$ combined with NACA 0010 at $\alpha = 7^\circ$ and $\ell = 1.4$; (a) + (b) + (c) = (d).

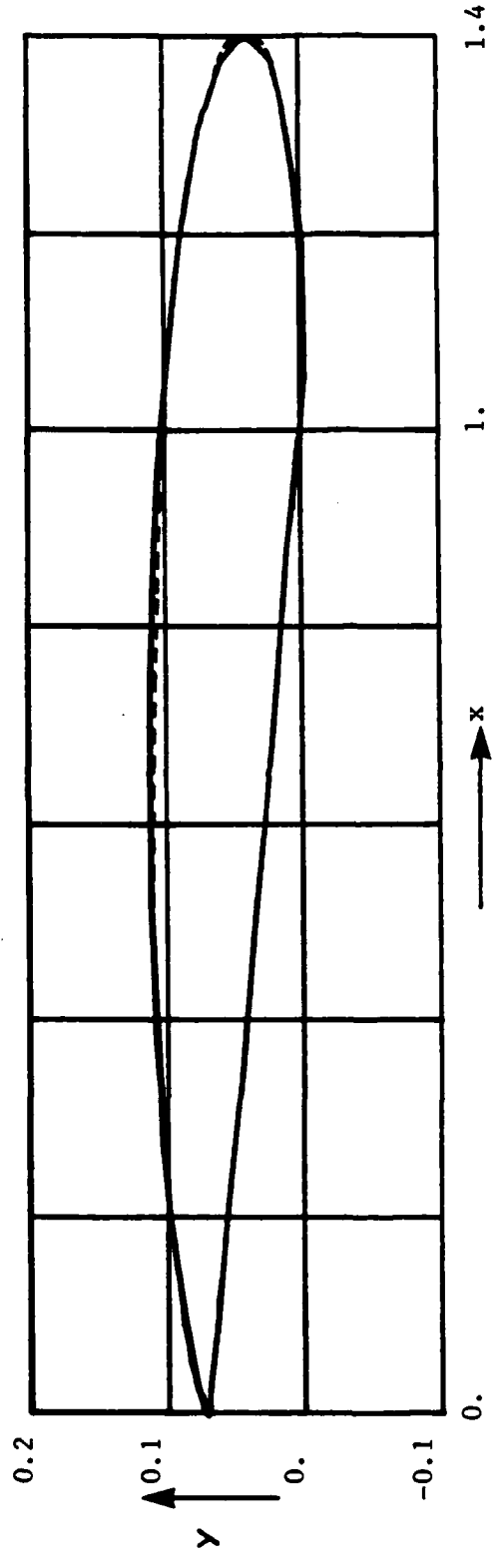


Figure 22. Cavity Plots for Flat Plate at $\alpha = 4^\circ$, $l = 1.4$

— linear theory, $\sigma = 0.221$

- - - nonlinear theory [38], $\sigma = 0.219$

PART C. CORRECTIONS TO THE LINEAR CAVITATING HYDROFOIL THEORY

20. Lighthill's correction for non-cavitating hydrofoils

The linear theory for non-cavitating hydrofoils has already been described in Section 1. The linear solution is not valid at a region close to the leading edge of the hydrofoil, where a stagnation point appears and the perturbation velocities (u , v) are not small anymore compared to the freestream velocity U_∞ . That region of the non-uniformity of the solution is of the order of the leading edge radius ρ_L as proved by Lighthill in [25] where also a uniformly valid expression for the surface velocity is given as follows:

$$q_s^\pm = (U_\infty + u_w^\pm) \cdot \sqrt{\frac{x}{\rho_L}} + O(\epsilon^2) \quad (20.1)$$

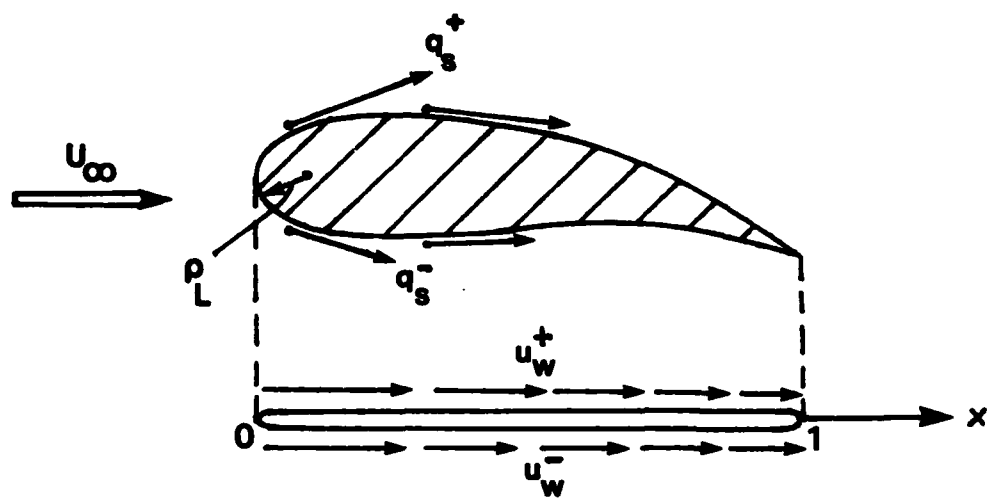
where ϵ is our small parameter and u_w^\pm are the linear streamwise perturbation velocities on the upper (+) and the lower (-) surfaces of the hydrofoil as shown in Figure 23a.

For example, for a symmetric hydrofoil at an angle of attack α , the upper surface velocity will be given as:

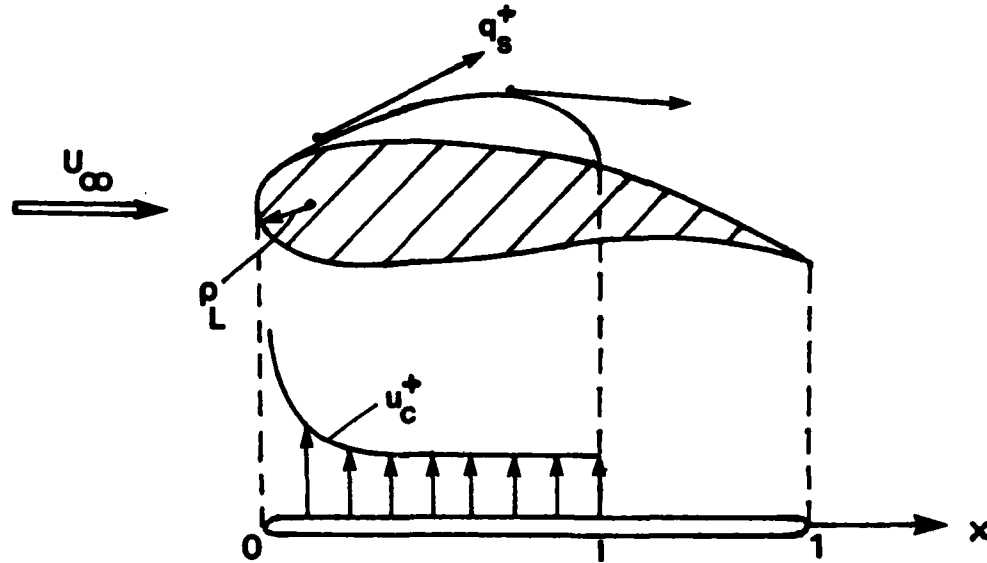
$$q_s^+ = U_\infty \left(1 + u_w^\tau + \frac{\alpha}{\sqrt{x}} \right) \cdot \sqrt{\frac{x}{x + \frac{\rho_L}{2}}} \quad (20.2)$$

where u_w^τ is the linear streamwise perturbation velocity due to the thickness distribution and given by (1.7).

The minimum pressure point will be on the suction (upper) surface of the hydrofoil where the maximum of q_s^+ occurs. For sufficient angle of attack, the minimum pressure point will be close to the leading edge, at a chordwise location x_{min} . In the case of a symmetric hydrofoil, x_{min} will correspond to the point which maximizes the RHS of equation (20.2). For slowly varying u_w^τ at the



(a)



(b)

Figure 23. Lighthill's correction for non-cavitating flow (a) and cavitating flow (b).

leading edge region, which is the usual case, x_{\min} is given as:

$$x_{\min} = \frac{(1+u_w^T)^2 \cdot \rho_L^2}{4 \cdot \alpha^2} \quad (20.3)$$

where u_w^T is taken at $x = 0$. The maximum surface velocity $q_{s,\max}^+$ is given from (20.2) for $x = x_{\min}$. The inception cavitation number σ_{inc} will then be:

$$\sigma_{inc} = (q_{s,\max}^+)^2 - 1 \quad (20.4)$$

The values for σ_{inc} given by (20.4) agree very well with the ones predicted by non-linear theory [5]. This indicates that linear theory with the Lighthill's correction gives sufficiently good results for the surface velocity for hydrofoils of practical applications.

21. Lighthill's correction for cavitating hydrofoils

Suppose now that the hydrofoil has a cavity of length ℓ on its upper surface as shown in Figure 23b. Then the leading edge radius of the cavity-hydrofoil remains the same, as proven in Appendix B. Therefore the velocity on the cavity surface will be given as follows:

$$q_s^+ = (U_\infty + u_c^+) \cdot \sqrt{\frac{x}{\frac{x}{\rho_L} + \frac{\ell}{2}}} ; \quad 0 < x < \ell \quad (21.1)$$

where u_c^+ is the linear streamwise perturbation velocity on the cavity surface. According now to the non-linear theory, the velocity on the cavity has to be [38]:

$$q_s^+ = \sqrt{1 + \sigma} \cdot U_\infty \quad (21.2)$$

Combining (21.1) and (21.2), we end up with the following dynamic boundary condition:

$$u_c^+ = U_\infty \cdot [\sqrt{1+\sigma} \cdot \sqrt{\frac{x+\frac{\rho_L}{2}}{x}} - 1] ; \quad 0 < x < l \quad (21.3)$$

Equation (21.3) requires u_c^+ to be square root singular at the leading edge, matching asymptotically to a constant value over the main body of the cavity. In fact this is equivalent to a virtually varying cavitation number over the cavity length.

The kinematic boundary conditions will be the same as (2.2) and (2.3). Following a similar analysis as described in Section 2, we end up with the following equations for the cavity source and vortex distributions $q(x)$ and $\gamma(x)$:

$$-\frac{q(x)}{2} + \frac{1}{2\pi} \cdot \int_0^l \frac{\gamma(\xi) \cdot d\xi}{\xi-x} = 0; \quad 0 < x < l \quad (2.21)$$

$$\frac{\gamma(x)}{2} - \frac{1}{2\pi} \cdot \int_0^l \frac{q(\xi) \cdot d\xi}{\xi-x} = u_c^+ - u_w^+ ; \quad 0 < x < l \quad (21.4)$$

$$\gamma(l) = \text{finite} \quad (2.23)$$

$$\int_0^l q(\xi) \cdot d\xi = 0 \quad (2.25)$$

Notice that equations (2.21), (2.23) and (2.25) are the same as in linear theory. Equation (21.4) can be written as:

$$\begin{aligned} \frac{\gamma(x)}{2} - \frac{1}{2\pi} \cdot \int_0^l \frac{q(\xi) \cdot d\xi}{\xi-x} - U_\infty \cdot [\sqrt{1+\sigma} - 1] &= \\ = U_\infty \cdot \sqrt{1+\sigma} \cdot [\sqrt{\frac{x+\frac{\rho_L}{2}}{x}} - 1] - u_w^+ & \end{aligned} \quad (21.5)$$

The left-hand side of equation (21.5) is in a similar form as that of equation (2.26). Therefore the coefficient of U_∞ in the left-hand side of (21.5) will be given, according to (5.8), as follows:

$$(\sqrt{1+\sigma} - 1) = \int_0^s \frac{u_w^+ - U_\infty \cdot \sqrt{1+\sigma} \cdot \left[\frac{x+\frac{\rho_L}{2}}{x} - 1 \right]}{U_\infty} \cdot f(n; s) \cdot dn \quad (21.6)$$

The cavitation number σ_L from linear theory is:

$$\sigma_L = \int_0^s \frac{2 \cdot u_w^+}{U_\infty} \cdot f(n; s) \cdot dn \quad (21.7)$$

By using now (7.21) and (21.7), (21.6) renders:

$$\sigma = \left[\frac{1 + \frac{\sigma_L}{2}}{a(\rho_L; l)} \right]^2 - 1 \quad (21.8)$$

where $a(\rho_L; l)$ is defined as:

$$a(\rho_L; l) = \int_0^s \sqrt{\frac{x + \frac{\rho_L}{2}}{x}} \cdot f(n; s) \cdot dn \quad (21.9)$$

Equation (21.8) gives the cavitation number σ in terms of the linear cavitation number σ_L and the leading edge correction factor $a(\rho_L; l)$. Some graphs of $a(\rho_L; l)$ as a function of l for different ρ_L are shown in Figure 24. The values of $a(\rho_L; l)$ have been evaluated by carrying out the numerical integration in (21.9) after making the transformation (8.1). Notice that as ρ_L increases with l fixed $a(\rho_L; l)$ also increases and therefore σ decreases, according to (21.8). This implies that for the same σ , the bigger the leading edge radius, the smaller the cavity it is, something which is also observed in the experiments described in Part D.

After the cavitation number σ has been determined by using equation (21.8), the right-hand side of (21.5) is known. Therefore we can proceed with the solution of the system of integral equations (2.21), (21.5) subject to the restrictions (2.23) and (2.25). The left-hand side of those equations is in the same form as in the linear theory described in Section 2. Therefore the solution and the results will be given by the same formulas (8.3), (6.1) and (6.5) where instead of u_w^+ and σ , the negative of the right-hand side of (21.5) and

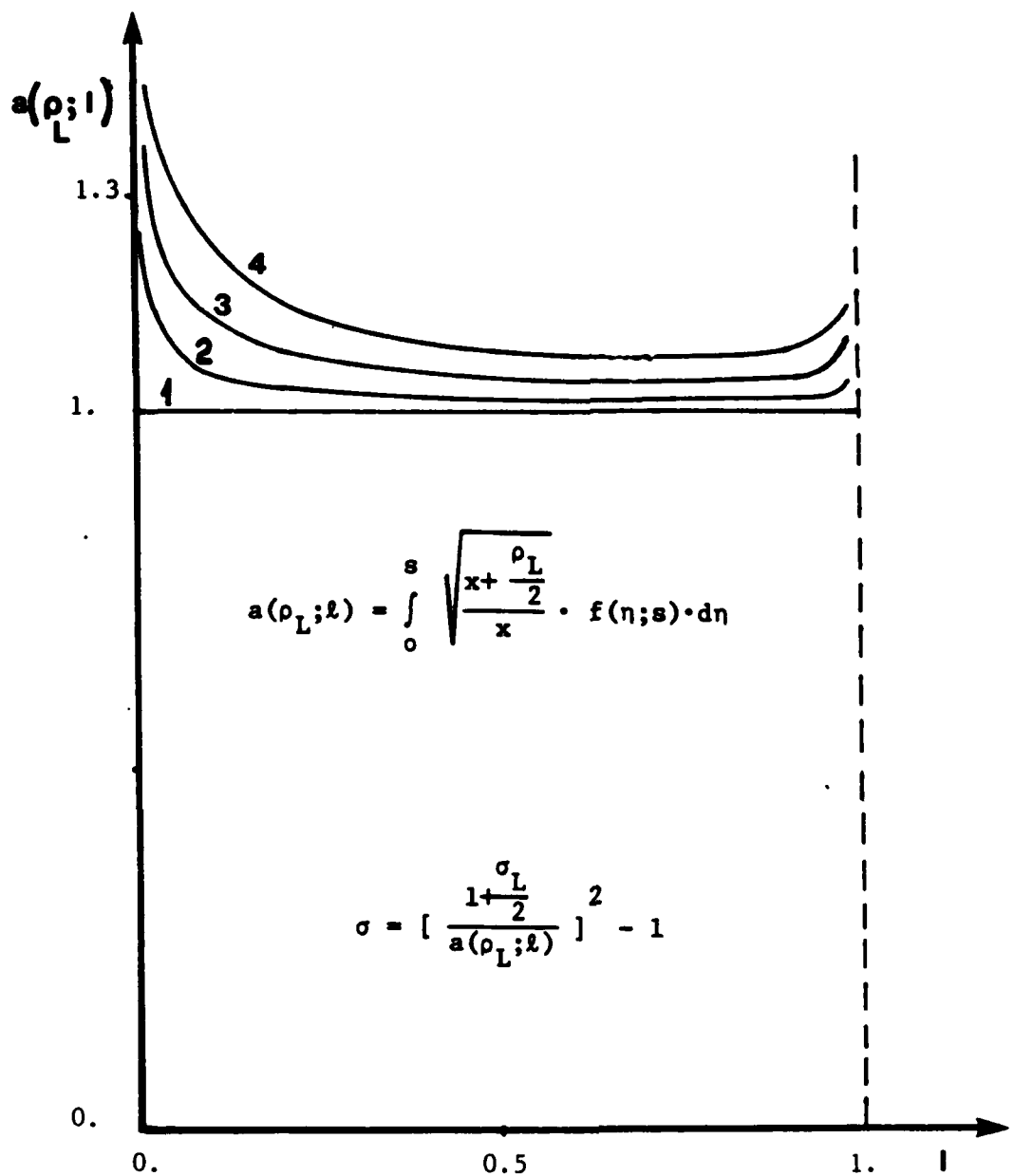


Figure 24. Graph of the leading edge radius correction factor $a(\rho_L; l)$ for different values of ρ_L .

- 1: $\rho_L = 0$
- 2: $\rho_L = 0.0004$
- 3: $\rho_L = 0.0016$
- 4: $\rho_L = 0.0036$

$2.(\sqrt{1+\sigma}-1)$ must be put respectively. The numerical integrations are performed by following the same method described in Section 8. As an application the effect of the leading edge radius on the cavitation of a flat plate is considered. In this case u_w^+ is given by (7.3). The characteristic curves for a flat plate at $\alpha = 4$ degrees and different leading edge radii are shown in Figure 25. The cavity plots are also shown for $a/\sigma = 0.06$. Notice the drastic reduction of the cavity volume as we increase the leading edge radius. This is of the same magnitude as that predicted by Tulin and Hsu [36].

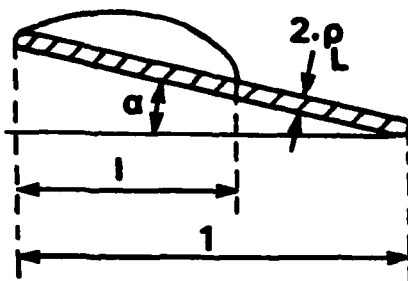
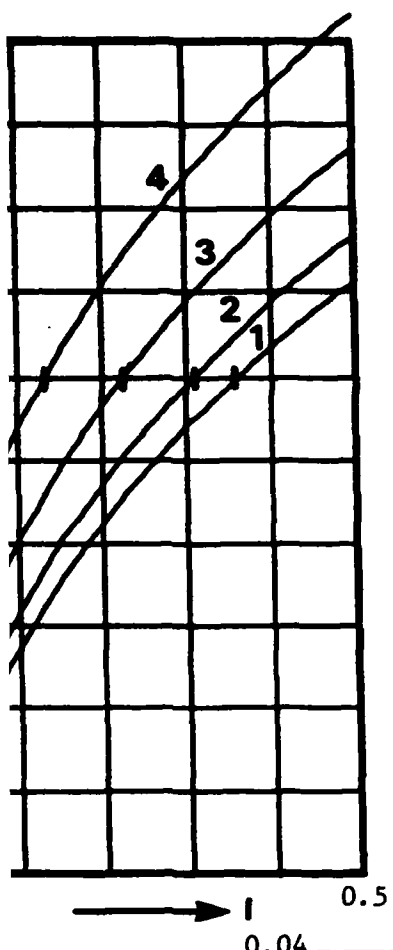
Finally, the cavity plots for three NACA 16 thickness forms at $\alpha = 4^\circ$ and $\sigma = 1.07$ are shown in Figures 26 and 27, as predicted by pure linear theory and by the linear theory including the non-linear leading edge corrections. The following conclusions can be drawn from the comparison between Figures 26 and 27:

a) Pure linear theory predicts that by increasing the thickness of the hydrofoil, the cavity also increases for constant flow conditions (i.e., α and σ).

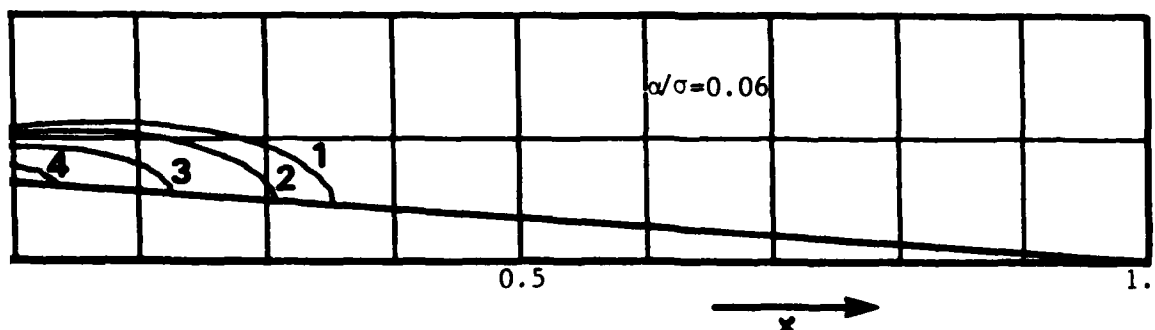
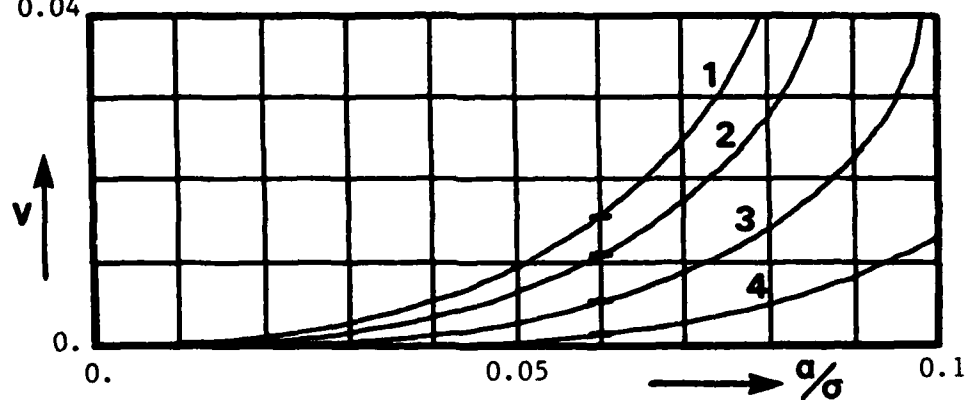
b) Linear theory, including the leading edge radius corrections, predicts that by increasing the thickness and thus the leading edge radius, the cavity decreases for constant flow conditions. This is the same trend as that observed in the experiments described in Part D.

22. Effect of the location of the cavity detachment point on the cavity shape

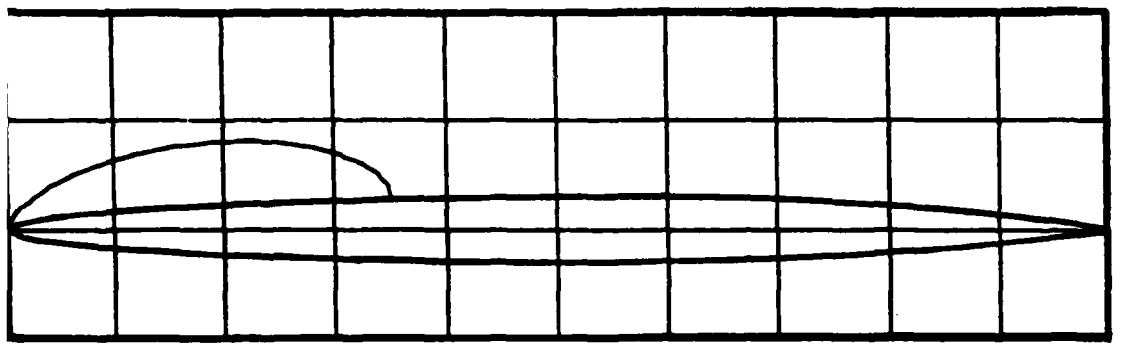
Looking in Figure 27, we already pointed out that as we increase the thickness of the hydrofoil, the cavity becomes smaller and smaller for constant flow conditions. We might anticipate that as we go on increasing the thickness of the foil we will eventually reach the



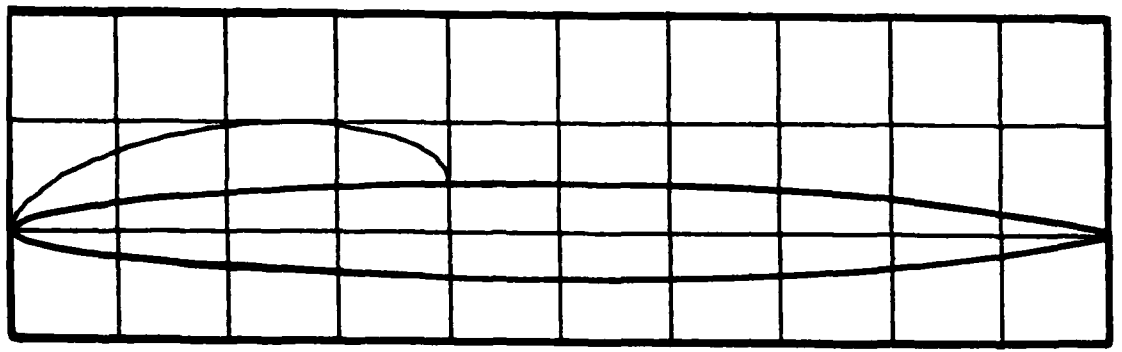
1: $\rho_L = 0.$
 2: $\rho_L = 0.0004$
 3: $\rho_L = 0.0016$
 4: $\rho_L = 0.0036$



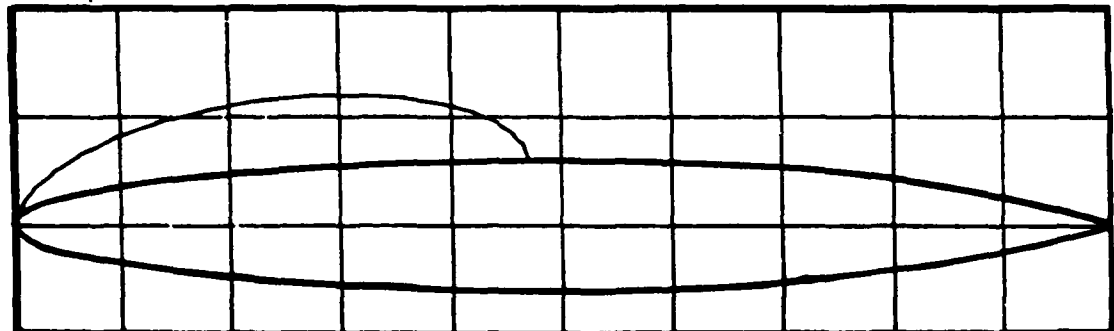
Flat plate with leading edge radius ρ_L , at $\alpha = 4^\circ$.



$x=0$ $x=1$
NACA 16-006

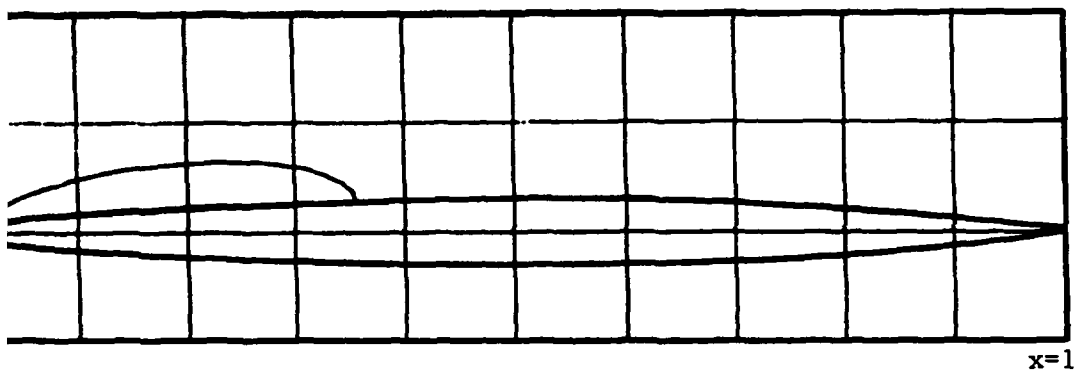


$x=0$ $x=1$
NACA 16-009

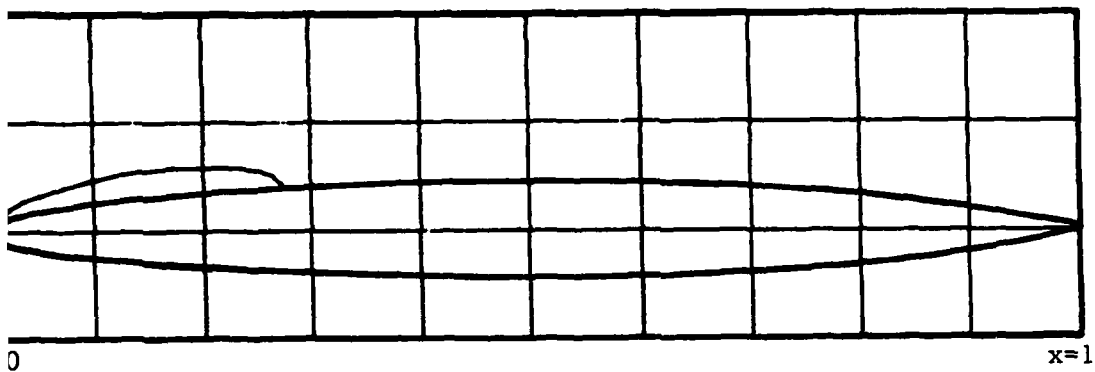


$x=0$ $x=1$
NACA 16-012

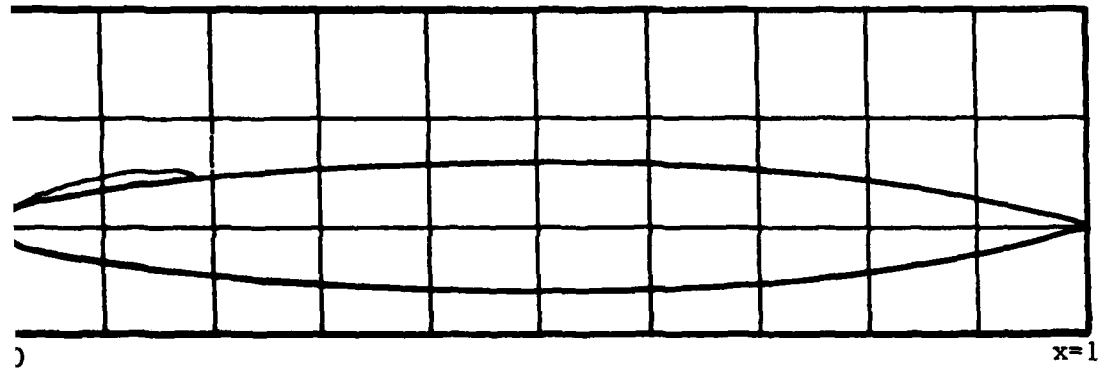
re 26. Pure linear theory.
All hydrofoils at $\alpha = 4^\circ$ and $\sigma = 1.07$.



NACA 16-006



NACA 16-009



NACA 16-012

27. Linear theory including leading edge corrections.
All hydrofoils at $\alpha = 4^\circ$ and $\sigma = 1.07$.

on situation after which no cavity will appear on the foil.

be proven by taking the limit of equation (21.8) as $\ell \rightarrow 0$. By 21.7), (21.9), and (7.21), we get:

$$\lim_{x \rightarrow 0} [(1+u_w^+(x)) \cdot \sqrt{\frac{x}{\rho_L}}]^2 - 1 ; \quad \text{as } \ell \rightarrow 0 \quad (22.1)$$

$$\sigma = [q_s^+(0)]^2 - 1 \quad (22.2)$$

In words, the inception cavitation number corresponds to the velocity at the leading edge for the non-cavitating problem. The correct cavitation number is given by (20.4) and corresponds to the surface velocity at $x = x_{\min}$. Therefore we will predict the cavitation number if we start the cavity at $x = x_{\min}$. The formulation of the linear partially cavitating hydrofoil with the cavity starting after the leading edge will be similar one described in Section 2. If the cavity starts at $x = \ell_0$, the boundary conditions will become:

The kinematic boundary conditions:

$$u_c(x, 0^+) = U_\infty \cdot \frac{\partial \bar{\eta}_u}{\partial x} ; \quad 0 < x < \ell_0 \text{ and } \ell_0 < x < 1 \quad (22.3)$$

$$u_c(x, 0^-) = U_\infty \cdot \frac{\partial \bar{\eta}_u}{\partial x} ; \quad 0 < x < 1 \quad (22.4)$$

The dynamic boundary condition:

$$u_c(x, 0^+) = \frac{\sigma}{2} \cdot U_\infty ; \quad \ell_0 < x < \ell \quad (22.5)$$

Cavity source and cavity vortex distributions $q(x)$ and $\gamma(x)$ will now the equations:

$$-\frac{q(x)}{2} + \frac{1}{2\pi} \cdot \int_0^1 \frac{\gamma(\xi) \cdot d\xi}{\xi - x} = 0; \quad 0 < x < 1 \quad (22.6)$$

AD-A158 105

NON-LINEAR CORRECTIONS TO THE LINEAR THEORY FOR THE
PREDICTION OF THE CAV. (U) MASSACHUSETTS INST OF TECH
CAMBRIDGE DEPT OF OCEAN ENGINEERIN. S A KINNAS JUN 85

2/2

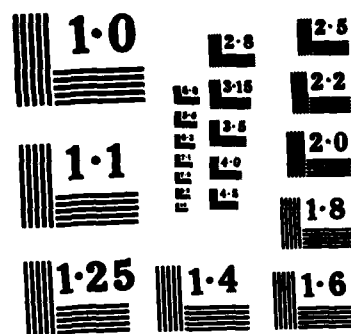
UNCLASSIFIED

OE-85-10 N00014-84-K-0067

F/G 2/4

NL

END
FILMED
SAC



NATIONAL BUREAU OF STANDARDS
MICROCOPY RESOLUTION TEST CHART

$$\frac{\gamma(x)}{2} - \frac{1}{2\pi} \cdot \int_{l_0}^l \frac{q(\xi) \cdot d\xi}{\xi - x} - \frac{\sigma}{2} \cdot U_\infty = -u_w(x, 0+) \quad (22.7)$$

for $l_0 < x < l$

$$\gamma(l) = \text{finite} \quad (22.8)$$

$$\int_{l_0}^l q(\xi) \cdot d\xi = 0 \quad (22.9)$$

where: $q(x) = U_\infty \cdot \frac{dh}{dx}; \quad l_0 < x < l \quad (22.10)$

$$q(x) = 0; \quad 0 < x < l_0 \text{ and } l < x < 1 \quad (22.11)$$

We observe again that the solution σ , $\gamma(x)$, $q(x)$ to the system of equations (22.6)-(22.9) is unique and depends only on the distribution of the perturbation velocity $u_w(x, 0+)$ for $l_0 < x < l$. The decomposition of the problem into elementary problems as described in Section 3 still applies as long as we keep the start and the end of the cavity fixed throughout all those problems. By using a similar procedure as the one described in Section 4, we derive the source distribution $q(z)$ as follows:

$$q(z) = \frac{1}{\pi} \cdot \frac{(1+z)^2}{z} \cdot \sqrt{\frac{z-s_0}{s-z}} \cdot \int_{s_0}^s \sqrt{\frac{s-n}{n-s_0}} \cdot \frac{n}{1+n^2} \cdot \frac{1}{z-n} \cdot \left(u_w^+ - \frac{\sigma \cdot U_\infty}{2} \right) \cdot dn \quad (22.12)$$

for $s_0 < z < s$

where: $s_0 = \sqrt{\frac{l_0}{1-l_0}}$ (22.13)

The cavitation number σ , as proven in Appendix C, can be expressed as:

$$\sigma = \int_{s_0}^s \frac{2 \cdot u_w^+(\eta)}{U_\infty} \cdot \bar{f}(\eta; s, s_0) \cdot d\eta \quad (22.14)$$

where:

$$\bar{f}(\eta; s, s_0) = \frac{\eta}{(1+\eta^2)^2} \cdot \sqrt{\frac{s-\eta}{\eta-s_0}} \cdot \left[\frac{\pi-C_3}{C_5} - \frac{C_4}{C_5} \cdot \eta \right] \quad (22.15)$$

The constants C_3 , C_4 , C_5 are functions of s and s_0 defined in Appendix C. The function $\bar{f}(\eta; s, s_0)$ again satisfies the restriction:

$$\int_{s_0}^s \bar{f}(\eta; s, s_0) \cdot d\eta = 1 \quad (22.16)$$

Notice that the formulas (22.12), (22.14) and (22.15) reduce to (4.5), (5.8) and (5.9) respectively as $s_0 \rightarrow 0$ (i.e., $l_0 \rightarrow 0$).

The cavity source distribution can also be written as:

$$q(z) = -\frac{1}{\pi} \cdot \frac{1+z^2}{z} \cdot \sqrt{\frac{z-s_0}{s-z}} \cdot \int_{s_0}^s \sqrt{\frac{s-\eta}{\eta-s_0}} \cdot \frac{\eta}{1+\eta^2} \cdot \frac{u_w^+(z)-u_w^+(\eta)}{z-\eta} \cdot d\eta + \\ + [\sigma \cdot U_\infty - 2 \cdot u_w^+(z)] \cdot \frac{1}{z} \cdot \sqrt{\frac{z-s_0}{s-z}} \cdot \left[\frac{C_2}{2} - \frac{C_1 + \pi}{2} \cdot z \right] \quad (22.17)$$

where the constants C_1 , C_2 are functions of s and s_0 defined in Appendix C.

For general shape hydrofoils, the expressions (22.14) and (22.17) are evaluated by making the transformation:

$$\eta = s_0 + (s-s_0) \cdot \sin^2\left(\frac{\theta}{2}\right)$$

with $s_0 \leq \eta \leq s$ and $0 \leq \theta \leq \pi$

$$(22.18)$$

Then the involved integrations are performed numerically by using Simpson's rule in θ .

The cavity shape is found from the numerical integration of (22.10) by using the algorithm described by the equations (8.4), (8.5) and (8.6), with ϕ defined as follows:

$$\xi = l_0 + (l-l_0) \cdot \sin^2\left(\frac{\phi}{2}\right)$$

$$l_0 \leq \xi \leq l \quad \text{and} \quad 0 \leq \phi \leq \pi \quad (22.19)$$

As an application, the partial cavitation for a NACA 16-015 thickness form at $\alpha = 4^\circ$ has been considered, as illustrated in Figure 28. The cavity shapes are shown for different starting positions $x = l_0$ and the same end position $x = l = 0.5$. Notice the substantial reduction in the cavity volume and the cavitation number as we move the start of the cavity from $x = 0$ to $x = x_{\min}$ as given by (20.3). By starting the cavity farther beyond than $x = x_{\min}$, the cavity decreases but now the pressure minimum will occur on the wetted part of the foil in front of the cavity, something which is physically unacceptable. In Figure 29, the cavity shapes are shown for a NACA 16-006 thickness form at $\alpha = 4^\circ$ and for $l_0 = 0$, $l_0 = x_{\min}$. Comparing Figure 29 to Figure 28, we observe that starting the cavity at $l_0 = x_{\min}$ has smaller effect on the solution, the thinner the hydrofoil.

The leading edge corrections can also be included when the cavity starts at $x = l_0 > 0$. In that case, the dynamic boundary condition on the cavity surface will become:

$$u_c^+ = U_\infty \cdot \left[\sqrt{1+\sigma} \cdot \sqrt{\frac{x + \frac{\rho_L}{2}}{x}} - 1 \right] ; \quad l_0 < x < l \quad (22.20)$$

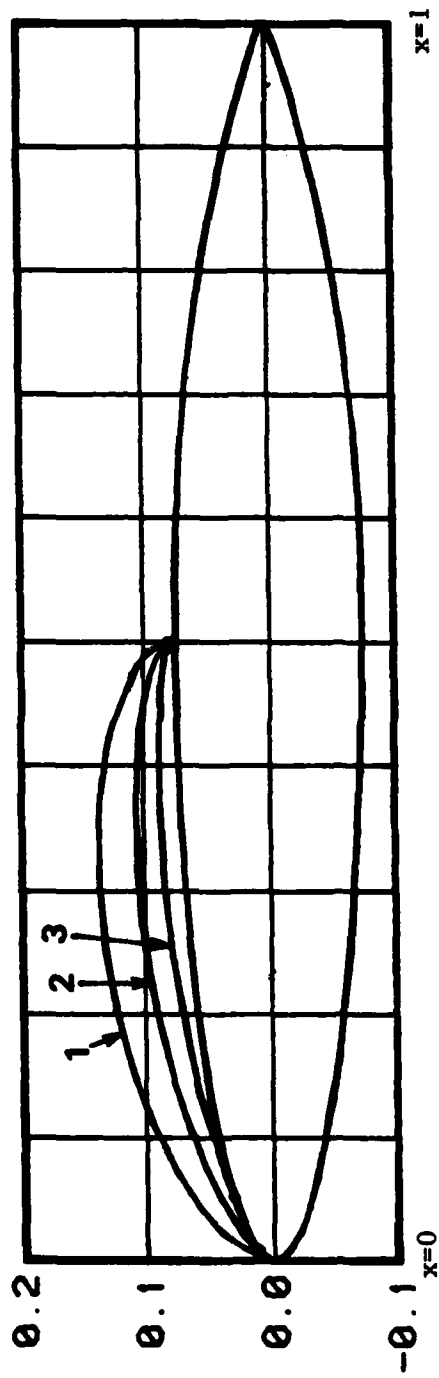
The cavitation number σ will again be given by (21.8) where now σ_L

corresponds to the linear theory with the same ℓ_0 and ℓ , and where instead of $a(\rho_L; \ell)$, $\bar{a}(\rho_L; \ell, \ell_0)$ is used, defined as:

$$\bar{a}(\rho_L; \ell, \ell_0) = \int_{s_0}^s \sqrt{\frac{x + \frac{\rho_L}{2}}{x}} \cdot \bar{f}(n; s, s_0) \cdot dn \quad (22.21)$$

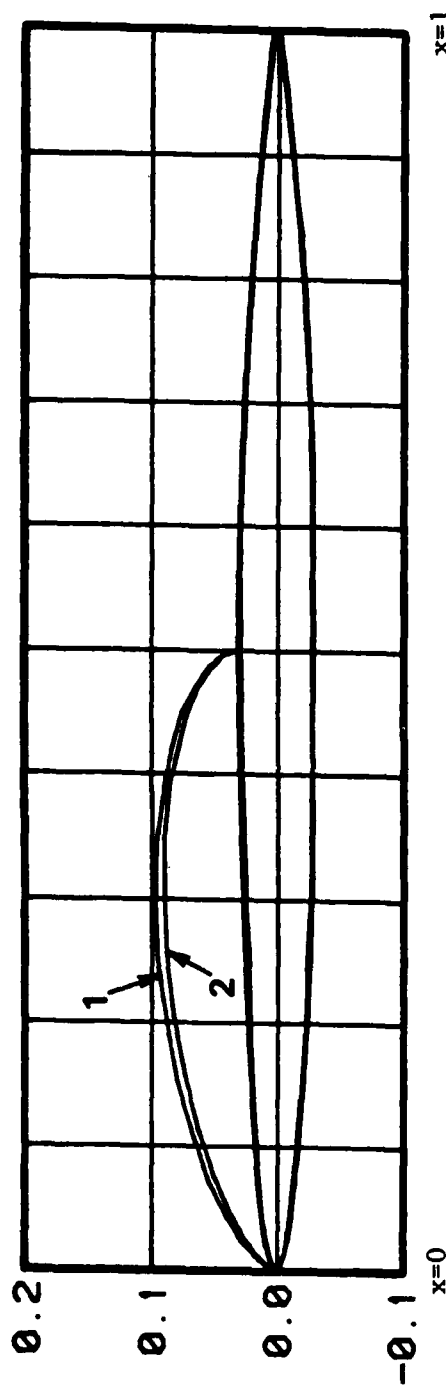
After σ has been determined, we proceed by solving the linear problem with the same ℓ_0 and ℓ , but with u_w^+ replaced by the negative of the right-hand side of (21.5). In Figure 30, the cavity shapes for a NACA 16-006 thickness form at $\alpha = 4^\circ$ and $\ell = 0.5$, are shown for $\ell_0 = 0$ and $\ell_0 = x_{\min}$, as predicted by the linear theory, including the leading edge corrections. Notice the negligible differences between the two cavity shapes and their cavitation numbers. This means that in the linear theory with leading edge corrections, the point where the cavity starts has little effect on the solution, something which has also been concluded from the non-linear theory [38]. However, by letting $\ell_0 = x_{\min}$, we predict the right cavitation inception number.

By comparing Figure 30 with Figure 14, we also observe that including the leading edge corrections makes the cavity thinner and, in fact, closer to the non-linear result. However, the predicted cavitation number is still higher than the non-linear one. The predicted cavity shape for the same cavitation number as the non-linear one is shown in Figure 31a. It seems that we still overpredict the cavity volume for fixed flow conditions, but not as much as with pure linear theory. Nevertheless, including the leading edge corrections makes the cavity shape very close to the non-linear one at its beginning. The discrepancies at the end of the cavity can partly be attributed to the different cavity termination models in the two theories. This is encouraged by the fact that non-linear theory using



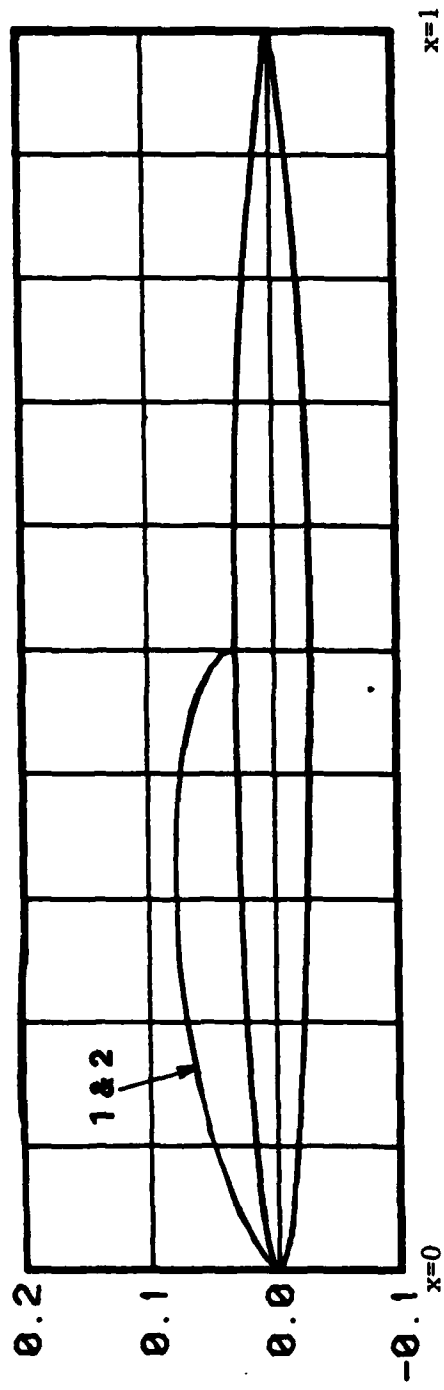
l_0	σ
1	0.
2	$x_{\min} = 0.00843$
3	0.05

Figure 28. Cavity plots for NACA 16-015 at $\alpha = 4^\circ$ for fixed $\ell = 0.5$ and different values of l_0 using pure linear theory.



l_0	σ
1	0. . 1.15
2	$x_{min} = 0.00018$ 1.08

Figure 29. Cavity plots for NACA 16-006 at $\alpha = 4^\circ$ for fixed $l = 0.5$ and different values of l_0 using pure linear theory.



I_0	σ
1	0.
2	$x_{\min} = 0.00018$

Figure 30. Cavity plots for NACA 16-006 at $\alpha = 4^\circ$ for fixed $\lambda = 0.5$ and different values of ℓ_o using linear theory including leading edge corrections.

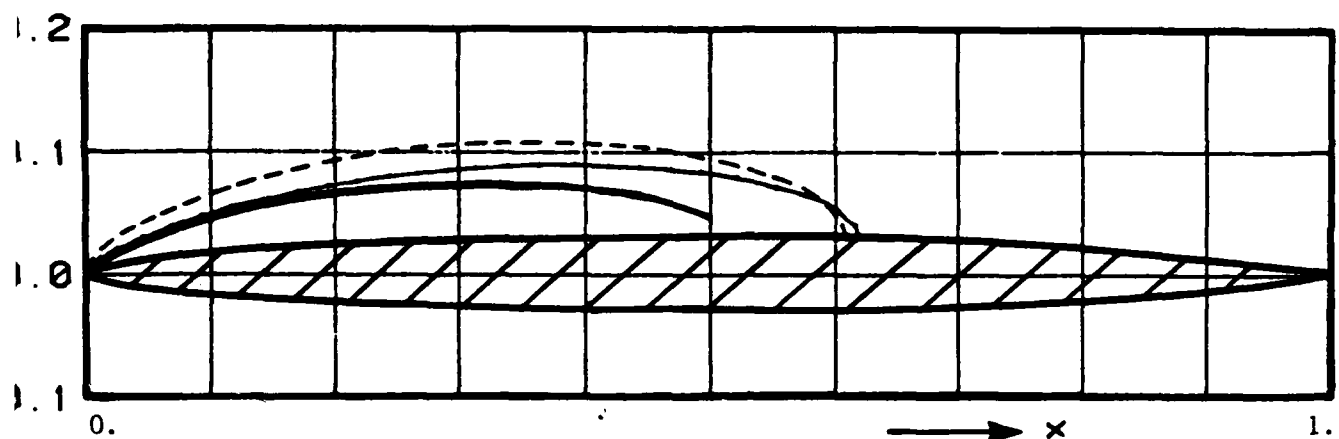


Figure 31a. Cavity plots for NACA 16-006 thickness form at $\alpha = 4^\circ$, $\sigma = 0.877$.

- Non-linear theory [38]
- - - Pure linear theory
- · - Linear theory including leading edge corrections

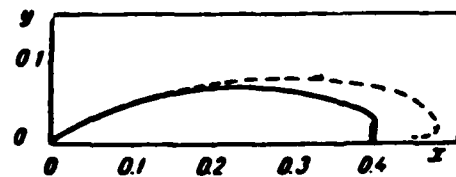


Figure 31b. Cavity plots for flat plate at $\alpha = 5^\circ$, $\sigma = 1.246$

- Non-linear theory--Riabouchinsky model [33]
- - - Non-linear theory--re-entrant jet model [23]

Riabouchinsky end plate model [33] underpredicts the extent and volume of the cavity for a flat plate, compared to the non-linear theory using the re-entrant jet model [23], as shown in Figure 31b.

23. Open cavity model

The open wake models have been developed in order to simulate better the actual flow behind the cavity and the ultimate wake defect, which is directly associated to the generated drag. A review of these models has been given by Tulin in [35].

The linearized version of the open wake models was first introduced by Fabula in [7]. According to that model, the wake has a constant thickness δ equal to the thickness of the cavity at its end, as shown in Figure 32a. The formulation of the linearized problem will be exactly the same except for the cavity closure condition which will become:

$$\delta = \int_0^l \frac{q(\xi)}{U_\infty} \cdot d\xi \quad (23.1)$$

or by using the transformation (4.3)

$$\delta = \int_0^s \frac{q(z)}{U_\infty} \cdot \frac{2 \cdot z}{(1+z^2)^2} \cdot dz \quad (23.2)$$

The cavity source $q(z)$ will still be given by (4.5), since no use of the closure condition has been made to derive it. If the change in cavitation number due to the finite thickness δ at the end of the cavity is $\Delta\sigma$, then (23.2) with (4.5), (5.3), (5.4) and (7.21) will render:

$$\Delta\sigma = - \frac{\delta}{D} \quad (23.3)$$

where D depends only on the cavity length l . Notice that $\Delta\sigma$ is

proportional to δ for a given cavity length and also that:

$$\Delta\sigma < 0 \quad (23.4)$$

The algorithm to find the cavity shape will remain exactly the same as in linear theory, after σ has been adjusted by (23.3).

Including the leading edge radius corrections, in the case an open cavity model is used, is straightforward. The resulting formulas will be the same as described in Section 21, except that σ_L must be changed by an amount given by (23.3). If the cavity starts after the leading edge of the hydrofoil, then by using the formulas developed in Appendix C, we will get:

$$\Delta\sigma = - \frac{\pi}{C_5} \cdot \delta \quad (23.5)$$

The effect of the open wake thickness δ on the cavity shape for a NACA 16-006 at $\alpha = 4^\circ$ is shown in Figure 32b. By increasing δ , the following conclusions are drawn:

- a) The cavity becomes thicker at its end and slightly thinner at its forebody.
- b) The cavity volume increases slightly for the same cavity length.
- c) The cavitation number decreases substantially.
- d) The cavity length and volume decrease substantially for the same σ .

The present theory with $\delta = 0$, is applied for some NACA 16 series Section forms and the results are shown in Appendix D, in comparison with other theories.

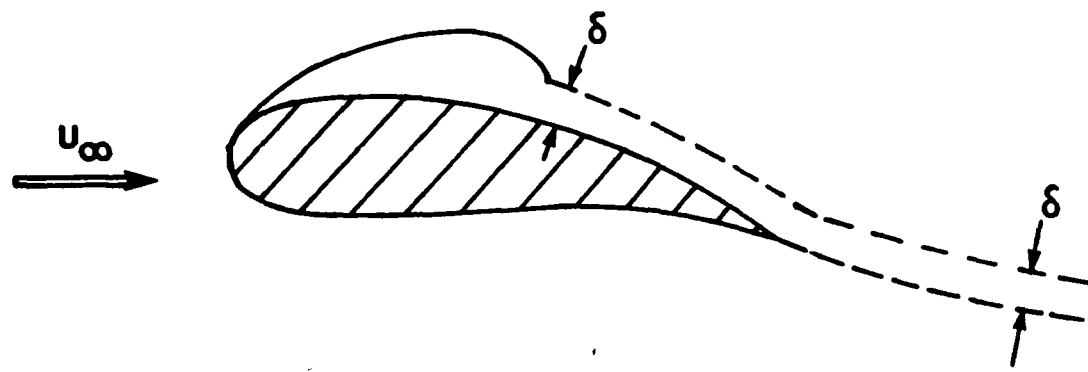


Figure 32a. Open cavity model in linear theory

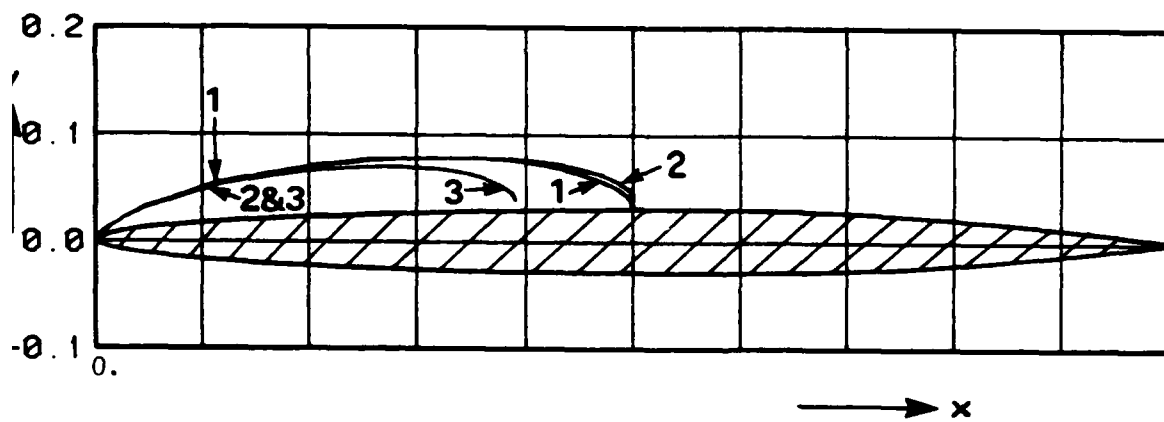


Figure 32b. Cavity plots for NACA 16-006 thickness form at $\alpha = 4^\circ$. Linear theory including leading edge corrections. Open cavity model.

	δ	I	σ
1	0.	0.5	0.939
2	0.01	0.5	0.861
3	0.01	0.39	0.939

PART D. CAVITATION EXPERIMENTS ON ROUND-NOSED HYDROFOILS

24. Purpose and description of the experiment

In section 21 we concluded that the leading edge radius plays a significant role in the partial cavitation of a hydrofoil. Namely, we found that the cavitation number σ_L resulting from pure linear theory could be corrected due to the leading edge radius, as follows:

$$\sigma = \left[\frac{1 + \frac{\sigma_L}{2}}{a(\rho_L; k)} \right]^2 - 1 \quad (21.8)$$

It would be interesting to see how well this predicts what happens in reality. The MIT Hydrodynamics Laboratory has at its disposal three round-nosed aluminum hydrofoils with identical projected area, camber distribution, and maximum thickness, but with different leading edge radii. Therefore, by testing those hydrofoils, we would be able to study solely the effect of their leading edge radii on their cavitation.

The three hydrofoils have the following main characteristics (with respect to the chord length):

No. 1: This is a NACA $a = 0.8$ meanline of $n_{max} = 0.02$ combined with a VLR thickness form [20] of $\tau_{max} = 0.04$, $\rho_L^{(1)} = 4 \times \rho_L^{(2)} = 0.002867$ and $\tau_{T.E.} = 0.004$.

No. 2: This is a NACA $a = 0.8$ meanline of $n_{max} = 0.02$ combined with a NACA 66 thickness form of $\tau_{max} = 0.04$, $\rho_L^{(2)} = 0.000717$ and $\tau_{T.E.} = 0.004$.

No. 3: This is a NACA $a = 0.8$ meanline of $n_{max} = 0.02$ combined with a VLR thickness form of $\tau_{max} = 0.04$, $\rho_L^{(3)} = 2.25 \times \rho_L^{(2)} = 0.001613$ and $\tau_{T.E.} = 0.004$.

Finally it was decided to test the hydrofoils No. 2 and No. 3.

Surfaces," Proc. London Math. Soc. 19, 2, 1921, pp. 206-215.

[33] Terentev, A. C., "Partially Cavitating Flow Around Plate"
(in Russian), Izvestia Vysshikh Uchebnykh Zavedenii Matematika 97,
6, 1970, pp. 112-118.

[34] Tulin, M. P., "Supercavitating Flow Past Foils and Struts,"
Paper No. 16, Symposium on Cavitation in Hydrodynamics, September 1955,
NPL, Teddington, England.

[35] Tulin, M. P., "Supercavitating Flows--Small Perturbation
Theory," Journal of Ship Research 7, 3, 1964, pp. 16-37.

[36] Tulin, M. P. and Hsu, C. C., "The Theory of Leading-Edge
Cavitation on Lifting Surfaces with Thickness," Symposium on
Hydrodynamics of Ship and Offshore Propulsion Systems, March 1977.

[37] Uhlman, J. S. and Jiang, C. W., "Experiments on a Partially
Cavitating Plano-Convex Hydrofoil with Comparison to Theory," M.I.T.,
Department of Ocean Engineering, Report No. 83481-2, July 1977.

[38] Uhlman, J. S., "The Surface Singularity Method Applied to
Partially Cavitating Hydrofoils," Ph.D. Thesis, M.I.T., Department of
Ocean Engineering, January 1983.

[39] Vandyke, M., Perturbation Methods in Fluid Mechanics, The
Parabolic Press, Stanford, CA, 1975.

[40] Villat, H., "Sur la validite des solutions de certain
problemes d'hydrodynamique," J. de Math. 6, 10, 1914, pp. 231-290.

[41] Wade, R. B., "Linearized Theory of a Partially Cavitating
Plano-Convex Hydrofoil Including the Effects of Camber and Thickness,"
J. Ship Research 11, 1, 1967, pp. 20-27.

[42] Wu, T. Y., "A Note on the Linear and Nonlinear Theories for
Fully Cavitated Hydrofoils," California Institute of Technology,
Hydrodynamics Laboratory Report No. 21-22, August 1956.

Documentation," MIT, Department of Ocean Engineering, Report 83-7, June 1983.

[22] Kinnas, S. A., "Cavity Shape Characteristics for Supercavitating Hydrofoils," M.I.T., Department of Ocean Engineering, Report 84-13, October 1984.

[23] Kutznetzov, A. V. and Terentev, A. C., "On Analysis of Partially Cavitating Flow Around Flat Plate" (in Russian), Izvestia Vysshikh Uchebnykh Zavedenii Matematika 66, 11, 1967, pp. 43-46.

[24] Lee, C. S., "Prediction of Steady and Unsteady Performance of Marine Propellers with or without Cavitation by Numerical Lifting Surface Theory," Ph.D. Thesis, MIT, Department of Ocean Engineering, May 1979.

[25] Lighthill, M. J., "A New Approach to Thin Aerofoil Theory," The Aeronautical Quarterly 3, November 1951, pp. 193-210.

[26] Meijer, M. C., "Some Experiments on Partly Cavitating Hydrofoils," International Shipbuilding Progress 6, 60, August 1959, pp. 361-368.

[27] Muskhelishvili, N. I., Singular Integral Equations, P. Noordhoff, Limited, Groningen, Holland, 1946.

[28] Newman, J. N., Marine Hydrodynamics, The M.I.T. Press, Cambridge, MA and London, England.

[29] Parkin, B. R., "Experiments on Circular Arc and Flat Plate Hydrofoils," J. Ship Research 1, 4, 1958, pp. 34-57.

[30] Parkin, B. R., "Munk Integrals for Fully Cavitated Hydrofoils," RAND Report P-2350-1, November 1961.

[31] Persson, B., "Theoretical Study of Cavitation on Flat Plate," DnV Technical Report 78/440.

[32] Riabouchinsky, D., "On Steady Fluid Motions with Free

August 1959, pp. 369-384.

[11] Geurst, J. A., "Linearized Theory for Fully Cavitated Hydrofoils," International Shipbuilding Progress 7, No. 65, January 1960.

[12] Geurst, J. A. and Verbrugh, P. J., "A Note on Camber Effects of a Partially Cavitated Hydrofoil," International Shipbuilding Progress 6, 61, Sep. 1959, pp. 409-414.

[13] Geurst, J. A., "Linearized Theory of Two-Dimensional Cavity Flows," Thesis, Delft Technical Institution, The Netherlands, 1961.

[14] Golden, D. W., "A Numerical Method for Two-Dimensional, Cavitating Lifting Flow," M.I.T., Department of Ocean Engineering, Report No. 81512-1, May 1975.

[15] Gradshteyn, I. S. and Ryzhik, I. M., Table of Integrals, Series, and Products, Academic Press, New York, NY, 1980.

[16] Hamaoka, T., "Linearized Theory of Cavity Flow Past a Hydrofoil of Arbitrary Shape," Ship Research Institute, Tokyo, Japan, Paper No. 21, 1967.

[17] Jiang, C. W., "Experimental and Theoretical Investigation of Unsteady Supercavitating Hydrofoils of Finite Span," Ph.D. Thesis, Department of Ocean Engineering, M.I.T., 1977.

[18] Kerwin, J. E., "Variable Pressure Water Tunnel," SNAME, New England Section Meeting, October 13, 1967.

[19] Kerwin, J. E., "A Numerical Method for the Analysis of Cavitating Propellers in a Nonuniform Flow--MIT--PUF-3. User's Manual," MIT, Department of Ocean Engineering, Report 83-6, June 1983.

[20] Kerwin, J. E., private communication.

[21] Kinnas, S. A., "A Numerical Method for the Analysis of Cavitating Propellers in a Nonuniform Flow--MIT--PUF-3 Program

REFERENCES

[1] Acosta, A. J., "A Note on Partial Cavitation of Flat Plate Hydrofoils," California Institute of Technology Hydrodynamics Laboratory Report No. E-19.9, October 1955.

[2] Arakeri, H., "Viscous Effects on the Position of Cavitation Separation from Smooth Bodies," Journal of Fluid Mechanics 68, Part 4, 1975, pp. 779-799.

[3] Birkhoff, G. and Zarantonello, E. H., Jets, Wakes and Cavities, Academic Press Inc., New York, NY, 1957.

[4] Brillouin, M., "Les surfaces de glissement de Helmholtz et la resistance des fluides," Ann. Chim. Phys. 23, 1911, pp. 145-230.

[5] Brockett, T., "Minimum Pressure Envelopes for Modified NACA-66 Sections with NACA $a = 0.8$ Camber and Bu Ships Type I and Type II Sections," DTMB Report 1780, February 1966.

[6] Efros, D. A., "Hydrodynamic Theory of Two-Dimensional Flow with Cavitation," Dokl. Akad. Nauk. SSSR 51, 1946, pp. 267-270.

[7] Fabula, A. G., "Application of Thin-Airfoil Theory to Hydrofoils with Cut-off Ventilated Trailing Edge," Navweps Report 7571 NOTS TP 2547, U. S. Naval Ordnance Test Station, China Lake, CA, September 13, 1960.

[8] Fabula, A. G., "Thin-Airfoil Theory Applied to Hydrofoils with a Single Finite Cavity and Arbitrary Free-Streamline Detachment," Journal of Fluid Mechanics 12, 1962, pp. 227-240.

[9] Geurst, J. A. and Timman, R., "Linearized Theory of Two-Dimensional Cavitational Flow Around a Wing Section," IX International Congress of Applied Mechanics, 1956.

[10] Geurst, J. A., "Linearized Theory for Partially Cavitated Hydrofoils," International Shipbuilding Progress 6, 60,

(n) The reduction in the cavity size by increasing the leading edge radius of the hydrofoil has also been confirmed from the experiments conducted at the MIT water tunnel.

RECOMMENDATIONS

The conclusions of the thesis suggest the following directions for further research:

- a) To investigate the effect of the leading edge radius on the load distribution and the hydrodynamic coefficients of a cavitating hydrofoil.
- b) To apply the leading edge corrections to supercavitating round-nosed hydrofoils. In this case, the corrections are expected to have less impact on pure linear theory.
- c) To conduct more experiments on round-nosed hydrofoils, preferably of thick leading edge radii, and to compare the measured values of the cavitation numbers for different cavity lengths with the ones predicted by the proposed theory. When applying the theory, the wall tunnel effects should be properly taken into account. The values of an equivalent open cavity thickness that would make the present theory fit the experiment should be found, and their correlation to the main variables of the problem should be investigated.
- d) To apply the leading edge corrections to the cavitating propeller problem by incorporating a local Lighthill's correction at each spanwise position on the leading edge of the blade. This is expected to have an insignificant effect on the computing time of the existing code.

supercavitating hydrofoils at moderate angles of attack.

(g) Linear theory has been shown to overpredict substantially the extent and volume of the cavity for partially cavitating round-nosed hydrofoils.

(i) The leading edge radius of the hydrofoil has been introduced by incorporating Lighthill's correction in the linearized formulation of the problem. This led to the introduction of a virtual cavitation number varying over the cavity length and, in particular, square root singular at the leading edge of the hydrofoil. The implementation of the leading edge radius corrections into our computer code for partially cavitating hydrofoils was trivial and had no significant effect on the computing time.

(j) The effect of the leading edge radius on the partial cavitation of a hydrofoil has been found to be significant. In particular, it was shown that by increasing the leading edge radius of a hydrofoil, the extent and volume of the cavity decreased, for fixed flow conditions.

(k) The effect of the location of the cavity detachment point, when the leading edge radius corrections were included, has been found to be negligible for long cavities. However, by starting the cavity at the minimum pressure point we predicted the right cavitation inception number.

(l) The effect of the cavity termination model on the cavity extent and volume has been found to be significant.

(m) The present theory, compared with the non-linear theory by Uhlman, has been found to overpredict the effect of leading edge radius on the cavity size, but not as much as the short cavity theory by Tulin and Hsu.

CONCLUSIONS

The following have been accomplished during the evolution of this thesis:

(a) The linearized theory for the partial and the supercavitating hydrofoil problem has been stated in a uniform way in terms of integral equations of unknown source and vortex distributions on the foil and on the cavity.

(b) The general problem for partial and supercavitating hydrofoils has been decomposed into three elementary problems, one of camber, one of thickness and one of angle of attack. This has enabled us to study separately the effect of camber and thickness on the cavitation of hydrofoils.

(c) The general solution of the linear partially cavitating hydrofoil problem for a given cavity length has been shown to depend only on the distribution over that length of the non-cavitating streamwise perturbation velocity u_w^+ on the upper hydrofoil surface. Expressions for the cavitation number, the cavity volume and the cavity source distribution have been given in terms of integrals of u_w^+ .

(d) For the supercavitating hydrofoil problem, expressions for the cavitation number, the cavity volume and the cavity source distribution are given in terms of integrals of the slope of the wetted hydrofoil surface.

(e) Very accurate and efficient computer codes have been developed for the application of linear theory in partial and supercavitating hydrofoils.

(f) Linear theory has been shown to be accurate for sharp-nosed

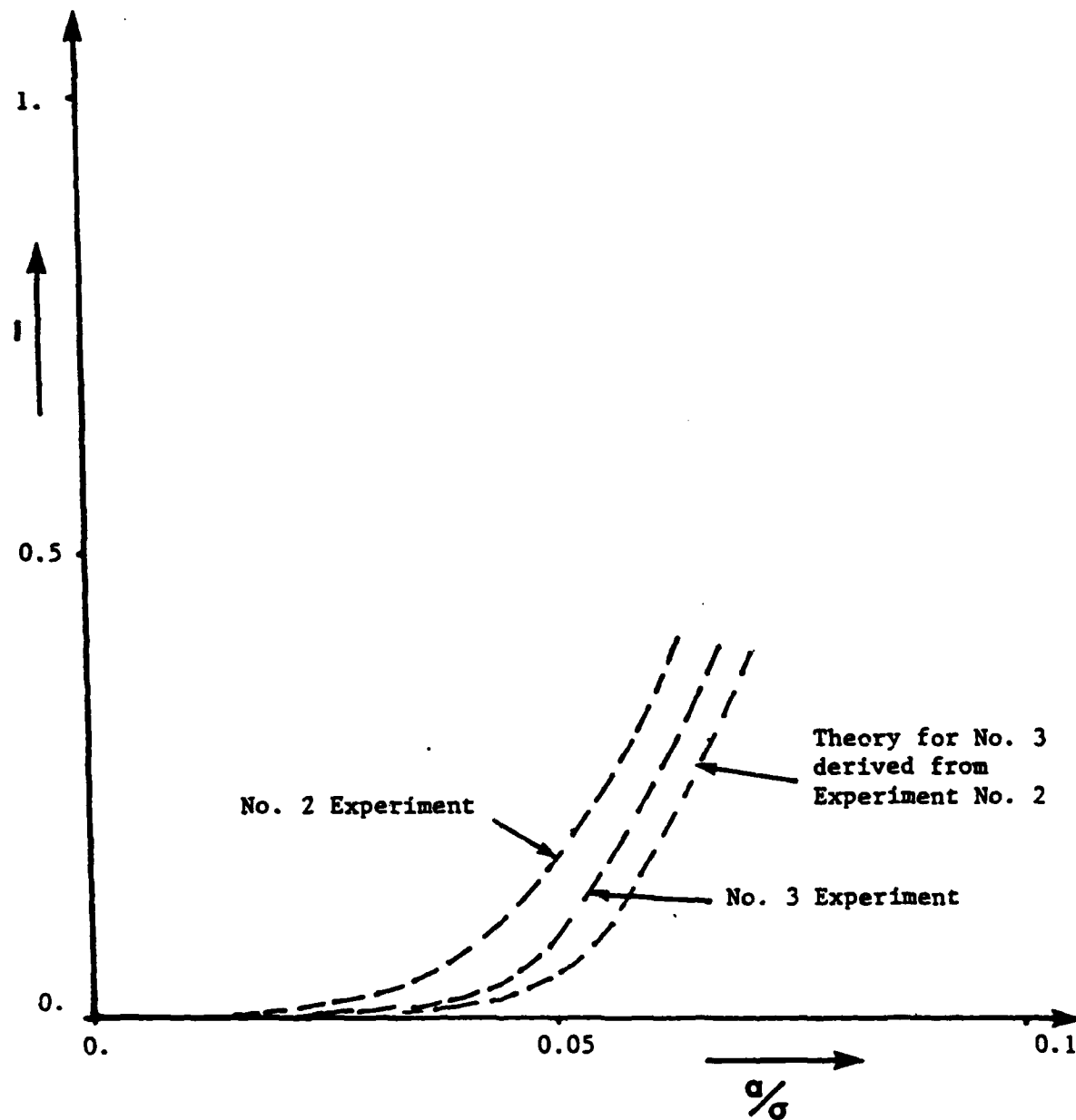


Figure 34. l vs. a/σ for the two tested hydrofoils at the MIT watertunnel - $\alpha = 2.7^\circ$.

ℓ	Measured σ	$\sqrt{1+\sigma}$	$q_s(3)$	Actual σ
0.	2.45	--	--	--
0.1	1.14	1.46	1.39	0.93
0.2	0.96	1.4	1.35	0.82
0.3	0.86	1.36	1.32	0.74
0.4	0.83	1.35	1.3	0.69

Table 12. Experimental results for foil No. 3

ℓ	Measured σ	$\sqrt{1+\sigma}$	$q_s(2)$	Actual σ
0.	2.944	--	--	--
0.1	1.262	1.50	1.43	1.045
0.2	1.047	1.43	1.38	0.905
0.3	0.956	1.40	1.34	0.795
0.4	0.91	1.38	1.32	0.75

Table 13. Experimental results for foil No. 2

actual leading edge radii or by testing hydrofoil No. 3 which has a larger leading edge radius and therefore is less vulnerable to machining imperfections.

changed from 3. degrees to 2.7 degrees, due to the angular deflection of the hydrofoils around their hinges, produced by the developed loading during the experiments. The reduction in the cavity extent due to the increase in the leading edge radius, for fixed α/σ , is significant especially for short cavities. A similar reduction in cavity volume is expected but the actual curves are not shown, since it is difficult to measure the cavity volume.

If $\sigma^{(2)}$ and $\sigma^{(3)}$ are the cavitation numbers predicted by the present theory for the two hydrofoils, then at a given cavity length the following relationship will hold:

$$\frac{\sqrt{1+\sigma^{(3)}}}{\sqrt{1+\sigma^{(2)}}} = \frac{a^{(2)}}{a^{(3)}} \quad (25.1)$$

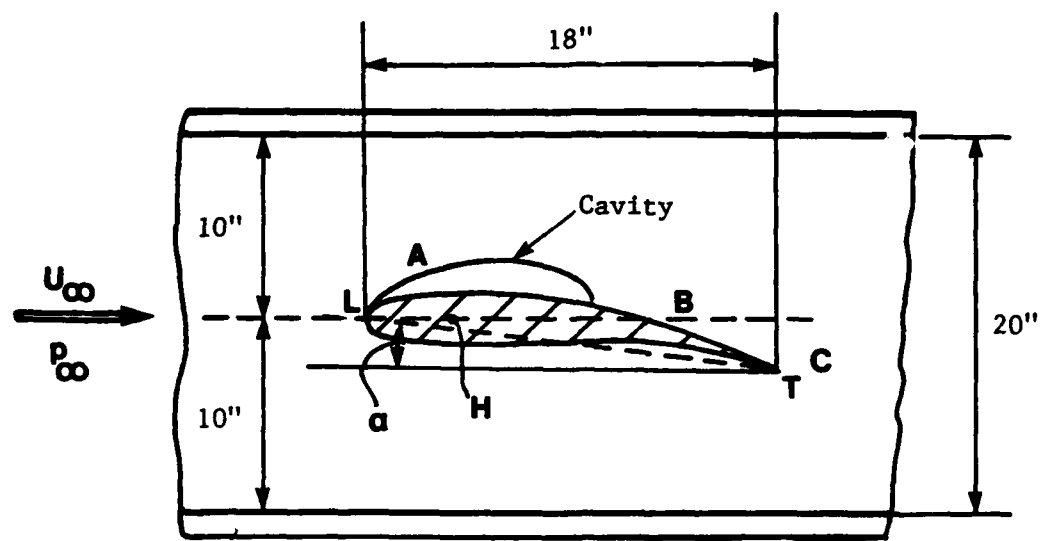
where $a^{(3)}$ and $a^{(2)}$ are the correction factors corresponding to $\rho_L^{(3)}$ and $\rho_L^{(2)}$ respectively, at the given cavity length. Equation (25.1) was derived from (21.8) under the assumption that $\sigma_L^{(2)} = \sigma_L^{(3)}$ which is true since the two hydrofoils are identical except for their leading edge radii, which do not affect the linear solution anyway. In order to compare the present theory with the experiments we evaluated $\sigma^{(3)}$ from (25.1) by using the experimental values of $\sigma^{(2)}$. The respective ℓ vs. α/σ curve is also shown in Figure 34. We observe that the present theory overpredicts the reduction in the cavity extent, for fixed α/σ . This may be attributed to any differences of the actual leading edge radii from the designed ones due to machining imperfections, especially for hydrofoil No. 2 which has the smaller leading edge radius. This could be verified by either measuring the

25. Comparison of the measurements to theory

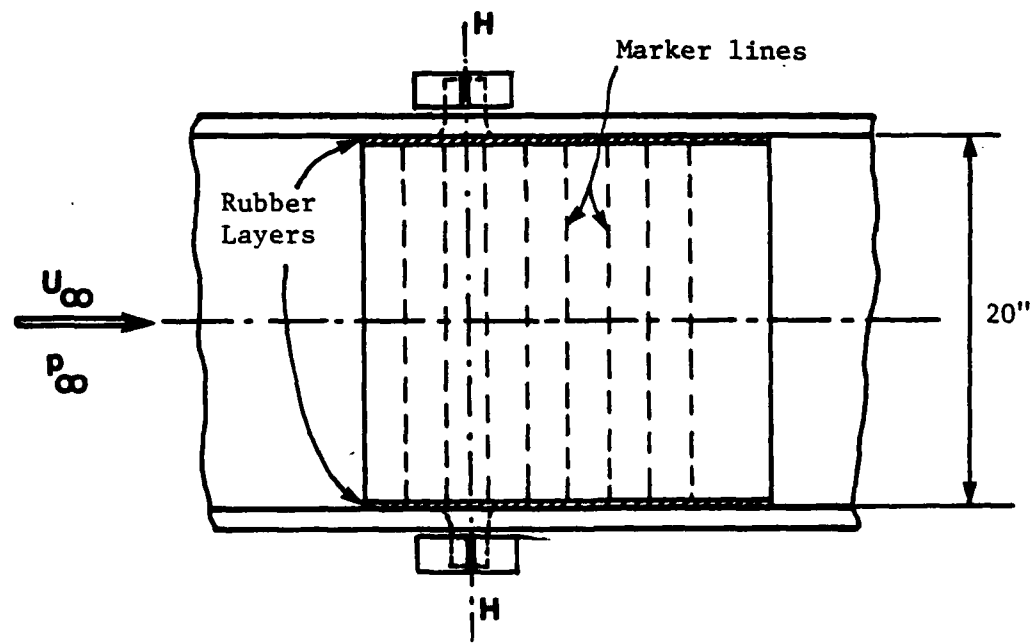
The cavitation number for each cavity length is evaluated by substituting in formula (2.1) the recorded values for $p_{\infty} - p_c$ and U_{∞} . The resulting numbers for the two tested hydrofoils, designated as measured σ 's, are shown in Tables 12 and 13. The corresponding values at $\lambda = 0$ are the cavitation inception numbers.

We have also been able to measure the flowfield velocity on the cavity surface, using the laser Doppler anemometer installed at the MIT water tunnel, operating in forward scatter mode. In fact, by approaching the cavity with the laser beams from above, we recorded the measured velocity just before the signal was lost by the tracker, indicating that the beams entered the cavity. The measured cavity velocities were found to be independent of the spanwise or chordwise location on the cavity. Their values relative to the freestream velocity are shown at the fourth column of Tables 12 and 13. We observe that they are smaller than the values of $\sqrt{1 + \sigma}$ based on the measured σ , also shown at the third column of the same Tables. The values of the cavitation numbers which would predict the same cavity velocities as the measured ones, designated as actual σ 's, are also shown. The difference of the measured from the actual cavitation number varies slightly with the cavity length and finally is attributed either to the entrapped air inside the cavity, or to calibration errors of the manometers. For any comparisons between experiments and theory the actual cavitation numbers should be used.

In Figure 34 the λ vs. a / σ curves are shown for the two experiments. The actual angle of attack was measured and was found



(a) Side view



(b) Plan view

Figure 33. Hydrofoil mounted in the MIT water tunnel

The hydrofoils were put in the twenty by twenty inches test section of the MIT variable pressure water tunnel [18], as shown schematically in Figure 33. They were mounted from their hinges H on specially provided holes on the vertical windows of the water tunnel. The angle of attack was set equal to 3 degrees for both tests, by rotating and then locking the hinges via devices mounted on the outer surface of the windows. Thin rubber layers were placed in between the tips of the hydrofoils and the inner surfaces of the vertical windows to prevent any cross flow due to the pressure differences between the lower and the upper surfaces of the hydrofoil. Marker lines were drawn on the upper surface of the hydrofoil in order to facilitate the cavity length readings.

During both tests the flow velocity has been kept constant around 19.5 ft/sec. By changing p_{∞} , we changed the cavitation number σ and therefore the size of the cavity. The following observations were made:

- a) The cavities appeared very two-dimensional.
- b) The end of the cavity was oscillating around some mean position. The longer the cavity, the bigger the oscillations. Cavities longer than 60% of the chord fell quickly into the 3/4 chord instability regime in which the cavity was moving violently back and forth.
- c) The cavity surface at its beginning was smooth and transparent, becoming rough and opaque towards the end, followed by a wake of similar structure.

[43] Wu, T. Y., "A Simple Method for Calculating the Drag in the Linear Theory of Cavity Flows," California Institute of Technology, Report No. 85-5, August 1957.

APPENDIX A

List of Integrals

In this appendix, a list of integrals used throughout our analysis is given, along with some instructions for their derivation.

The first integrals (A.1)-(A.7) have been evaluated by using the transformation:

$$x = l \cdot \sin^2\left(\frac{\theta}{2}\right) \text{ or } z = t \cdot \sin^2\left(\frac{\theta}{2}\right), \text{ where } 0 \leq \theta \leq \pi$$

$$\int_0^l \sqrt{\frac{x}{l-x}} \cdot dx = \frac{\pi \cdot l}{2} \quad (\text{A.1})$$

$$\int_0^l x \cdot \sqrt{\frac{x}{l-x}} \cdot dx = \frac{3\pi \cdot l^2}{8} \quad (\text{A.2})$$

$$\int_0^l x \cdot \sqrt{\frac{x}{l-x}} \cdot \frac{1}{x-\xi} \cdot dx = \pi \cdot \left(\xi + \frac{l}{2}\right); \quad 0 \leq \xi \leq l \quad (\text{A.3})$$

$$\begin{aligned} \int_0^t \sqrt{\frac{z}{t-z}} \cdot \frac{1}{n-z} \cdot dz &= -\pi; \quad 0 \leq n \leq t \\ &= \pi \cdot \sqrt{\frac{n}{n-t}} - \pi; \quad n > t \end{aligned} \quad (\text{A.4})$$

$$\begin{aligned} \int_0^t \sqrt{\frac{t-z}{z}} \cdot \frac{1}{n-z} \cdot dz &= \pi; \quad 0 \leq n \leq t \\ &= \pi - \pi \cdot \sqrt{\frac{n-t}{n}}; \quad n > t \end{aligned} \quad (\text{A.5})$$

$$\int_0^t \sqrt{\frac{z}{t-z}} \cdot \frac{1}{n+z} \cdot dz = \pi - \pi \cdot \sqrt{\frac{n}{n+t}} \quad (\text{A.6})$$

$$\int_0^t \sqrt{\frac{t-z}{z}} \cdot \frac{1}{n+z} \cdot dz = \pi \cdot \sqrt{\frac{n+t}{n}} - \pi \quad (\text{A.7})$$

The next integrals (A.8)-(A.18) have been taken from [31] where they have been evaluated by straightforward application of the calculus of

residues:

$$\int_0^s \sqrt{\frac{z}{s-z}} \cdot \frac{1}{1+z^2} \cdot dz = \frac{\pi}{\sqrt{2}} \cdot \frac{\sqrt{r^2-1}}{r^2} \quad (\text{A.8})$$

$$\int_0^s \sqrt{\frac{z}{s-z}} \cdot \frac{z}{1+z^2} \cdot dz = \pi - \frac{\pi}{\sqrt{2}} \cdot \frac{\sqrt{r^2+1}}{r^2} \quad (\text{A.9})$$

$$\int_0^s \sqrt{\frac{z}{s-z}} \cdot \frac{z^2}{1+z^2} \cdot dz = \frac{\pi \cdot s}{2} - \frac{\pi}{\sqrt{2}} \cdot \frac{\sqrt{r^2-1}}{r^2} \quad (\text{A.10})$$

$$\int_0^s \sqrt{\frac{z}{s-z}} \cdot \frac{1}{(1+z^2)^2} \cdot dz = \frac{\pi}{4\sqrt{2}} \cdot \frac{s \cdot (s^2+3) \cdot \sqrt{r^2+1} - 2 \cdot \sqrt{r^2-1}}{r^8} \quad (\text{A.11})$$

$$\int_0^s \sqrt{\frac{z}{s-z}} \cdot \frac{z}{(1+z^2)^2} \cdot dz = \frac{\pi}{4\sqrt{2}} \cdot \frac{2 \cdot s^2 \cdot \sqrt{r^2+1} + s \cdot (s^2-1) \cdot \sqrt{r^2-1}}{r^8} \quad (\text{A.12})$$

$$\int_0^s \sqrt{\frac{z}{s-z}} \cdot \frac{z^2}{(1+z^2)^2} \cdot dz = \frac{\pi}{4\sqrt{2}} \cdot \frac{s \cdot (3 \cdot s^2+1) \cdot \sqrt{r^2+1} - (4 \cdot s^2+2) \cdot \sqrt{r^2-1}}{r^8} \quad (\text{A.13})$$

$$\int_0^s \sqrt{\frac{s-z}{z}} \cdot \frac{1}{1+z^2} \cdot dz = \frac{\pi}{\sqrt{2}} \cdot \sqrt{r^2-1} \quad (\text{A.14})$$

$$\int_0^s \sqrt{\frac{s-z}{z}} \cdot \frac{z}{1+z^2} \cdot dz = \frac{\pi}{\sqrt{2}} \cdot \sqrt{r^2+1} - \pi \quad (\text{A.15})$$

$$\int_0^s \sqrt{\frac{s-z}{z}} \cdot \frac{z^2}{1+z^2} \cdot dz = \frac{\pi \cdot s}{2} - \frac{\pi}{\sqrt{2}} \cdot \sqrt{r^2-1} \quad (\text{A.16})$$

$$\int_0^s \sqrt{\frac{s-z}{z}} \cdot \frac{1}{(1+z^2)^2} \cdot dz = \frac{\pi}{4\sqrt{2}} \cdot \frac{s \cdot \sqrt{r^2+1} + (3 \cdot s^2+2) \cdot \sqrt{r^2-1}}{r^4} \quad (\text{A.17})$$

$$\int_0^s \sqrt{\frac{s-z}{z}} \cdot \frac{z}{(1+z^2)^2} \cdot dz = \frac{\pi}{4\sqrt{2}} \cdot \frac{s \cdot \sqrt{r^2-1}}{r^2} \quad (\text{A.18})$$

The next integrals have been evaluated by breaking the integrand into partial fractions and then by applying the formulas (A.1) to (A.18):

$$\int_0^s \sqrt{\frac{s-\eta}{\eta}} \cdot \frac{\eta}{(1+\eta^2) \cdot (z-\eta)} d\eta = -2\pi \cdot \frac{(A-B.z)}{(1+z^2)} \quad (\text{A.19})$$

with: $A = \frac{1}{2\sqrt{2}} \cdot \sqrt{r^2 - 1}$ and $B = \frac{1}{2\sqrt{2}} \cdot \sqrt{r^2 + 1}$

$$I(\eta; s) = \int_0^s \sqrt{\frac{z}{s-z}} \cdot \frac{1}{1+z^2} \cdot \frac{1}{z-\eta} \cdot dz = \\ = \frac{\pi}{\sqrt{2 \cdot r^2 \cdot (1+\eta^2)}} \cdot [\sqrt{r^2+1} - \eta \cdot \sqrt{r^2-1}] \quad (A.20)$$

$$\int_0^s \sqrt{\frac{z}{s-z}} \cdot \frac{1}{(1+z^2)^2 \cdot (z-\eta)} \cdot dz = \\ = \frac{\pi}{\sqrt{2 \cdot r^2}} \cdot \frac{1}{(1+\eta^2)^2} \cdot [\sqrt{1+r^2} - \eta \cdot \sqrt{r^2-1}] - \frac{\pi}{4 \cdot \sqrt{2 \cdot r^8}} \cdot \frac{1}{1+\eta^2} \cdot [E+n.F] \quad (A.21)$$

with

$$E = 2.s^2 \cdot \sqrt{r^2+1} + (s^3-s) \cdot \sqrt{r^2-1}$$

and $F = (s^3+3.s) \cdot \sqrt{r^2+1} - 2 \cdot \sqrt{r^2-1}$

$$\int_0^t \sqrt{\frac{t-z}{z}} \cdot \frac{1}{1+z^2} \cdot \frac{1}{z-\eta} \cdot dz = - \frac{\pi}{\sqrt{2 \cdot (1+\eta^2)}} \cdot (\sqrt{r^2+1} + \eta \cdot \sqrt{r^2-1}) \quad (A.22)$$

$$J(\eta; t) = \int_0^t \frac{z^2}{(1+z^2)^2} \cdot \sqrt{\frac{t-z}{z}} \cdot \frac{1}{z-\eta} \cdot dz = \\ = \frac{\pi}{\sqrt{2 \cdot r^2}} \cdot \frac{1}{(1+\eta^2)} \cdot \left[\frac{\eta \cdot (t-\eta)}{(1+\eta^2)} \cdot \{ \sqrt{r^2+1} - \eta \cdot \sqrt{r^2-1} \} - \right. \\ \left. - \frac{(1+\eta \cdot t)}{4 \cdot r^6} \cdot \{ 2 \cdot t^2 \cdot \sqrt{r^2+1} + t \cdot (t^2-1) \cdot \sqrt{r^2-1} \} + \right. \\ \left. + \frac{(t-\eta)}{4 \cdot r^6} \cdot \{ t \cdot (t^2+3) \cdot \sqrt{r^2+1} - 2 \cdot \sqrt{r^2-1} \} \right] \quad (A.23)$$

$$R(\omega, z) \stackrel{\text{DEF}}{=} \int_0^t \sqrt{\frac{t-\eta}{\eta}} \cdot \frac{1}{z^2-\eta^2} \cdot \frac{1}{\eta-\omega} \cdot d\eta \quad (A.24a)$$

$$R(\omega, z) = - \frac{\pi}{2 \cdot z \cdot (z+\omega)} \cdot \sqrt{\frac{t+z}{z}} \quad ; \quad 0 \leq z \leq t \quad (A.24b)$$

$$R(\omega, z) = - \frac{\pi}{2 \cdot z \cdot (z+\omega)} \cdot \sqrt{\frac{t+z}{z}} - \frac{\pi}{2 \cdot z \cdot (z-\omega)} \cdot \sqrt{\frac{z-t}{z}} ; \quad z > t \quad (\text{A.24c})$$

$$\begin{aligned} \int_0^t \sqrt{\frac{\omega}{t-\omega}} \cdot \frac{1}{1+\omega^2} \cdot \frac{\omega}{z+\omega} \cdot d\omega = \\ = - \frac{1}{1+z^2} \cdot \frac{\pi}{\sqrt{2 \cdot r^2}} \cdot [\sqrt{r^2-1} - z \cdot \sqrt{r^2+1}] + \pi \cdot \sqrt{\frac{z}{z+t}} \cdot \frac{z}{1+z^2} \quad (\text{A.25}) \end{aligned}$$

$$\begin{aligned} \int_0^t \sqrt{\frac{\omega}{t-\omega}} \cdot \frac{1}{1+\omega^2} \cdot \frac{\omega}{z-\omega} \cdot d\omega = \\ = - \frac{1}{1+z^2} \cdot \frac{\pi}{\sqrt{2 \cdot r^2}} \cdot [\sqrt{r^2+1} \cdot z + \sqrt{r^2-1}] + \pi \cdot \sqrt{\frac{z}{z-t}} \cdot \frac{z}{1+z^2} \quad (\text{A.26}) \\ z > t \end{aligned}$$

$$\begin{aligned} \int_0^t \int_a^b \sqrt{\frac{t-\eta}{\eta}} \cdot \frac{\eta}{(z^2 - \eta^2) \cdot (\eta - \omega)} \cdot d\eta = \\ = \frac{\pi}{2} \cdot [\frac{1}{z+\omega} \cdot \sqrt{\frac{t+z}{z}} - \frac{1}{z-\omega} \cdot \sqrt{\frac{z-t}{z}}] ; \quad z > t \quad (\text{A.27}) \end{aligned}$$

Whenever we have to change the order of integration in a double singular integral, we use the Poincaré-Bertrand formula [27]:

$$\begin{aligned} \int_a^b \int_a^b \frac{dt}{t-t_0} \cdot \int_a^b \frac{\phi(t, t_1)}{t_1-t} \cdot dt_1 = \\ = - \pi^2 \cdot \phi(t_0, t_0) + \int_a^b dt_1 \int_a^b \frac{\phi(t, t_1)}{(t-t_0) \cdot (t_1-t)} \cdot dt \quad (\text{A.28}) \end{aligned}$$

APPENDIX B

Leading edge radius for cavitating hydrofoils

The point where the cavity starts for the case of round-nosed hydrofoils can be determined in non-linear theory by the Villat-Brillouin condition [4, 40], according to which the curvature of the cavity and foil should be continuous at that point. Some semi-empirical criteria to take into account viscous effects can also be used [2]. For the case of sharp-nosed hydrofoils, the cavity will start from the leading edge tangent to the lower hydrofoil surface, going ahead of the foil for a short distance and then turning back towards the trailing edge of the hydrofoil.

In the linear theory described in Parts A and B of this thesis, we assume that the cavity starts at the leading edge of the hydrofoil for either sharp- or round-nosed hydrofoils. In both cases the asymptotic behavior of $q(x)$ as $x \rightarrow 0$ can be found by using (4.5) and (4.3) as:

$$q(x) \sim \frac{(\text{const})}{x^{1/2}} \quad \text{as } x \rightarrow 0 \quad (\text{B-1})$$

which by using (2.19) will give:

$$\frac{dh}{dx} \sim \frac{(\text{const})}{x^{1/2}} \quad \text{as } x \rightarrow 0 \quad (\text{B-2})$$

For round-nosed hydrofoils the slope of the upper surface behaves like:

$$\frac{d\bar{n}_u}{dx} \sim \sqrt{\frac{\rho_L}{2}} \cdot \frac{1}{x^{1/2}} \quad \text{as } x \rightarrow 0 \quad (\text{B-3})$$

where ρ_L is the leading edge radius of the hydrofoil. But the cavity surface $\bar{n}_c(x)$ can be expressed as:

$$\bar{n}_c(x) = \bar{n}_u(x) + h(x); \quad 0 < x < l \quad (\text{B-4})$$

and the slope of the cavity surface will be given as the sum of the foil and the cavity thickness slopes:

$$\frac{d\bar{n}_c}{dx} = \frac{d\bar{n}_u}{dx} + \frac{dh}{dx} \quad (B-5)$$

The asymptotic behavior of $\frac{\partial \bar{n}_c}{\partial x}$ will be:

$$\frac{d\bar{n}_c}{dx} \sim \frac{d\bar{n}_u}{dx} \sim \sqrt{\frac{\rho_L}{2}} \cdot \frac{1}{x^2} \quad (B-6)$$

since the second term in the RHS of (B-5) is subdominant according to (B-2) and (B-3). Therefore the slope of the cavity is the same as the slope of the hydrofoil at the point where the cavity starts. Similarly we may conclude that the radius of the curvature of the cavity surface at its start is ρ_L , the same as the curvature of the hydrofoil at that point.

For supercavitating round-nosed hydrofoils, if the cavity starts at the leading edge of the hydrofoil, then the formula (16.1a) will render [22]:

$$\bar{q}(z) \sim -2\theta^*(z) \text{ as } z \rightarrow 0 \quad (B-7)$$

which also means that the cavity has the same leading edge radius as the hydrofoil.

When the leading edge corrections are included, again the leading edge radius remains the same as that of the foil, since the cavity source distribution will have again a fourth root singularity at the leading edge, as can be concluded from Section 21.

APPENDIX C

Formulas used in Section 22

The cavity source distribution in the case the cavity starts at $\ell_0 > 0$ has been given in Section 22 as follows:

$$q(z) = \frac{1}{\pi} \cdot \frac{(1+z^2)}{z} \cdot \sqrt{\frac{z-s_0}{s-z}} \cdot \int_{s_0}^s \sqrt{\frac{s-\eta}{\eta-s_0}} \cdot \frac{\eta}{1+\eta^2} \cdot \frac{1}{z-\eta} \cdot \left(u_w^+ - \frac{\sigma \cdot U_\infty}{2} \right) \cdot d\eta \quad (22.12)$$

for $s_0 < z < s$

$$\text{where: } s_0 = \sqrt{\frac{\ell_0}{1-\ell_0}} \quad (22.13)$$

The cavitation number σ is going to be determined from the cavity closure condition (22.9), which in terms of z will become:

$$\int_{s_0}^s q(z) \cdot \frac{2 \cdot z \cdot dz}{(1+z^2)^2} = 0 \quad (C-1)$$

Substituting (22.12) in (C-1) and using (A.28) we get:

$$\int_{s_0}^s d\eta \cdot \frac{\eta}{1+\eta^2} \cdot \sqrt{\frac{s-\eta}{\eta-s_0}} \cdot \bar{I}(\eta; s, s_0) \cdot \left(u_w^+ - \frac{\sigma \cdot U_\infty}{2} \right) \cdot d\eta = 0 \quad (C-2)$$

$$\text{where: } \bar{I}(\eta; s, s_0) \stackrel{\text{DEF}}{=} \int_{s_0}^s \frac{1}{1+z^2} \cdot \sqrt{\frac{z-s_0}{s-z}} \cdot \frac{dz}{z-\eta} \quad (C-3)$$

The integral $\bar{I}(\eta; s, s_0)$ is identical to $I(\eta; s)$ defined in (5.7), for $s_0 = 0$. It can also be expressed as:

$$\bar{I}(\eta; s, s_0) = \frac{(\pi-C_3)-C_4 \cdot \eta}{1 + \eta^2} \quad (C-4)$$

where C_3, C_4 are constants depending on s, s_0 and defined as:

$$C_3 = \int_{s_0}^s \sqrt{\frac{z-s_0}{s-z}} \cdot \frac{z}{1+z^2} \cdot dz \quad (C-5)$$

$$C_4 = \int_{s_0}^s \sqrt{\frac{z-s_0}{s-z}} \cdot \frac{1}{1+z^2} \cdot dz \quad (C-6)$$

If we also define:

$$C_5 = \int_{s_0}^s \frac{n}{(1+n^2)^2} \cdot \sqrt{\frac{s-n}{n-s_0}} \cdot [(\pi - C_3) - C_4 \cdot n] \cdot dn \quad (C-7)$$

then we find from (C-2) the following expression for σ :

$$\sigma = \int_{s_0}^s \frac{2 \cdot u_w^+(n)}{U_w} \cdot \bar{f}(n; s, s_0) \cdot dn \quad (22.14)$$

where:

$$\bar{f}(n; s, s_0) = \frac{n}{(1+n^2)^2} \cdot \sqrt{\frac{s-n}{n-s_0}} \cdot \left[\frac{\pi - C_3}{C_5} - \frac{C_4}{C_5} \cdot n \right] \quad (22.15)$$

The cavity source distribution $q(z)$ can also be put in the following form, starting from (22.12):

$$q(z) = -\frac{1}{\pi} \cdot \frac{1+z^2}{z} \cdot \sqrt{\frac{z-s_0}{s-z}} \cdot \int_{s_0}^s \sqrt{\frac{s-n}{n-s_0}} \cdot \frac{n}{1+n^2} \cdot \frac{u_w^+(z) - u_w^+(n)}{z-n} \cdot dn + \\ + [\sigma \cdot U_w - 2 \cdot u_w^+(z)] \cdot \frac{1}{z} \cdot \sqrt{\frac{z-s_0}{s-z}} \cdot \left[\frac{C_2}{2} - \frac{C_1 + \pi}{2} \cdot z \right] \quad (22.17)$$

where the constants C_1 and C_2 are defined as:

$$C_1 = \int_{s_0}^s \sqrt{\frac{s-n}{n-s_0}} \cdot \frac{n}{1+n^2} \cdot dn \quad (C-8)$$

$$C_2 = \int_{s_0}^s \sqrt{\frac{s-n}{n-s_0}} \cdot \frac{1}{1+n^2} \cdot dn \quad (C-9)$$

The constants C_1 , C_2 , C_3 , C_4 for $s_0 = 0$ reduce to the constants defined by the expressions (A.15), (A.14), (A.9), (A.8).

Similarly $C_5 \rightarrow D \cdot \pi$ as $s_0 \rightarrow 0$. Analytical expressions for C_1 , C_2 , C_3 , C_4 , C_5 as functions of s and s_0 can be found through a cumbersome application of the calculus of residues. Instead we perform the integrations involved in their definitions numerically

after making the transformation (22.18).

APPENDIX D

Characteristic curves and cavity plots for NACA 16 thickness forms

The computer codes developed for the application of the theory described in Parts A and C of the thesis have been run for symmetrical NACA 16 sections with thickness/chord ratios of 6%, 9%, and 12%, at an angle of attack $\alpha = 4^\circ$. The input ℓ_0 and ρ_L values, in the case the leading edge corrections are included, are shown in Table D1. The values for ℓ_0 correspond to x_{\min} and they have been evaluated by using (20.3). The results have been found to be as accurate and convergent as stated in Section 8. The required CPU time has been negligible.

The characteristic curves as given by pure linear theory, linear theory including leading edge corrections, non-linear theory [38], and short cavity theory [36] are shown in Figures D1-D10. The following conclusions can be drawn:

- a) Pure linear theory predicts that as the foil thickness increases, the cavity length and volume also increase for fixed flow conditions.
- b) Linear theory, including the leading edge corrections, non-linear theory and short cavity theory, all predict that by increasing the foil thickness, the cavity length and volume decrease for fixed flow conditions. The reduction in cavity volume as predicted by the present theory is higher than that predicted by Uhlman [38], but not as high as that by Tulin and Hsu [36].
- c) Comparing Figure D5 with D6, we observe that for fixed cavity length, the present theory predicts a slightly higher cavity volume than the non-linear theory. Comparing also Figures D2 with D3, we conclude that it is the difference between the corresponding cavitation

numbers which makes the two theories different. By adjusting the thickness of the cavity at its trailing edge, as described in Section 23, we could very well make the two theories produce equivalent results. However, since the cavity termination model in non-linear theory is not necessarily physically correct, it is still necessary to make use of experimental results to judge which theory is better.

Finally, some cavity plots for the three NACA sections, as predicted by linear theory including leading edge corrections, are shown in Figures D11-D13.

NACA	I_o	ρ_L
16-006	0.00018	0.00176
16-009	0.00097	0.00396
16-012	0.00325	0.00703

Table D1. Input data for the NACA 16 thickness forms at $\alpha = 4^{\circ}$

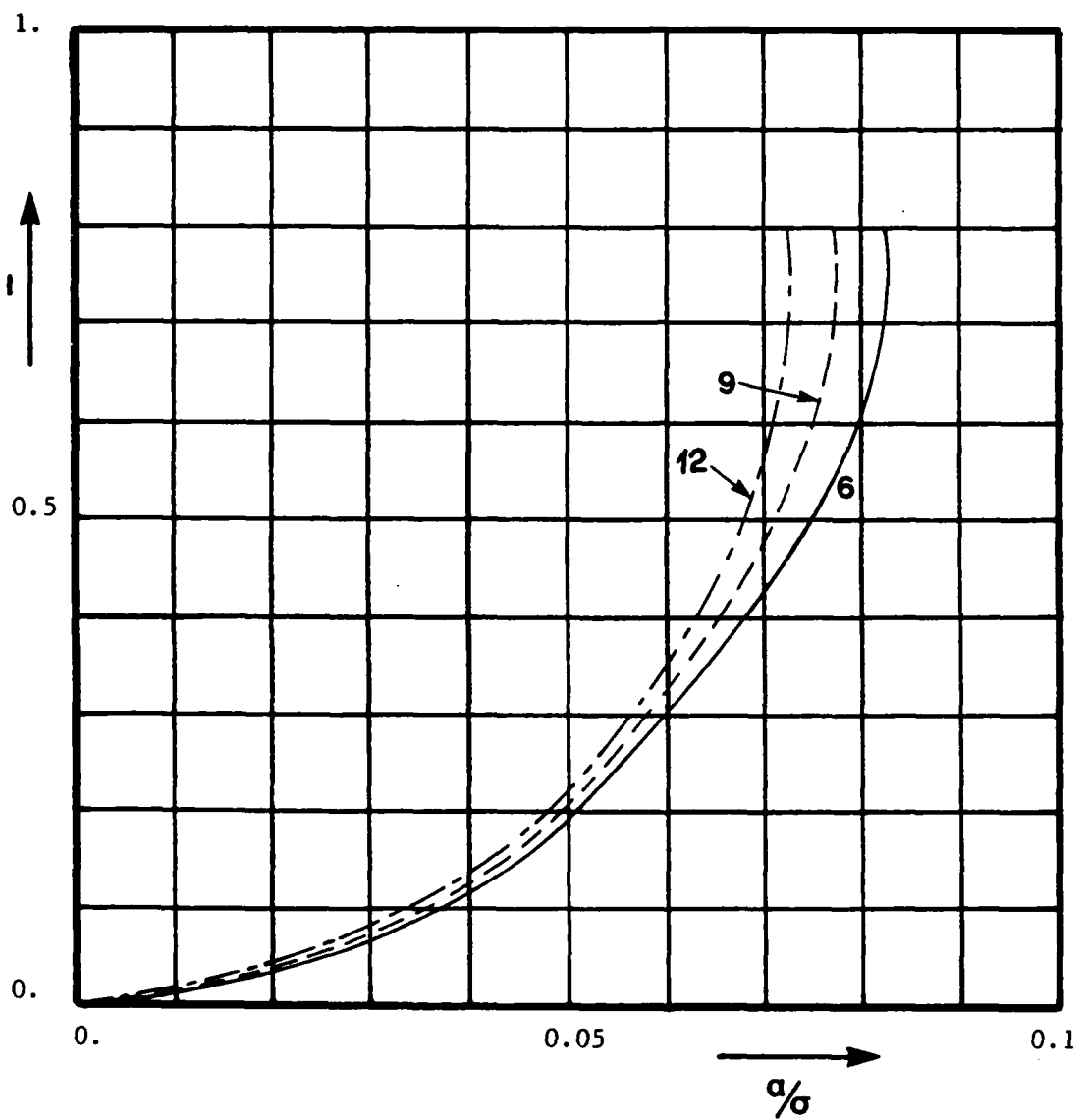


Figure D1. l vs. α/σ for NACA 16 series sections of 6%, 9%, and 12% thickness/chord ratios at $\alpha = 4^\circ$ using pure linear theory.

1.

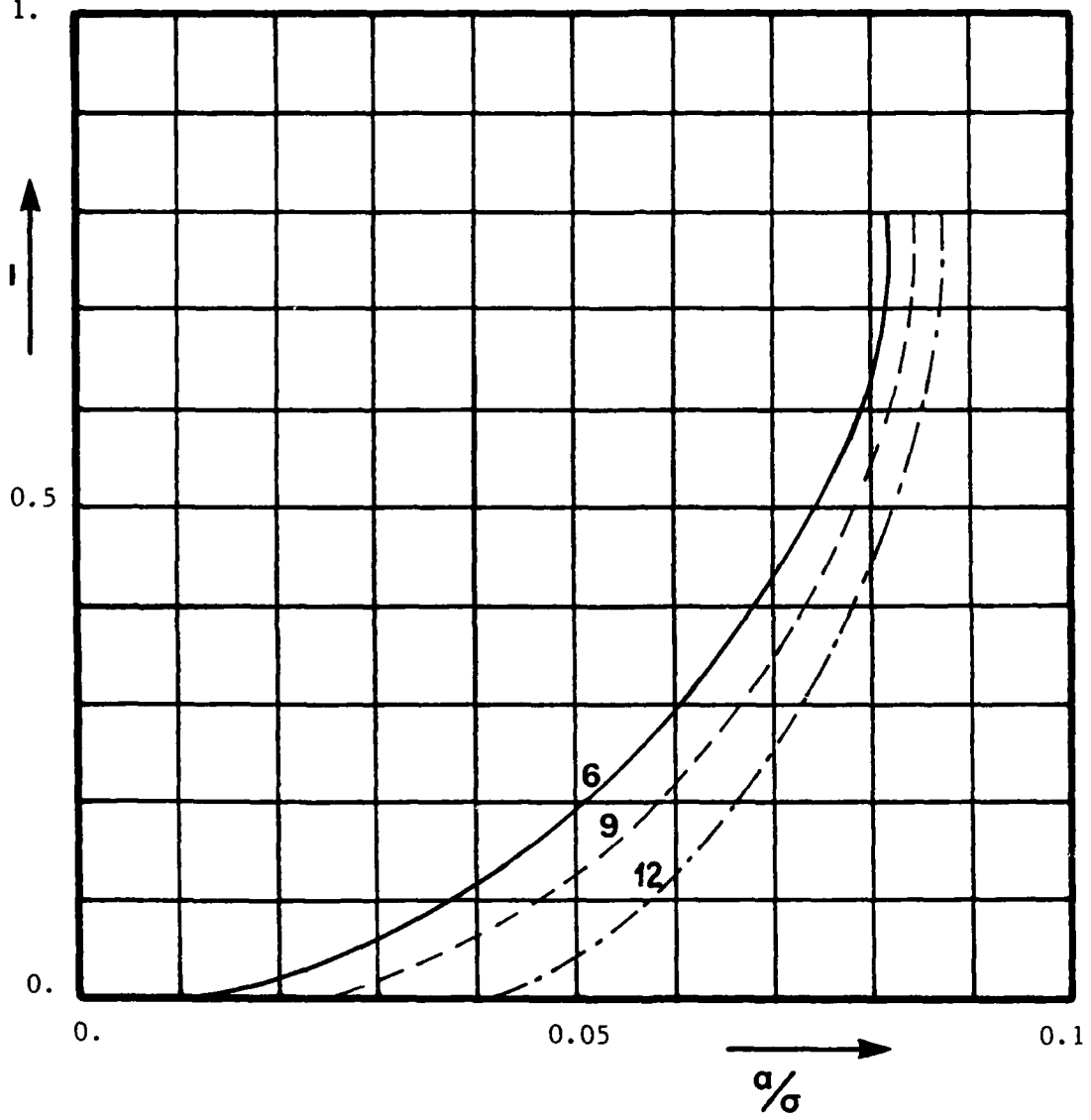


Figure D2. l vs. α/σ for NACA 16 series sections of 6%, 9%, and 12% thickness/chord ratios at $\alpha = 4^\circ$ using linear theory including leading edge corrections.

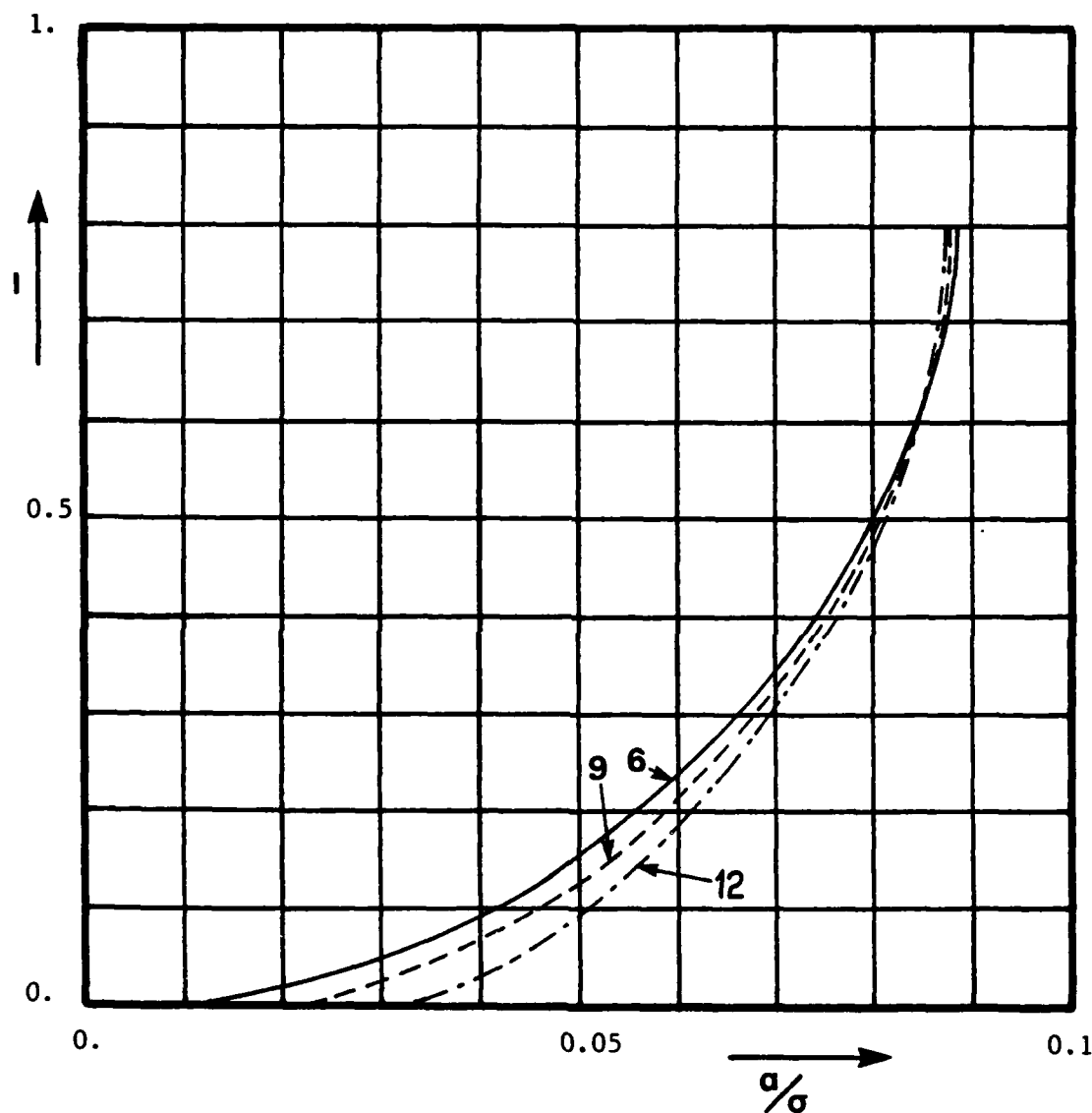


Figure D3. l vs. α/σ for NACA 16 series sections of 6%, 9%, and 12% thickness/chord ratios at $\alpha = 4^\circ$ using non-linear theory [38].

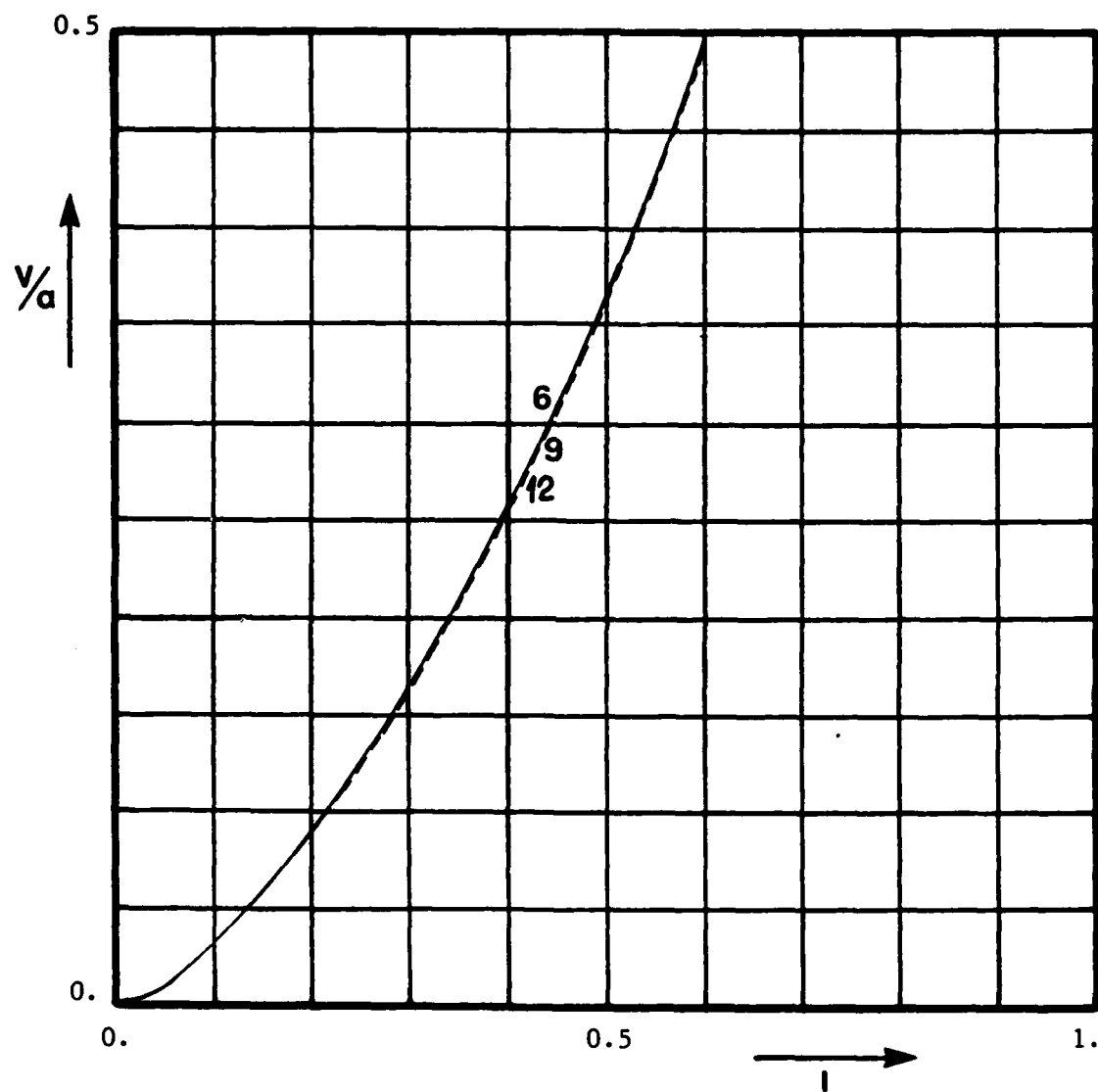


Figure D4. V/a vs. l for NACA 16 series sections of 6%, 9%, and 12% thickness/chord ratios at $\alpha = 4^\circ$ using pure linear theory.

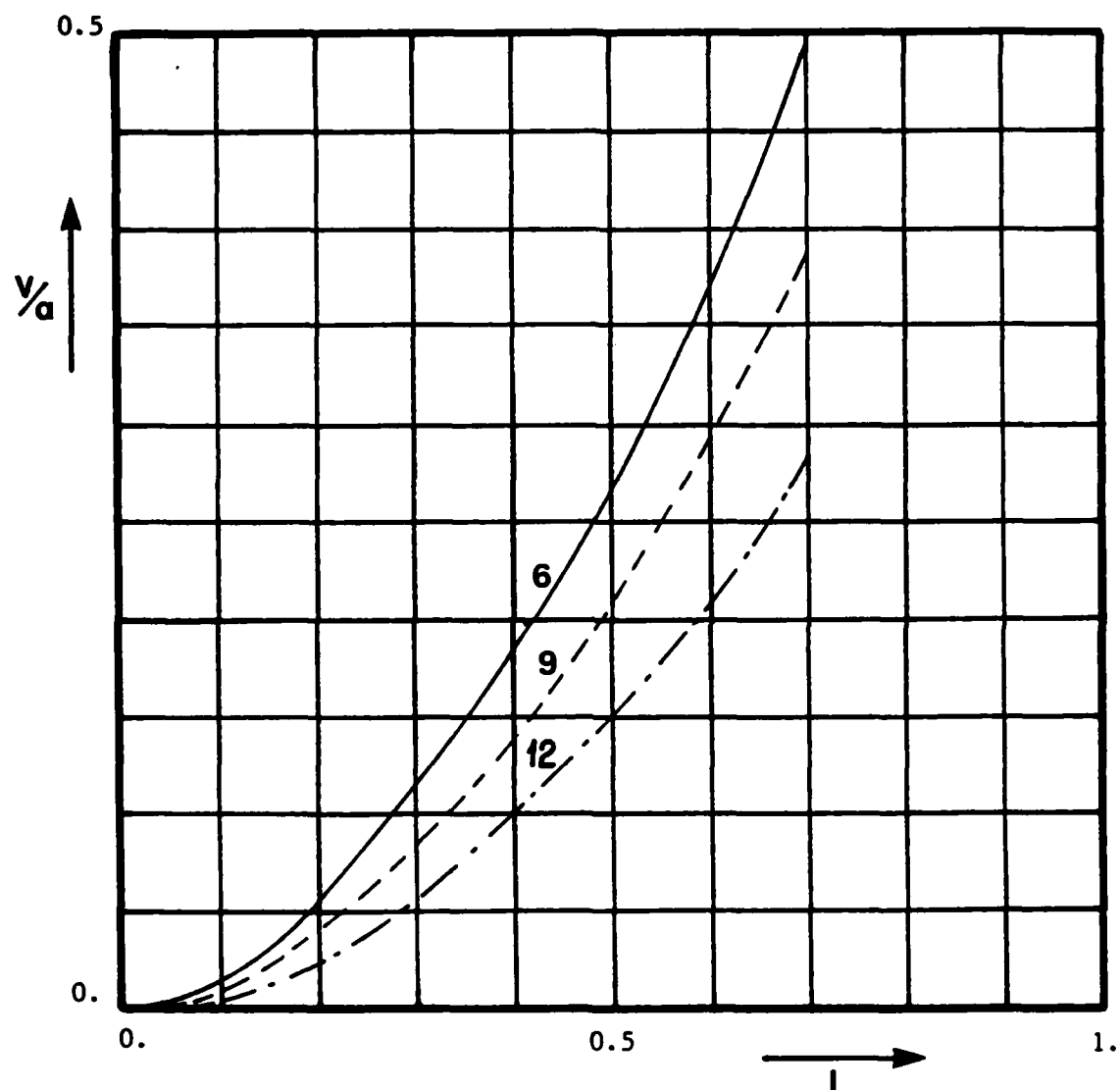


Figure D5. V/α vs. l for NACA 16 series sections of 6%, 9%, and 12% thickness/chord ratios at $\alpha = 4^\circ$ using linear theory including leading edge corrections.

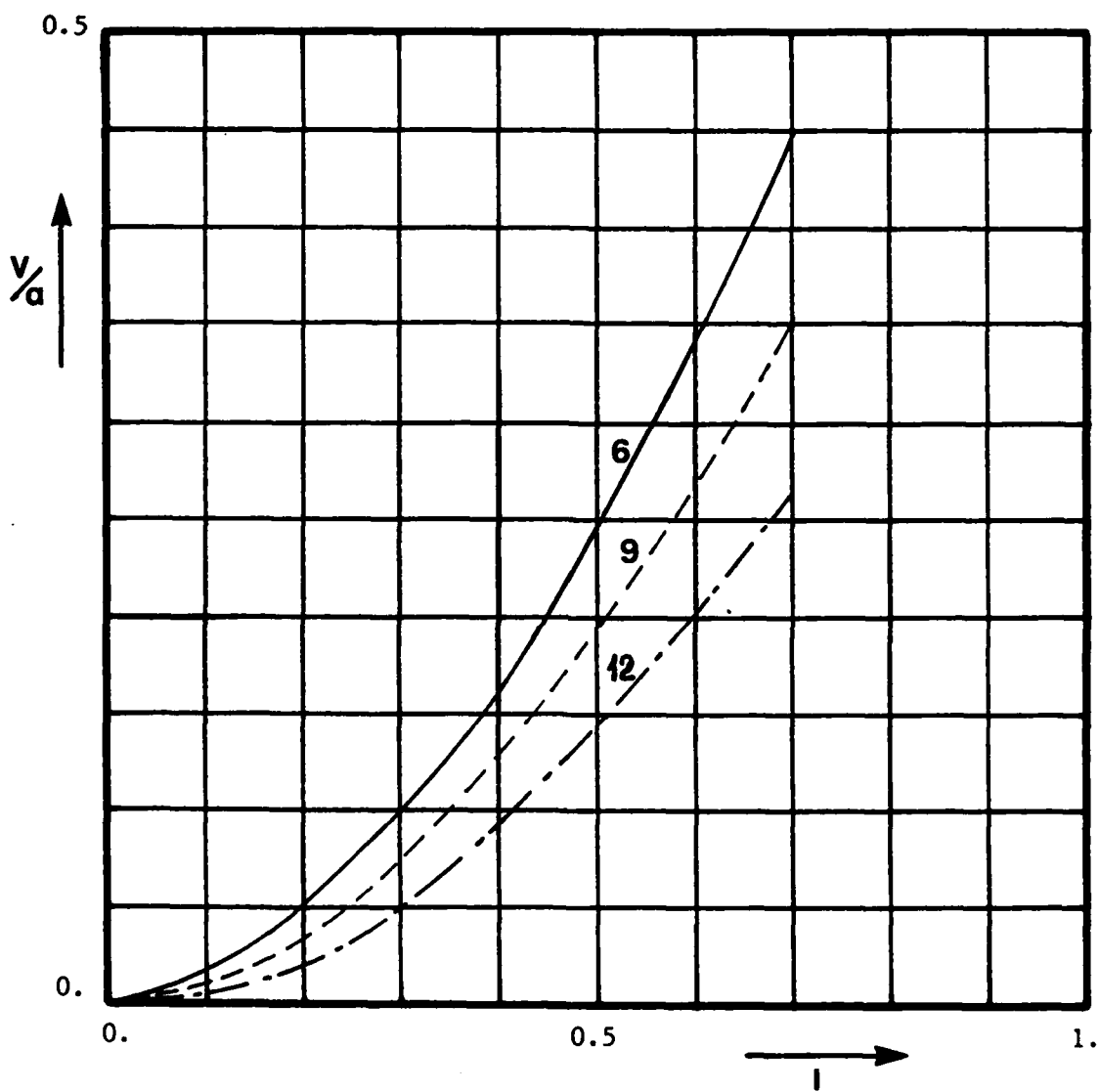


Figure D6. V/α vs. λ for NACA 16 series sections of 6%, 9%, and 12% thickness/chord ratios at $\alpha = 4^\circ$ using non-linear theory [38].

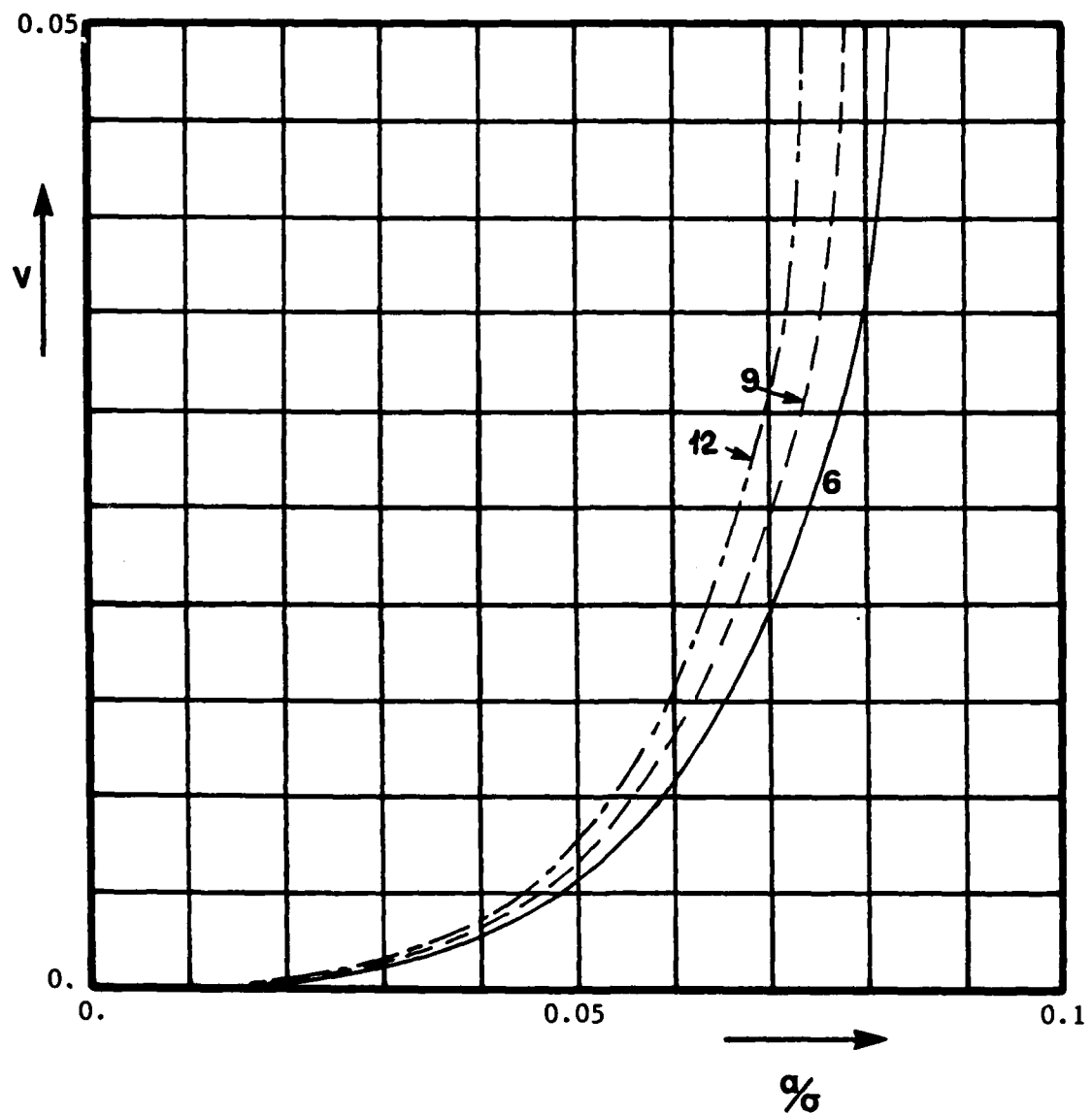


Figure D7. V vs. α/σ for NACA 16 series sections of 6%, 9%, and 12% thickness/chord ratios at $\alpha = 4^\circ$ using pure linear theory.

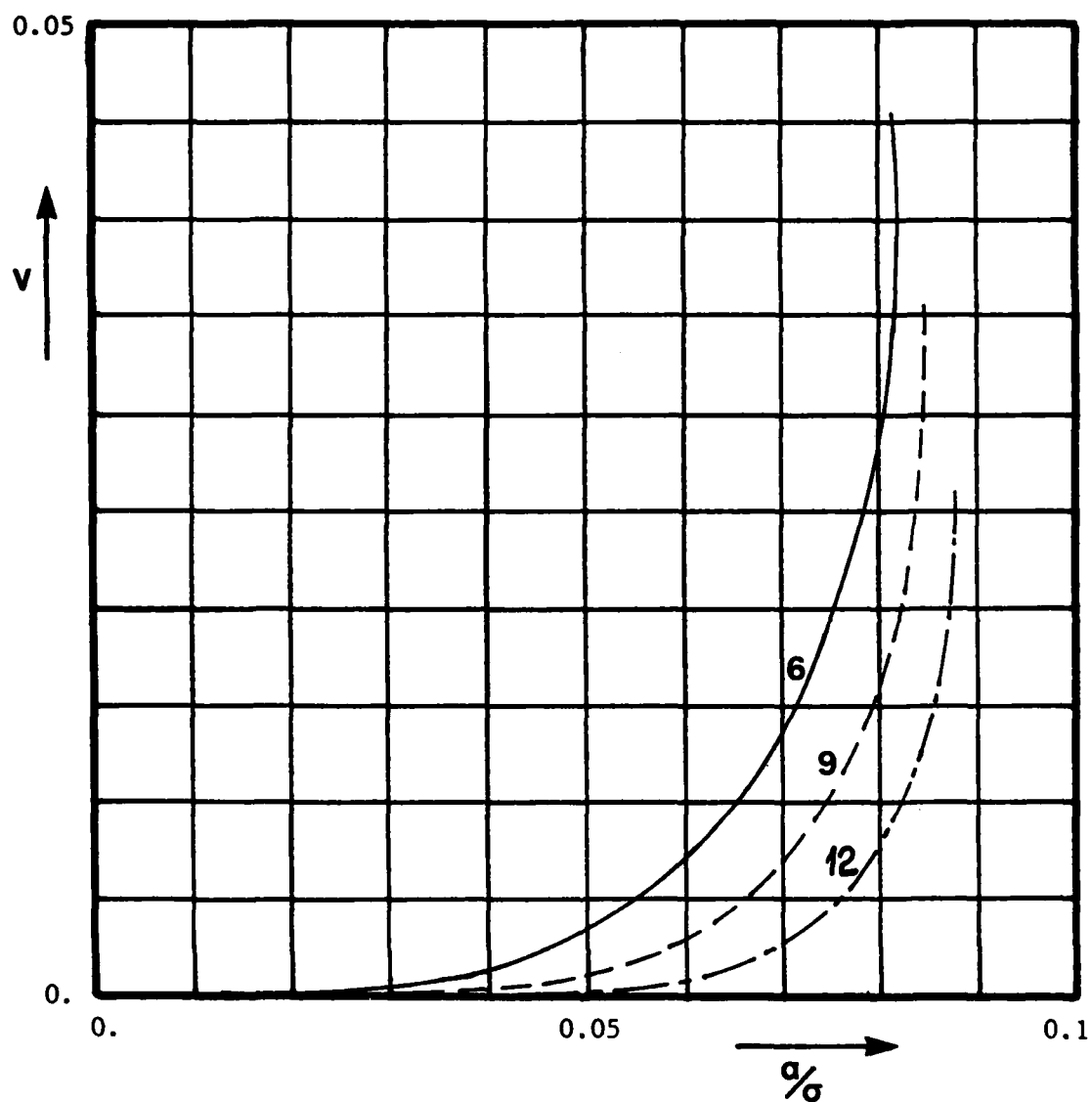


Figure D8. V vs. α/σ for NACA 16 series sections of 6%, 9%, and 12% thickness/chord ratios at $\alpha = 4^\circ$ using linear theory including leading edge corrections.

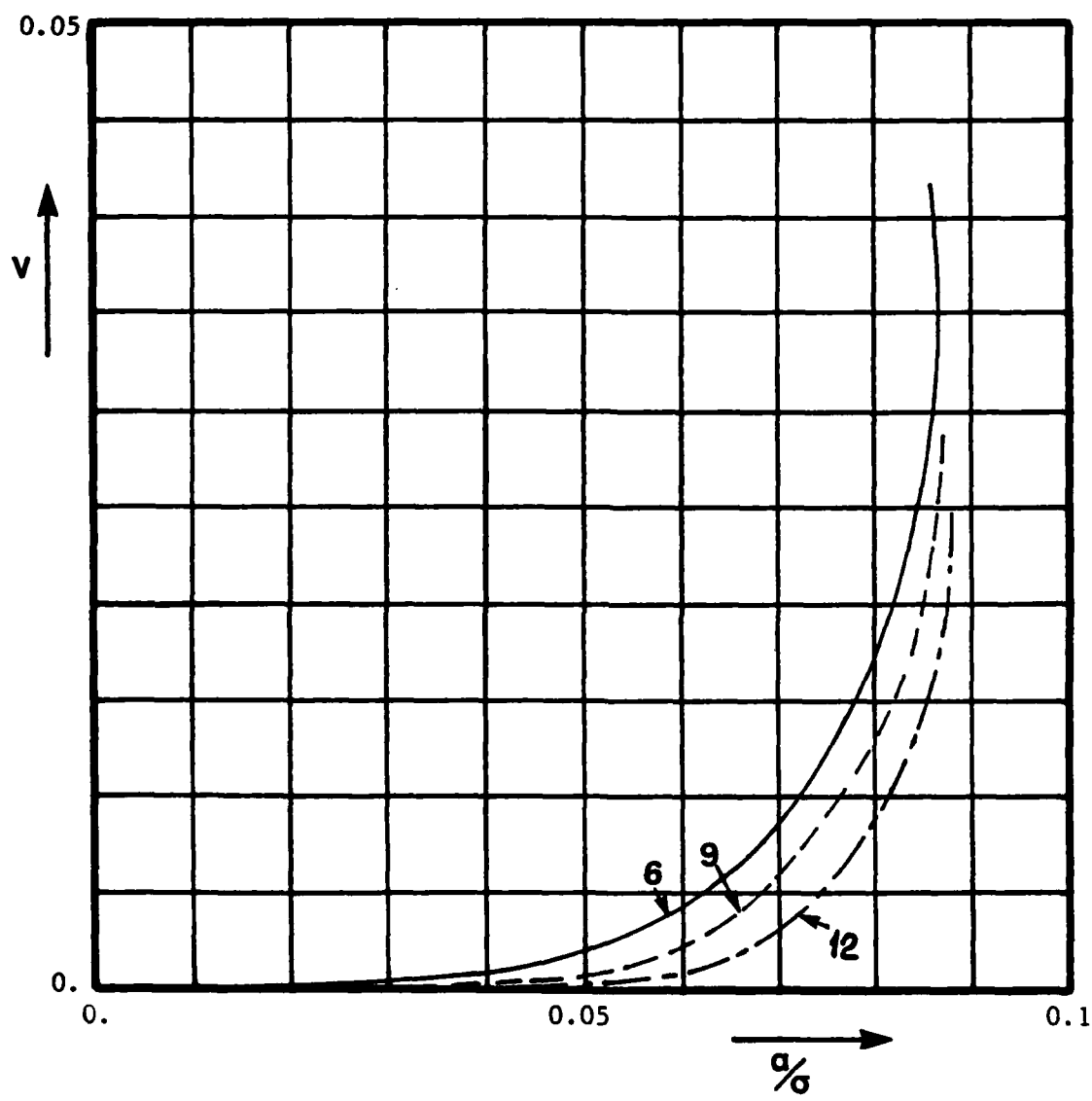


Figure D9. V vs. α/σ for NACA 16 series sections of 6%, 9% and 12% thickness/chord ratios at $\alpha = 4^\circ$ using non-linear theory [38].

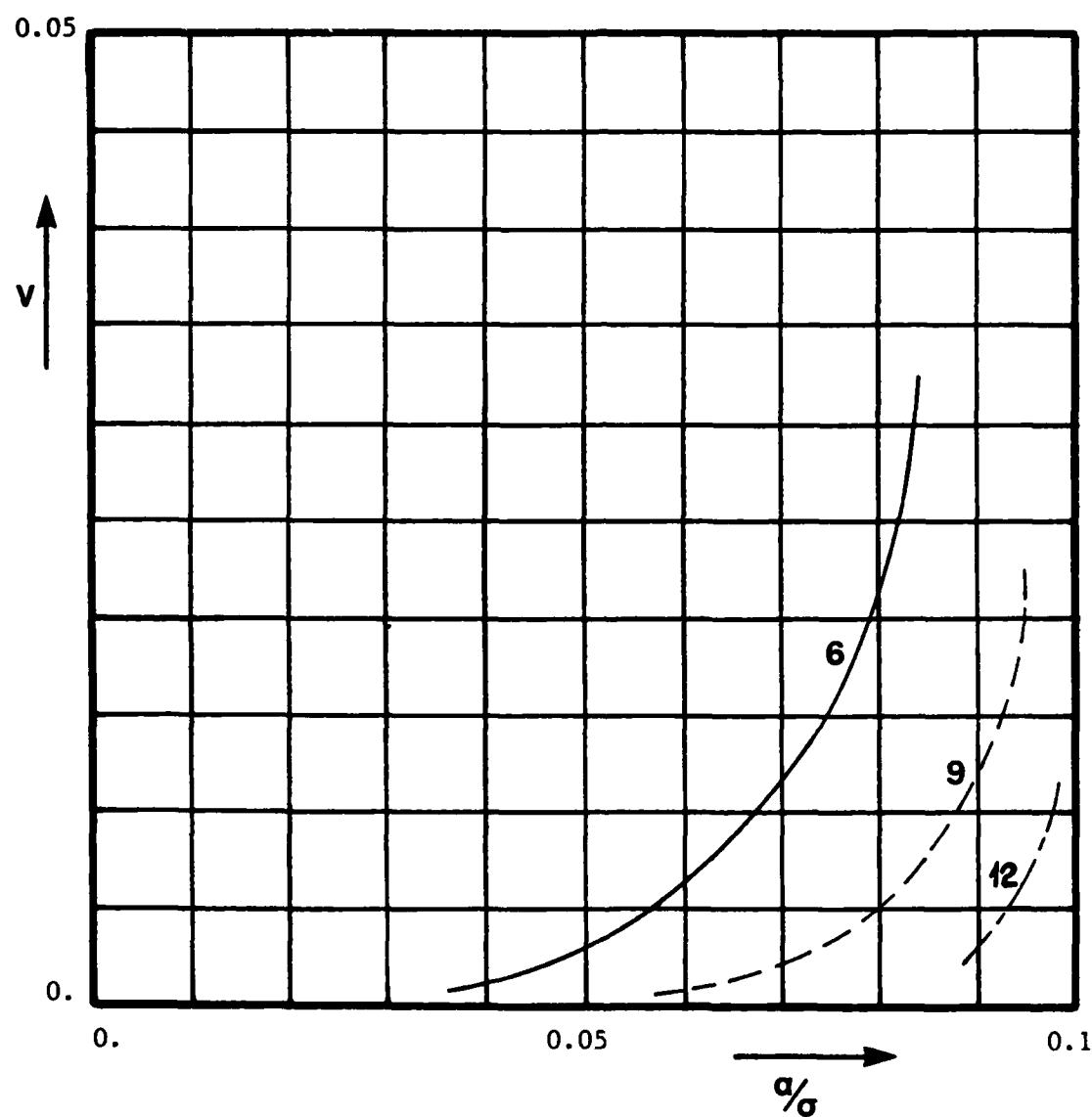


Figure D10. V vs. a/σ for NACA 16 series sections of 6%, 9%, and 12% thickness/chord ratios at $\alpha = 4^\circ$ using short cavity theory [36].

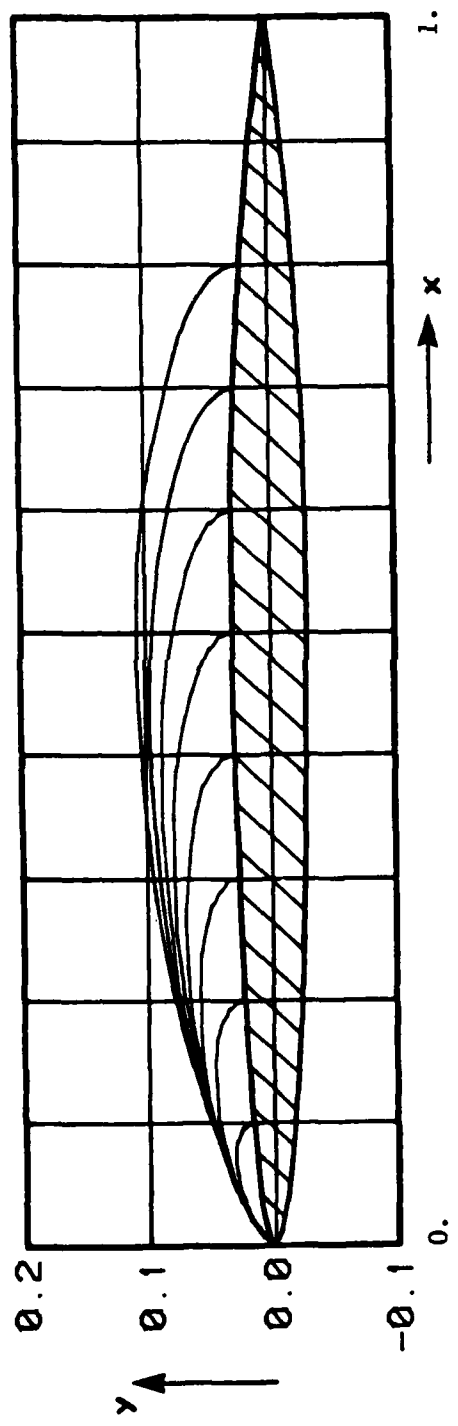


Figure D11. Cavity plots for NACA 16-006 thickness form at $\alpha = 4^\circ$ using linear theory including leading edge corrections.

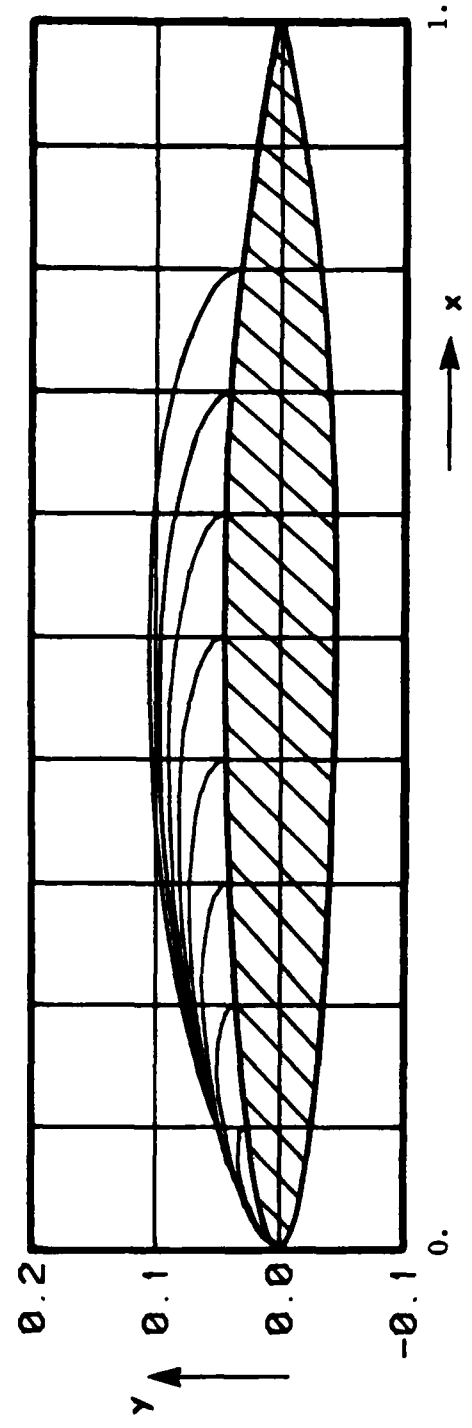


Figure D12. Cavity plots for NACA 16-009 thickness form at $\alpha = 4^\circ$ using linear theory
including leading edge corrections.

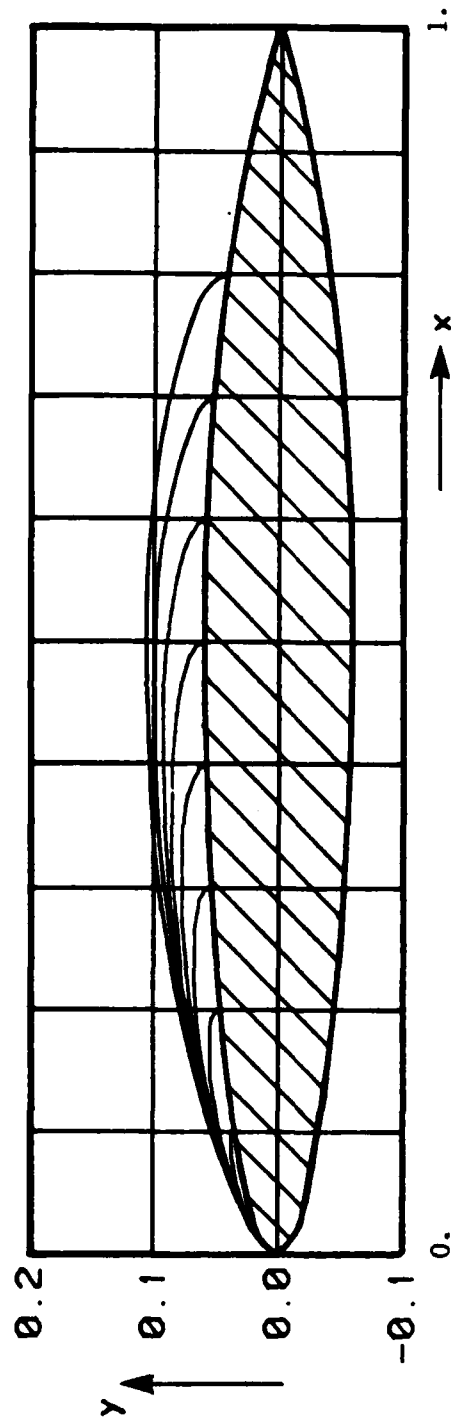


Figure D13. Cavity plots for NACA 16-012 thickness form at $\alpha = 4^\circ$ using linear theory including leading edge corrections.

END

FILMED

9-85

DTIC